Laser Refrigeration of Ytterbium-Doped Alkali-Rare-Earth-Fluoride Nanostructures and Applications for Radiation-Balanced Lasers

Xiaojing Xia

A dissertation
submitted in partial fulfillment of the
requirements for the degree of

Doctor of Philosophy

University of Washington

2021

Reading Committee:

Peter J. Pauzauskie, Chair

James J. De Yoreo

Arka Majumdar

Mohammad Malakooti

Program Authorized to Offer Degree:
Molecular Engineering

University of Washington

Abstract

Laser Refrigeration of Ytterbium-Doped Alkali-Rare-Earth-Fluoride Nanostructures and Applications for Radiation-Balanced Lasers

Xiaojing Xia

Chair of the Supervisory Committee:
Associate Professor Peter J. Pauzauskie
Department of Materials Science and Engineering

This work focuses on the development of new laser cooling materials and their applications for radiation-balanced lasers. The report begins with a brief introduction in Chapter 1 to the field of solid-state laser refrigeration, emphasizing the fundamental physical phenomena that have made solid-state laser-cooling possible. The concept of radiation balanced lasers and some attempts to realize radiation balanced lasing with different gain media structures are also introduced.

Chapter 2 introduces non-contact thermometries for micrometer and nanometer-scale materials, especially those frequently mentioned in this dissertation. Different temperature-dependent parameters are measured to interpret temperature, such as fluorescence, diffusion coefficient, Young's modulus, etc. The widely used Er^{3+} ratiometric thermometry is discussed in Chapter 3 in detail. A new green emission is introduced, which overlaps with the green luminescence typically used for intensity ratiometric thermometry. This emission is often neglected and is very sensitive to excitation power. Therefore, the wavelength intervals for intensity ratio measurement must be selected carefully to achieve accurate temperature readouts.

In Chapter 4, a group of new laser cooling materials, potassium lutetium fluorides,

are discussed. The rapid, low-cost hydrothermal synthesis of potassium lutetium fluoride materials was performed. Four crystalline phases were synthesized, namely trigonal $KLuF_4$, orthorhombic KLu_2F_7, cubic KLu_3F_{10}, and orthorhombic K_2LuF_5, with each phase exhibiting unique microcrystalline morphologies. Fluorescence spectra and emission lifetimes of the four crystalline phases were characterized based on the point-group symmetries of trivalent cations. Laser refrigeration was measured by observing both the optomechanical eigenfrequencies of microcrystals on cantilevers in vacuum and the Brownian dynamics of optically-trapped microcrystals in water. Among all four crystalline phases, the most significant laser cooling was observed for 10%Yb:$KLuF_4$ with cooling of 8.57 $\pm$ 2.07 K below room temperature. The end of this chapter presents some preliminary crystal growth results of potassium lutetium fluoride with different stoichiometries. The exact growth mechanism remains unclear for future exploration.

Chapter 5 discussed point defects in laser refrigeration materials and their impacts on cooling performance. After X-ray irradiation, point defects are formed in Yb:$YLiF_4$ (YLF) microcrystals. Two defects with different thermal stability are formed according to TL spectra. These defects are assigned to F-centers tentatively based on EPR spectra. The laser cooling performance of such Yb:YLF deteriorated a lot after irradiation. This is probably due to the increased non-radiative relaxation rate with the interaction of point defects and Yb^{3+}.

In Chapter 6, applications of laser cooling crystals to radiation-balanced lasers are discussed. Although the output power of commercial fiber lasers has been reported to exceed 500 kW, the heat generated within fiber gain-media has limited the generation of higher laser powers due to thermal lensing and melting of the gain-media at high temperatures. Radiation-balanced fiber lasers promise to mitigate detrimen-

tal thermal effects within fiber gain-media based on using upconverted, anti-Stokes photoluminescence to extract heat from the optical fiber's core. In this chapter, we experimentally demonstrate that Yb(III) ions within YLF microcrystals can cool the cladding of optical fibers. Based on this experiment, a design for radiation-balanced fiber-lasers using a composite fiber cladding material is presented that incorporates YLF nanocrystals as the active photonic heat engine. YLF crystals have the potential to form composite cladding materials to mitigate thermal gradients within the core and cladding based on anti-Stokes photoluminescence. With the development of new amorphous optical refrigeration glass materials, a new design of an all-glass multi-mode clad pumped fiber laser is proposed to provide more cooling power with clad pumping. Finally, analytical models of heat transfer within the fiber of both designs are presented where the light within the fiber core is responsible for the heating while the light in the cladding excites Yb(III) ions for anti-Stokes laser refrigeration.

TABLE OF CONTENTS

LIST OF FIGURES

GLOSSARY

CBM: cold Brownian motion

DI: deionized

EDS: energy-dispersive x-ray spectroscopy

EPR: electron paramagnetic resonance

KLF: potassium lutetium fluoride

CDSNR: cadmiun sulfide nanoribbon

FTIR: Fourier transform infrared

LIR: luminescence intensity ratio

NA: numerical aperture

NC: nanocrystal

NP: nanoparticle

NIR: near infrared

PL: photoluminescence

PLE: photoluminescence excitation

PSD: power spectral density

QPD: quadrant photodiode

SAED: select-area electron diffraction

SEM: scanning electron microscope

TL: thermoluminescence

XANES: X-ray absorption near edge structure

YLF: yttrium lithium fluoride

Some passages have been quoted verbatim from the following sources:

1. **X. Xia**, A. Pant, E. J. Davis, P. J. Pauzauskie, Design of a radiation-balanced fiber laser via optically active composite cladding materials. *J. Opt. Soc. Am. B* **36(12)**, 3307 (2019).

2. **X. Xia**, A. Pant, A. S. Ganas, F. Jelezko, P. J. Pauzauskie, Quantum point defects for solid-state laser refrigeration. *Adv. Mat.* **33 (23)**, 1905406 (2021).

3. **X. Xia**, A. Pant, X. Zhou, E. A. Dobretsova, A. B. Bard, M. B. Lim, J-Y D. Roh, D. R. Gamelin, P. J. Pauzauskie, Hydrothermal synthesis and solid-state laser refrigeration of potassium lutetium fluoride microcrystals. *Chem. Mat.* **33 (12)**, 4417-4424 (2021).

4. **X. Xia**, A. Volpi, J-Y D. Roh, C. Michael, D. R. Gamelin, M. P. Hehlen, p. J. Pauzauskie, The impact of $^2H_{9/2} \longrightarrow {}^4I_{13/2}$ emission from Er^{3+} ions on ratiometric optical temperature sensing with Yb^{3+}/Er^{3+} co-doped upconversion materials. *J. Lumin.* **236**, 118006 (2021).

ACKNOWLEDGMENTS

I want to thank my advisor, Professor Peter J. Pauzauskie, without whom I could never accomplish this work. His academic rigor, broad knowledge, passion for science, and patience have inspired me for the past five years. I appreciate Professor Emeritus E. James Davis for all of his guidance and feedback and the interesting science stories he shared with me.

I want to thank Dr. Xuezhe Zhou for the conception and initial development related to potassium lanthanide fluorides. I also thank him and Dr. Matt Lim, Dr. Matt Crane for training me during my first year in the Pauzauskie lab. Thanks to Dr. Anupum Pant, who always encouraged me and inspired me a lot when we worked on the MURI project. Thanks to Dr. Abbie Ganas, Dr. Elena Dobretsova, Alex Bard, Greg Felsted, Rachel Gariepy, and Chaman Gupta for all the things they taught me and supported me during hard times. I want to thank Diwash Dhakal, Dr. James Feathers, Dr. Donald Mannikko, and Dr. William Holden for helping with X-ray radiation experiments and EPR and thermoluminescence measurements.

I want to thank my family and friends. My deepest gratitude to my parents, Weiqin Li and Zhongnan Xia, who give me everything I need. Finally, I want to thank my husband, Weishi Yan. You are my North Star in this lonely world.

DEDICATION

To my dear family and friends, I love you all

Chapter 1
INTRODUCTION

1.1 Motivation

Solid-state laser refrigeration is based on a counter-intuitive process in which a solid material absorbs low-entropy photons produced by a laser and then emits new photons through spontaneous luminescence with the emitted photons having both a higher average energy and net entropy[1]. The laser refrigeration process is analogous to reversing the operational cycle of an optically-pumped laser, where the "quantum-defect" removes, rather than contributes heat to the gain medium.

One of the earliest papers reporting the concept of optical refrigeration based on anti-Stokes fluorescence was published in 1929 with a focus on a vapor of sodium atoms[2]. However, it was not until 1995 that the first experimental demonstration of solid-state laser cooling was reported[3]. In the last 25 years tremendous progress has been made in demonstrating the solid-state laser refrigeration of both amorphous[3, 4, 5] and crystalline materials[6, 7, 8, 9, 10, 11] under vacuum and atmospheric conditions. Solid-state laser cooling has also been demonstrated within aqueous media[12], enabling the first experimental demonstration of cold Brownian motion (CBM) since Einstein's seminal paper[13] on Brownian motion in 1905.

Unlike the Doppler cooling of metal atom vapors, solid-state laser refrigeration does not require high vacuum and low starting temperature conditions. In contrast with thermoelectric cooling, solid-state laser refrigeration is capable of cooling materials in the absence of electrical connections. Furthermore, it does not require moving parts or cryogenic fluids which eliminates detrimental mechanical vibrations or the risk

of mechanical failure. These unique attributes have enabled promising applications in the solid-state laser cooling of focal plane arrays for imaging or spectroscopy[14], for the development of radiation-balanced lasers[15] capable of operating at high continuous powers, controlling the temperature of frequency standards based on optical cavities[16], or modulating the temperature of individual molecules at physiological conditions[12, 17].

In our lab, instead of cooling bulk materials, we work on crystals in micro- or nano-scales. To achieve laser cooling of a single nanocrystal, there are several challenging difficulties that need to be solved: 1) Fabrication and characterization of high quality crystalline materials to achieve high quantum cooling efficiency and low background absorption; 2) Optimization of material's structure and dopant concentration; 3) Isolation of single nanocrystal from substrate to prevent heat generation and conduction; 4) High irradiance of excitation source to compensate the low absorption coefficient of Yb^{3+} ions in a nanocrystal; 5) Precise temperature control and measurement of single nanocrystals; 6) Simulation prediction of single nanocrystal under certain excitation source to help understand and improve laser cooling performance.

Overall, having the capability to solve each of the problems can help inform ongoing experiments not only in the laser cooling community, but also the materials science community, as well as creating new possibilities for many other future research directions and applications. In the meanwhile, we want to move forwards to realize radiation balanced micro-/nano-lasers with the cooling grade crystals we have. Radiation balanced lasers in other forms, such as fiber lasers, are also proposed.

1.2 Fundamentals of laser cooling

It is assumed normally that following optical excitation a luminescent material will emit photons with a lower energy (longer wavelength) relative to the energy of the

absorbed photons. This red-shifting of the emitted photon's energy is known as the Stokes shift and the conservation of energy requires heating of the optical material. In contrast to Stokes luminescence, if the emitted photons have a higher average energy relative to what was absorbed (anti-Stokes luminescence) then phonon energy can be removed from the crystal lattice. If the anti-Stokes luminescence has a near-unit quantum efficiency, then the overall removal of phonon energy from the material may result in laser cooling.[18]. This process results in internal cooling of the solid, known as solid-state laser cooling, or optical refrigeration.

When Pringshiem first proposed the optical refrigeration of vaporized sodium metal atoms in vacuum[2], there were concerns about the violation of the second law of the thermodynamics. In 1946, Landau helped address these concerns by quantifying the optical entropy of the system[19]. Lasers have low optical entropy due to their small divergence, narrow photon energy range, phase coherence, and well-defined polarization. Following optical excitation of the solid, the emission of spontaneous (anti-Stokes) luminescence has a higher net entropy when considering the wide divergence, broad photon energies, low phase coherence, and multiple polarization states of the emitted light. The need for optical radiation with low entropy is a major reason why solid-state laser cooling was not demonstrated before the advent of the laser.

However, several additional thermodynamic parameters are also important to realize the optical cooling of solid-state materials. In this section several fundamental physical requirements for the experimental demonstration of solid-state optical refrigeration are reviewed. In particular, the overall cooling process along with the three most important parameters describing it are described: 1) the cooling efficiency, 2) the absorption efficiency, and 3) the external quantum efficiency. These are discussed by introducing the simplified four-level energy model in Section 1.2.1. The material properties affecting these parameters are discussed in Section 1.2.2.

1.2.1 Cooling Parameters

Solid-state laser refrigeration can be described well by a four-level electronic system. Figure 1.1 depicts the anti-Stokes process for a two-manifold system introduced by Seletskiy *et al*[20, 21] consisting of a ground-state manifold and an excited-state manifold, both with two sub-states |0>, |1>, and |2>, |3>. Such sub-states can be considered as quasi-continuous vibrational broadening of the ground and excited states for semiconductor materials or discrete crystal field induced Stark levels for rare-earth (RE) ions. Although in more practical cases there are more than two sub states, such a model is enough to explain the cooling process. Excitation photons are chosen to have an energy ($h\nu$) that is resonant with a transition between the top of the ground-state manifold to the bottom of the excited-state manifold. This optical excitation breaks the thermal equilibrium of the relative populations between the two manifolds. The ground and excited atoms must reach quasi-equilibrium by absorbing phonons from the lattice with the rates w_g and w_u. Afterwards, spontaneous emission of a photon higher in energy than the absorbed photon, $h\nu_f$, releases the energy into free space. It is assumed that interactions between electrons and phonons within each manifold, also known as "thermalization", are far faster ($\sim$ps) than the spontaneous emission rate ($\sim$ms), which is valid for a broad range of materials and temperatures. This electron-phonon interaction helps maintain the quasi-equilibrium of the Boltzmann distribution among each manifold. This will be discussed in more details with materials properties in Section 1.2.2. For now, a simplified four-level model is utilized to discuss the fundamentals of laser cooling processes in this section.

Cooling Efficiency

The thermodynamic cooling efficiency η_c of the cooling cycle is expressed as

$$\eta_c = \frac{h\nu_f - h\nu}{h\nu} = \frac{\lambda}{\lambda_f} - 1, \tag{1.1}$$

where $h\nu$ is the pump photon energy, $h\nu_f$ is the mean fluorescence energy, $\lambda = c/\nu$ is the pump wavelength, and $\lambda_f = c/\nu_f$ is the mean fluorescence wavelength.

Additional considerations must be made to calculate the thermodynamic efficiency for non-ideal systems, such as the probability that a pump photon can be absorbed, the probability that an absorbed photon is converted to a fluorescence photon, and the probability a spontaneously emitted photon escapes the system. Non-ideal systems require the introduction of the other two parameters, absorption efficiency and external quantum efficiency discussed in Section 1.2.1 and Section 1.2.1 respectively[22, 20]. Following these considerations, the overall cooling efficiency can be rewritten as

$$\eta_c(\nu, T) = \eta_{ext}\eta_{abs}\frac{\lambda}{\lambda_f} - 1. \tag{1.2}$$

This describes the cooling efficiency by which an excited ion decays to its ground state with the fluorescence photon escaping to free space. The cooling efficiency must be positive to realize net cooling, which means high external quantum efficiency (η_{ext}), high absorption efficiency (η_{abs}), and a large anti-Stokes shift ($h\nu_f - h\nu$) are required.

Absorption Efficiency

The absorption efficiency η_{abs} describes the probability of a pump photon being absorbed by the cooling ions rather than an impurity, which is a function of temperature

and wavelength defined by

$$\eta_{abs} = \frac{\alpha_r(\lambda, T)}{\alpha_r(\lambda, T) + \alpha_b}, \tag{1.3}$$

where $\alpha_r(\lambda, T)$ is the temperature and wavelength-dependent resonant absorption coefficient of the cooling ion. The term α_b represents background absorption, which is assumed to be independent of temperature and wavelength[23]. However, a recent study shows the background absorption could be temperature dependent[24, 25].

It is clear from the Eq. 1.3 that a high value of resonant absorption (α_r) and low detrimental background absorption (α_b) would maximize the absorption efficiency (η_{abs}), which would enhance the cooling efficiency. The detrimental absorption could be minimized by improving the material's purity while it's more complicated to optimize the resonant absorption. Considering the saturation of absorption, the resonant absorption coefficient gets reduced if one tries to increase thermodynamic cooling efficiency by increasing the Stokes shift[26]. The choice of the optimum pump wavelength should have a moderate resonant absorption and Stokes shift to maximize the cooling efficiency. The pump wavelength with the highest cooling efficiency can be predicted with temperature-dependent absorption and emission data.

External Quantum Efficiency

The external quantum efficiency (η_{ext}) is a measure of the fraction of excited ions that transfer heat out of the material through anti-Stokes luminescence, and is given by

$$\eta_{ext} = \frac{\eta_e W_r}{\eta_e W_r + W_{nr}}, \tag{1.4}$$

where η_e is the luminescence extraction efficiency which denotes the fraction of the emitted photons that are able to escape from the material. W_r and W_{nr} are radiative and nonradiative decay rates, respectively. The ratio $W_r/(W_r+W_{nr})$ quantifies the

probability of an excitation producing fluorescence and the η_e quantifies the probability that a spontaneously emitted photon exits the system.

The cooling requirement ($\eta_c > 0$) necessitates that the $\eta_{ext}\eta_{abs}$ product in Eq.(1.2) is as close as possible to unity, which means the vast majority of optical excitations should decay radiatively, and a minimum amount of parasitic heating due to unwanted background absorption from impurities should occur.

It is known that rare-earth ions doped into low-phonon energy glasses and crystal hosts (e.g. fluorides) are typically associated with high external quantum efficiency ($\eta_{ext} > 99\%$) for their electronic excited states[27, 28]. As such, the corresponding RE ions are excellent candidates for solid-state laser cooling within these host materials.

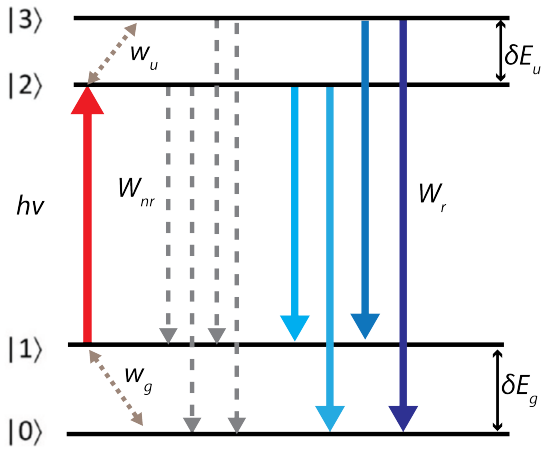

Figure 1.1: The simplified four-level model for optical refrigeration consisting of two pairs of closely spaced levels: |0> and |1> in the ground state and |2> and |3> in the excited-state manifolds. Reproduced with permission[20] ©2019 Wiley.

1.2.2 Material Properties Affecting Cooling Parameters

The three most important parameters describing the cooling process are addressed above in Section 1.2.1. In this section various material properties related to these

cooling parameters are discussed in more detail. Understanding the relationships between these material properties and the cooling parameters is helpful for developing new laser cooling materials.

As shown in Figure 1.1, this model involves a two-level ground state having a separation of δE_g, which represents the width of the ground-state manifold. Similarly, a two-level excited state with an energy splitting of δE_u is involved. Upon electronic excitation from |1> to |2> induced by the laser pump ($h\nu = E_2 - E_1$), the electronphonon interaction helps establish the Boltzmann quasi-equilibrium within each two-level manifold with relatively fast rates given by w_g and w_u. The excitation then decays to the ground state by radiative and nonradiative relaxations with the corresponding rates W_r and W_{nr}. The number density of populations in state |0>, |1>, |2>, and |3> are denoted as N_0, N_1, N_2, and N_3. The total ion density is $N_t = N_0 + N_1 + N_2 + N_3$. A set of rate equations have been constructed and the corresponding cooling parameters have been extensively discussed in previous reviews[20, 21]. From these equations, important parameters discussed in the following section can be derived.

Absorption Efficiency vs. Ground State Splitting

The resonant absorption coefficient in Eq. 1.3 can be expressed as[21]

$$\alpha_r = \sigma_{12} N_t \frac{e^{-\delta E_g / k_B T}}{1 + e^{-\delta E_g / k_B T}} \tag{1.5}$$

where σ_{12} is the absorption cross section associated with |1> to |2> transition and k_B is the Boltzmann constant. This reveals the diminishing pump absorption due to thermal depletion of the top ground state at low temperatures. When the temperature is low, the lattice phonon energy $k_B T < \delta E_g$ is insufficient to overcome the energy gap between |1> and |2> and further cooling cannot happen. This implies that lower

temperatures could be achieved with a narrower ground-state manifold because the electrons still can "thermalize" at low temperature. In general, the ground state is narrower in crystalline materials than in glasses. Also, crystalline materials with smaller crystal-field splitting of the ground-state manifold are preferred.

Quantum Efficiency vs. Lattice Phonon Energy

According to Eq. (1.4) the quantum efficiency is dependent on both the radiative and nonradiative relaxation rates. The radiative rate of RE-doped materials can be calculated using Judd-Ofelt theory while the multiphonon nonradiative relaxation rate, W_{nr}, follows the energy gap law[29]

$$W_{nr} = \beta e^{-\alpha m}, \tag{1.6}$$

in which β and α are characteristic constants for host materials and m is the number of phonons involved in the process. This equation reveals the criteria for both dopants and host materials: (i) large energy gap between the excited and ground states of $4f$ manifolds for dopants and (ii) low phonon energy of host materials. The energy gap between excited and ground states should be high so that more phonons are involved in the nonradiative process. The most successful materials for laser cooling have been either low phonon-energy fluoride glasses or crystals, typically with phonon energies below 500 cm^{-1}.

Besides the splitting of the ground-state manifold and phonon energy, defects like transition metals and other RE impurities could increase the nonradiative relaxation rate via energy transfer. .

Mean Fluorescence Energy vs. Electron - Phonon Interaction Rate

The mean fluorescence energy of the four-level system is given by[21]

$$h\nu_f = h\nu + \frac{\delta E_g}{2} + \frac{\delta E_u}{1 + (1 + R/w_u)e^{\delta E_u / k_B T}} \tag{1.7}$$

where R is the sum of the radiative and nonradiative relaxation rates ($R = W_r + W_{nr}$). This equation conveys that the mean fluorescence is red-shifted as temperature decreases which lowers the cooling efficiency. Such shift is enhanced when the electron-phonon interaction rate w_u is small compared to the total relaxation rate R that the excitation relaxes to the ground state before thermalization happens. Without thermalization, the excitation cannot absorb lattice energy from the host and thus no cooling takes place in a single cooling cycle.

As the temperature is lowered, both the red-shift of the mean fluorescence wavelength along with the decrease of resonant absorption contribute to reduce the overall cooling efficiency. At a certain temperature the cooling stops, i.e. $\eta_c \to 0$. This minimum achievable temperature (MAT) can be lowered by reducing the background absorption (higher material purity), increasing the quantum efficiency, enhancing the resonant absorption coefficient, and also selecting materials with a narrow ground-state manifold.

1.3 Fundamentals of radiation balanced lasers

The power scaling of high energy lasers has been limited due to the heat generation in the gain media, which cause a number of detrimental problems such as thermal lensing, mode instability, materials thermal degradation, etc. It has been proposed that solid-state lasers could be constructed in which the cooling of anti-Stokes fluorescence would offset heat generated by stimulated emission[30]. This mode of laser

operation is referred to as radiation balanced lasing. Unlike conventional exothermic laser systems, Radiation balanced lasers exhibit little or no internal heat generation. In principle, this technique would allow radiation balanced lasers to be scaled up to much higher average powers than conventional solid-state laser systems.

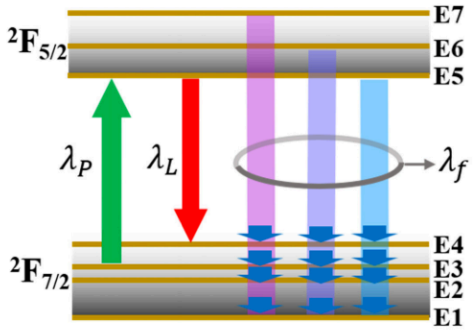

Figure 1.2: Energy diagram of Yb:YAG. λ_f, λ_p, and λ_l represent the mean fluorescence wavelength the wavelength of pump and laser photon, respectively. Reprinted from Ref [31]. Copyright ©2021 Optica Publishing Group.

As an example, a diagram of the radiation balanced lasing process is depicted in Figure 1.2 for the $4f$ transitions of Yb^{3+} ions in the YAG solid host, which is considered the workhorse of high-power solid-state lasers. By selecting the pump wavelength λ_p longer than the mean fluorescence wavelength λ_f, but shorter than the laser wavelength λ_l, the heat generated during the laser process can be balanced by the anti-Stokes fluorescence cooling process.

The radiation balanced lasers concept was first demonstrated experimentally in high quality Yb:YAG rods where powers exceeding 500 W by minimizing the heat load were reported under RBL condition[32]. A Yb:KGW based disk laser with reduced heating in quasi-CW operation was also reported. In 2019, the first radiation-balanced disk laser in an intracavity-pumped Yb:YAG crystal was demonstrated in kilowatt

power regimes[31]. Drastic improvement in thermal management has been achieved leading to high-power (multi-kilowatt) continuous wave (CW) operation by increasing the surface-to-volume ratio of the gain medium as in fiber lasers. Laser cooling has been observed in Yb:ZBLAN optical fibers[33], suggesting it is a viable laser cooling medium for radiation balanced lasers. Recently, net cooling has been realized in high-purity Yb-doped silica glass fibers[34, 35]. Although radiation balanced lasing has not been observed in optical fibers yet, there are some theoretical analyses and simulations towards radiation balanced fiber lasers[36, 37].

Chapter 2

THERMOMETRIES

Making direct temperature measurements of nanoscale materials is challenging due to the lack of small thermocouples. Direct physical contact with thermocouples can also conduct heat, limiting the accuracy of temperatures. Non-contact thermometry techniques based on spectroscopic and spin readout methods offer a great advantage over others because they prevent the possibility of a conductive heat flux being attached to the material physically. A variety of non-contact techniques may be used to measure the temperature of nanoscale materials. The thermometries I used and the challenges associated with them have been discussed in the following sections.

2.1 Yb^{3+} emission analysis

Yb^{3+} is a common dopant for laser refrigeration materials. Yb^{3+} emission analysis can be used to measure the internal temperature of the Yb doped crystal. This becomes a reliable complementary thermometry technique to verify the results from other methods.

2.1.1 Yb^{3+} Ratiometric Emission Analysis

The emission spectrum from Yb^{3+} ions excited using a NIR laser consist of a bright Stokes and anti-Stokes emission in the region of 900 to 1100 nm. Depending on the excitation wavelength, a shortpass / longpass filter can be applied to filter the laser line and analyze the Yb^{3+} emission. As illustrated in Figure 1.2 and FIgure 2.1a, the excited state and ground state split to 3 and 4 Stark levels, respectively. When the

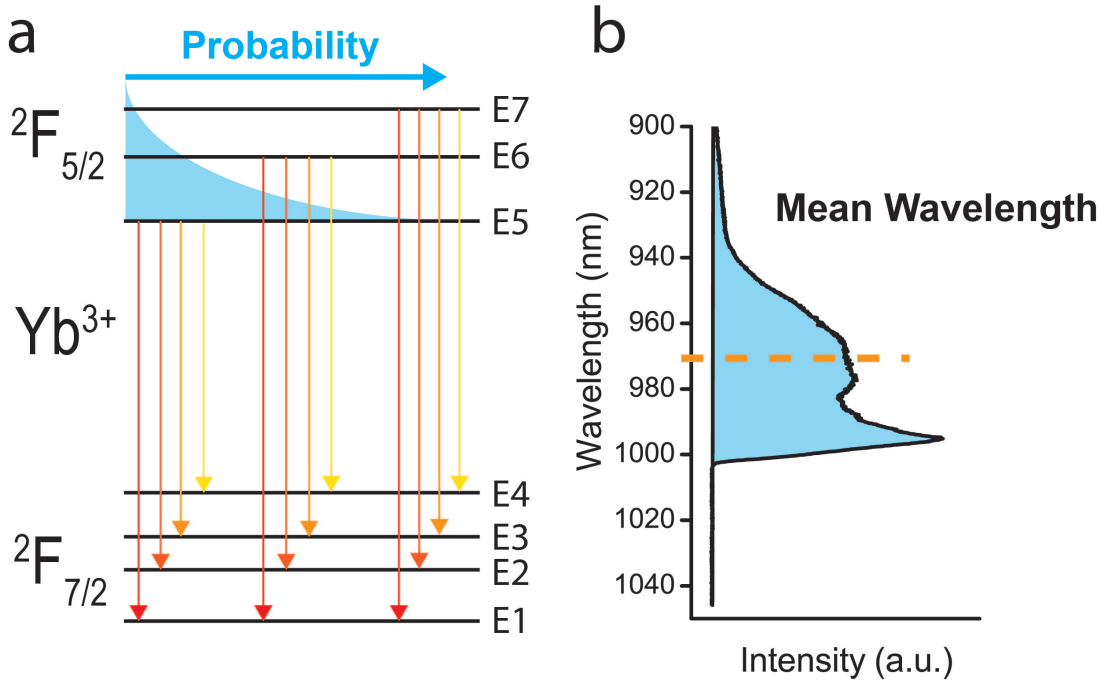

Figure 2.1: (a) The energy-level scheme of Yb^{3+} and (b) the emission spectra of Yb^{3+} $^2F_{5/2}$ $^2F_{7/2}$ transition upon excitation. A 1000 nm shortpass filter is applied.

ion is in a $LiYF_4$ host lattice, the emission spectrum has distinct peaks representing the $E_6 \rightarrow E_1$ (960 nm) and $E_5 \rightarrow E_3$ (993 nm). The areas under the peaks are represented as I_1 and I_2, respectively. The temperature of the Yb:$LiYF_4$ crystal can be determined using a ratiometric analysis of the fluorescence spectra. The intensity ratio of I_1 and I_2 bands is temperature dependent based on a Boltzmann distribution:

$$\frac{I_1}{I_2} \propto \exp\left(\frac{-(E_6 - E_5)}{k_B T}\right).[38,\ 39] \tag{2.1}$$

Lower ratio values correspond to lower temperatures. By evaluating the ratio of areas under the peaks I_1 and I_2 corresponding to the dominant E_6 and E_5 transitions, and using the above equation, the temperature can be interpreted.

This method is more reliable for small-sized microcrystals (<100 μm) as larger crystals are more susceptible to reabsorption effects. Due to reabsorption, the emitted light is absorbed better near the 960 nm wavelength, which may also contribute to the decrease in the ratio of I_1/I_2 and appear like cooling.

2.1.2 Mean wavelength analysis

In ratiometric emission analysis, at least two well-defined peaks without much overlap with the rest emission peaks are required to obtain the ratio. $E_6 \rightarrow E_1$ (960 nm) and $E_5 \rightarrow E_3$ (993 nm) emission are used for YLF. For other host materials without two distinct peaks, such as $NaYF_4$(Figure 2.1b), ratiometric analysis is not appropriate, and mean wavelength analysis should be used.

The mean wavelength of the spectrum is obtained by calculating the “spectral centroid" :

$$\lambda_f = \frac{\sum \lambda_i I(\lambda_i)}{\sum I(\lambda_i)} \tag{2.2}$$

where the summation represents the sum over all emission wavelength, $I(\lambda_i)$ is the

intensity, and λ_i is the wavelength at the i^{th} pixel. The mean wavelength analysis relies on the same Boltzmann distribution of excited and ground state as ratiometric emission analysis. However, the entire spectral window is integrated and no distinct peaks are required. Figure 2.1b shows the emission spectrum of Yb:$NaYF_4$ and the calculated mean wavelength. As the temperature of Yb:$NaYF_4$ grains increases, the mean wavelength blueshifts due to the changing excited-state Boltzmann distribution populations distribution, which redistributes intensities across the various peaks of the spectrum. Changes in the mean wavelength are directly correlated to a change in the crystal temperature.

2.1.3 Differential luminescence thermometry (DLT)

DLT is a variant of ratiometric analysis or mean wavelength analysis depending on whether two emission bands or the entire Yb emission are used. A differential luminescence spectrum is obtained Upon subtracting the normalized spectrum with a reference temperature spectrum. DLT can be applied to any material system that exhibits a temperature-dependent change in its luminescence spectrum. Therefore, DLT is a versatile technique for the measurement of temperature, which is widely used within the laser refrigeration community.

Two-band DLT is another variant of essentially the same technique, which analyzes the spectral distribution from Yb^{3+} emission by isolating two bands from the spectrum using interference filters. The signal is obtained by dividing the difference between two bands by their sum. More recently, a 7 mK temperature resolution was obtained for RE-doped materials.[40].

2.2 Er^{3+} emission analysis

The Er^{3+}, Yb^{3+} codoped nanocrystals can upconvert NIR light (920-1030 nm) to green and red light with two photon process via energy transfer from excited Yb^{3+} ions to fluorescent Er^{3+} ions.[41] The strong emission from a single nanocrystals can be seen with unaided eyes. Similar to Yb^{3+} emission, the Er^{3+} emission can be utilized for temperature measurement as well. The emission band shape, peak position or lifetime have been found that can be affected by temperature significantly.[42, 43]

The green emission from $^2H_{11/2}$ and $^4S_{3/2}$ excited states relates to two different emission bands of 515 nm-535 nm and 535 nm-570 nm. The intensity of the emission bands may be used to infer temperature changes through ratiometric thermometry by analysis of Boltzmann thermal populations,[43, 44] which is given by the equation:

$$\frac{I_2}{I_1} \propto exp(\frac{-(E_2 - E_1)}{k_b T}) \tag{2.3}$$

I_1 and I_2 are the integrated emission bands which relate to the transition between energy states E_2 and E_1 from the ground state. The temperature change of nanocrystals can lead to a thermalized Boltzmann distribution between the E_2 ($^2H_{11/2}$) and E_1 ($^4S_{3/2}$) manifolds of Er^{3+} and an intense green upconversion emission.

However, the green emission is not solely temperature-dependent. Factors such as laser power can also change the band shape and the intensity ratio. The power dependence of green emission and guides to perform accurate temperature analysis with Er^{3+} are discussed in Chapter 3

2.3 Cold Brownian motion analysis

The dynamics of a particle in liquid can be analyzed to extract the local temperature and viscosity. Usually, a particle is trapped in the laser tweezers, and the forwarded-

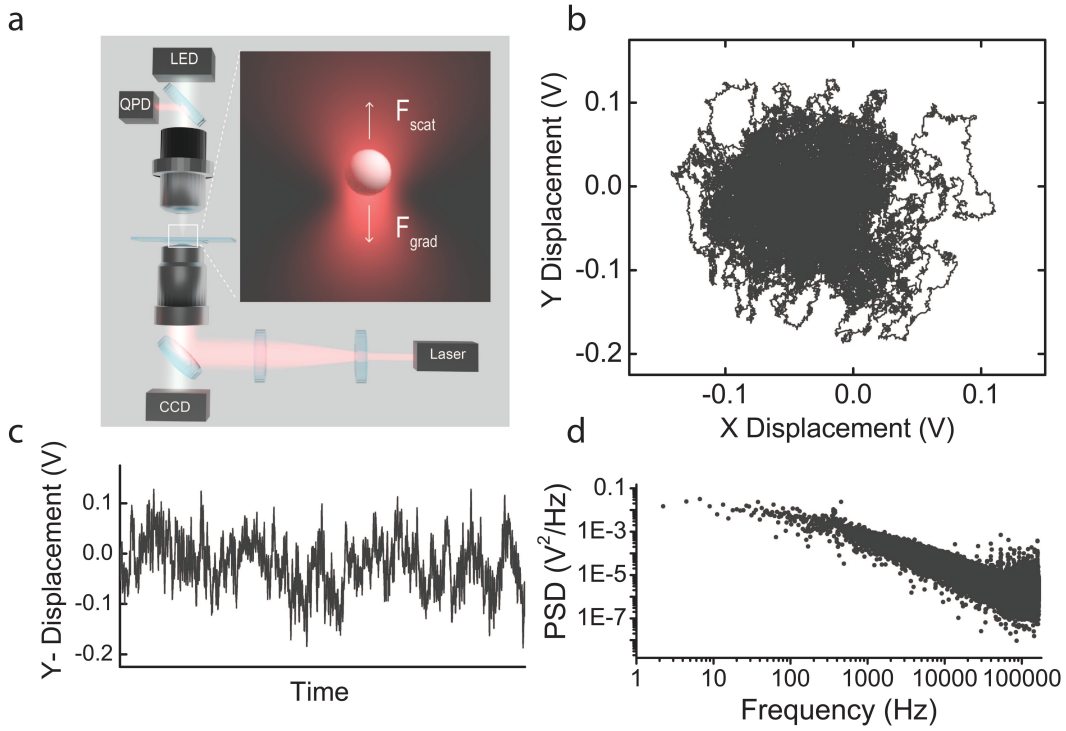

Figure 2.2: (a) Experimental setup of monitoring the Brownian motion of a microsphere trapped in water. (b) Microsphere position detected via the quadric photodiode (QPD). (c) Microsphere position versus time in one of the lateral direction. (d) Power spectrum of V(t) in (c).

scattered light from the trap is recorded. The particle displacement in time series is used to extract the local environment temperature.

Optical tweezers, also called laser tweezers, use a highly focused laser beam to trap dielectric nano- or micro-size particles with attractive forces arising from the difference in refractive index between the aqueous solution and particles. As shown in Figure 2.2a, the NIR laser is focused with 100x objective, and the particle is trapped inside the aqueous solution in the glass slide chamber. The forward scattered light is focused and collected by a quadrant photodiode (QPD).[45] A white LED light placed

behind the collection condenser illuminates the particles in Brownian motion, which can be observed live through the color CCD camera.

The nanoparticles suspended in an aqueous solution undergo Brownian motion. The NIR laser beam scatters off the trapped particles and creates a dynamics interference pattern on the QPD, which gives time-dependent particle displacement (Figure 2.2b and c). Then the photovoltage signal from the detector can be processed with Fourier transform to power spectra density (PSD, Figure 2.2d), which can be further processed to achieve the local surrounding aqueous solution temperature of the trapped particle.[46]

2.3.1 Temperature extraction

An experimental diffusion coefficient is extracted by fitting the characteristic function for the experimental power spectra derived in Berg-Sorensen and Flyvbjerg.[47] The cold Brownian motion (CBM) diffusion coefficient is then related to the CBM temperature by:

$$D_{\mathrm{CBM}} = \frac{k_{\mathrm{b}} T_{\mathrm{CBM}}}{\gamma_{\mathrm{CBM(T)}}} \tag{2.4}$$

where $\mathrm{D_{CBM}}$ is the CBM diffusion coefficient, kb is Boltzmanns constant, $\mathrm{T_{CBM}}$ is the CBM temperature, and $\gamma_{\mathrm{CBM(T)}}$ is the CBM Stokes drag. The CBM Stokes drag is given by

$$\gamma_{\mathrm{CBM(T)}} = 6\pi R \eta_{\mathrm{CBM(T)}} \tag{2.5}$$

where R is the particle radius, and $\eta_{\mathrm{CBM(T)}}$ is the temperature-dependent CBM viscosity.

To the leading order of the temperature increment or decrement Δ T = ($\mathrm{T_p}$ - $\mathrm{T_0}$), the temperature-dependence of the viscosity on $\mathrm{T_{CBM}}$ can be neglected, giving the

effective temperature[48]

$$T_{\mathrm{CBM}} = T_0 + \frac{5}{12}\Delta T \tag{2.6}$$

To account for the solvent viscosity temperature dependence, the methods of Reference[49] are followed and the Vogel-Fulcher-Tammann-Hesse law is used with the viscosity functional form η(T)=η_∞exp[A/((T-T_{VF}))], that is related to the viscosity of the solvent at room temperature,η_0, by

$$\frac{\eta_0}{\eta_{\mathrm{CBM(T)}}} \approx 1+\frac{193}{486}[ln(\frac{\eta_0}{\eta_\infty})][\frac{\Delta T}{(T_0 - T_{\mathrm{VF}})}]-[\frac{56}{243}ln(\frac{\eta_0}{\eta_\infty})-\frac{12563}{118098}ln^2(\frac{\eta_0}{\eta_\infty})][\frac{\Delta T}{(T_0 - T_{\mathrm{VF}})}]^2 \tag{2.7}$$

The VF viscosity parameters were fit to experimental data and are as follows:

D_2O, η_∞=3.456 x 10^{-5} Pa · s, A = 478.6 K, T_{VF} = 160 K, and

H_2O, η_∞=2.664 x 10^{-5} Pa · s, A = 536.5 K, TVF = 145.5 K. The non-uniform viscosity local viscosity distribution can also be measured using an inverse integral transformation method[50].

2.4 Optomechanical thermometry

In this technique, Young's modulus is the primary temperature-dependent observable.

For a beam freely suspended on the edge of a substrate, the resonant vibration frequency can be measured by collecting the forward scattered light transmitted through it using an avalanche photodiode. The time series photovoltage data is then Fourier transformed to obtain the frequency. The frequency f_i of the i^{th} mode of the cantilever of length L and thickness h as[51]

$$f_i = \frac{\beta_n^2}{4\sqrt{3}\pi}\frac{h}{L^2}\sqrt{\frac{E}{\rho}}, \tag{2.8}$$

for which the solutions β_n are given using

$$1 + \cos\beta_n \cosh\beta_n = 0. \tag{2.9}$$

where E is the Youngs modulus, ρ is the density.

Measurements of the fundamental acoustic eigenfrequency at low laser powers showed a red-shift in the eigenfrequency when temperature increases.

Although several parameters will have a temperature dependence, it has been shown[52] for cantilevers comprised of a single material that the dominating factor is the temperature dependence of Young's modulus. Other power-dependent effects of optical trapping stiffness are discussed in detail in Dr. Pant's dissertation[53].

Chapter 3

UPCONVERSION FLUORESCENCE THERMOMETRY

3.1 Introduction

The precise and accurate measurement of temperature is crucial for many advanced technological applications, including but not limited to microelectronics, bio-medicine, and aerospace[54]. Present technological demands in microelectronics and nanoelectronics, microfluidics, and nanophotonics, among others, have developed to the point that conventional contact thermal probes are no longer able to perform accurate measurements with sub-micron spatial resolution without detrimental electromagnetic interference. These increasing demands for accurate nanoscale thermometry have stimulated the development of novel non-contact thermal probes based on luminescence thermometry[55, 56, 57, 58, 59].

Luminescence thermometry based on trivalent lanthanide ions has increased in popularity over the last several years due to the unique versatility, stability, and narrow emission band profiles of the ions that cover the entire electromagnetic spectrum with relatively high emission quantum yields[54, 60]. Changes in luminescence features such as intensity, bandwidth, spectral shift, lifetime, and polarization are possible effects caused by temperature variations. Among them, luminescence intensity ratio (LIR, sometimes referred to as fluorescence intensity ratio, FIR, when transitions obey the spin selection rule) and luminescence lifetime are the two most promising luminescence-based temperature sensing techniques. In LIR thermometry, the change in the intensity ratio of two transitions is used to measure temperature[61]. The LIR (Δ) is defined in Eq.3.1 using the emission intensities (photons per unit time)

of the |2> |0> and |1> |0> transitions, where |0> denotes the ground level and |1> and |2> the two thermally coupled excited levels (level |2> is more energetic than level |1>)

$$\Delta = \frac{I_2}{I_1} = \frac{A_{02}N_2}{A_{01}N_1}. \tag{3.1}$$

Here, N_1 and N_2 are the populations of levels |1> and |2>. A_{01} and A_{02} are the total spontaneous emission rate constants from levels |1> and |2> to level |0>. The populations N_1 and N_2, are related by

$$\frac{N_2}{N_1} = \frac{g_2}{g_1} exp(-\frac{\delta E}{k_B T}), \tag{3.2}$$

where g_1 and g_2 are the degeneracies of the two levels and δE is the energy gap between the barycenters of the |1> |0> and |2> |0> emission bands. Consequently, the population in N_2 is small if $\delta E \gg kT$. Typically, the two excited states are considered to be thermally coupled (i.e., in a thermodynamic quasi-equilibrium state) for δE ranging from 200 to 2000 cm^{-1}[62]. The temperature can be expressed as

$$\frac{1}{T} = -\frac{k_B}{\delta E}(ln\Delta - lnB), \tag{3.3}$$

where B is $\frac{A_{01}g_1}{A_{02}g_2}$. Both the B and δE parameters can be extracted following temperature calibrations.

The most common upconversion (UC) systems for LIR thermometry are based on Yb^{3+} as a sensitizer and Er^{3+} as an activator. Yb^{3+} acts as an effective sensitizer with a large absorption cross-section at 980 nm, a wavelength easily available due to its use in the telecommunications industry for pumping erbium-doped fiber amplifiers. This wavelength also is widely used in biological systems because it lies in the tissue penetration window.[57] Furthermore, the Yb^{3+} excited state energy level matches

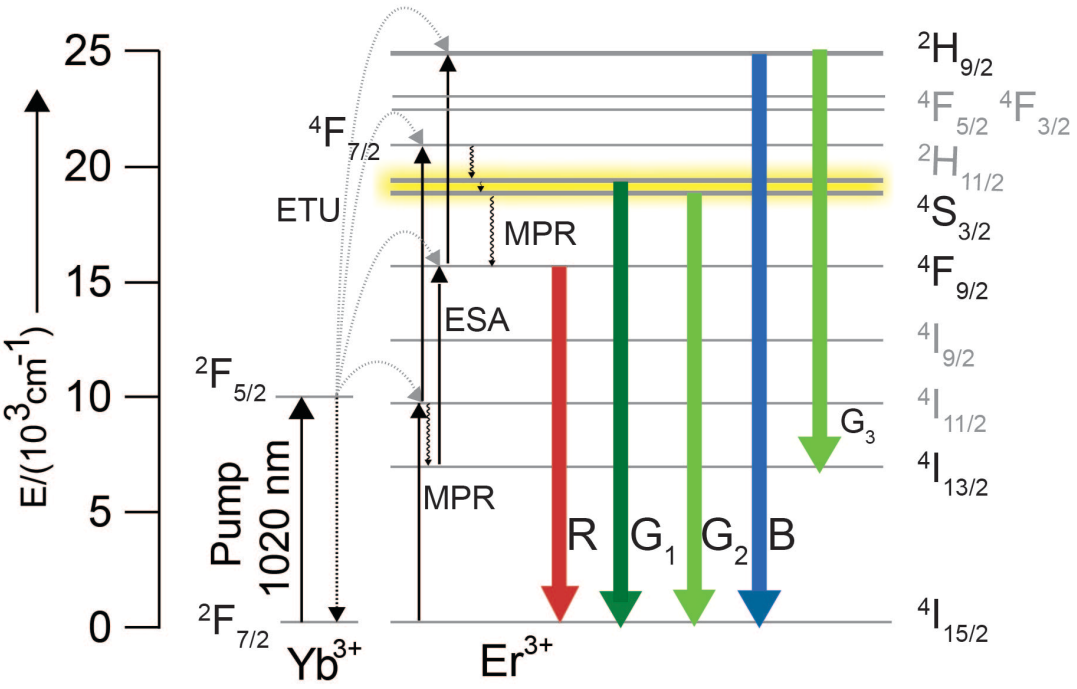

Figure 3.1: Schematic diagram of Yb-Er energy levels. The upconverted luminescence involves green emissions from the thermally coupled $^2H_{11/2}$ and $^4S_{3/2}$ states for LIR thermometry (G_1 and G_2, respectively), red emission (R) from the $^4F_{9/2}$ state, and blue emission (B) from the $^2H_{9/2}$ state. The alternative relaxation of $^2H_{9/2}$ to the intermediate state $^4I_{13/2}$ also emits green light G_3, overlapping with G_1 and G_2.ESA and MPR are excited-state absorption and multi-phonon relaxation, respectively. Copyright ©2021 Elsevier.

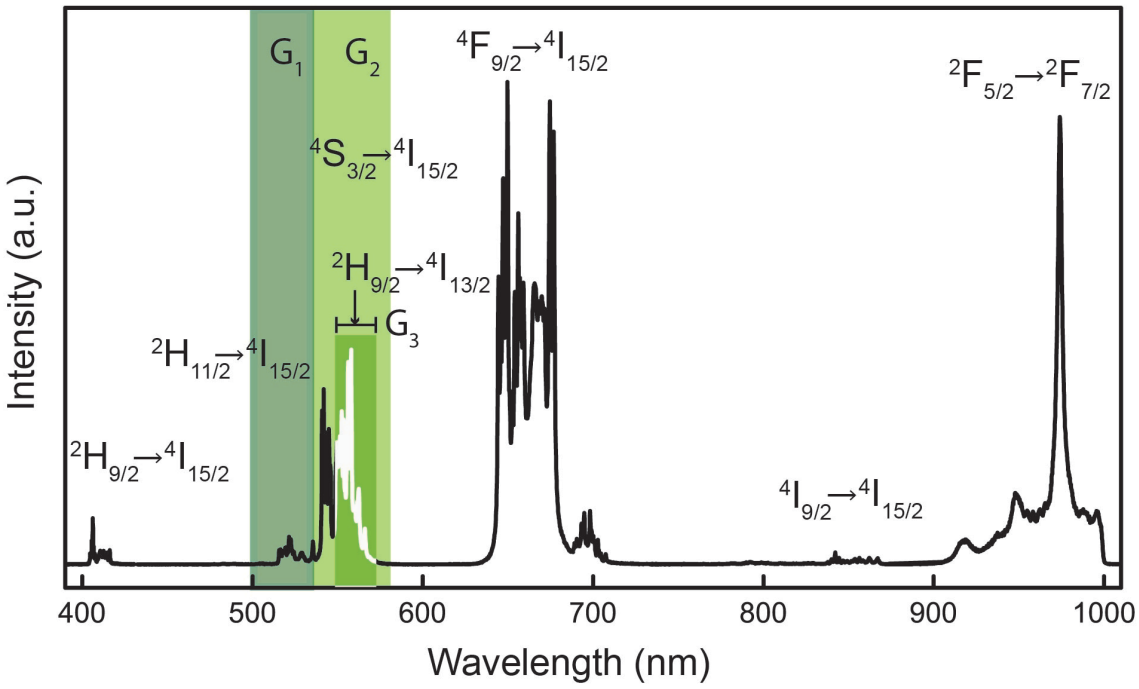

Figure 3.2: Representative PL spectrum of a K_2LuF_5:10%Yb,0.5%Er doped crystal. The two green emission bands G_1 and G_2 for LIR analysis are highlighted. Copyright ©2021 Elsevier.

well with the excited states of Er^{3+} ions, allowing a sequence of near-resonant energy transfers and the resulting stepwise excitation of Er^{3+} (Figure 3.1). As an activator, Er^{3+} is one of the widely used ions due to its highly temperature-dependent and intense green emission arising from the thermally coupled $^2H_{11/2}$ and $^4S_{3/2}$ states, whose separation is about 800 cm^{-1}[63]. The combination of Yb^{3+}/Er^{3+} is extensively used in a variety of host materials for LIR thermometry and their sensitivities are compared in the following references[64, 65, 66, 67].

The intensity ratio of the $^2H_{11/2} \rightarrow ^4I_{15/2}$ emission (labelled G_1 in Figure 3.2 at λ = 510-530 nm) and $^4S_{3/2} \rightarrow ^4I_{15/2}$ emission (labelled G_2 in Figure 3.2 at λ = 535570 nm) is utilized to determine the temperature of UC crystals. In addition to the

green transitions, there are red, blue, and sometimes ultra-violet transitions as well, depending on lanthanide concentrations and also the lattice structures of the host materials. The blue and UV emissions, which require high UC efficiencies, are usually weaker than the green or red emissions. For some UC crystals, the intensity ratio of the red and green emission bands is also used for optical thermometry[68].

The $^2H_{9/2}$ state, which emits blue light if it relaxes to the ground state, can also emit green light if it branches to the intermediate $^4I_{13/2}$ excited state. Such green emission from the $^2H_{9/2} \rightarrow ^4I_{13/2}$ transition will interfere with the ratiometric thermometry bands and cause an inaccurate temperature readout. However, this has not been discussed extensively in the literature[69, 70]. Renero *et al.* did spectroscopic characterizations of this emission in the hexagonal phase $NaYF_4$ but quantifying the impact of this $^2H_{9/2} \rightarrow ^4I_{13/2}$ emission in the context of optical thermometry has been limited[71]. In this work, we have characterized the impact of Er^{3+} $^2H_{9/2} \rightarrow ^4I_{13/2}$ emission on all-optical thermometry, including the interplay between upconversion pathways involving Er^{3+} $^4F_{9/2}$, $^2H_{11/2}$, $^4S_{3/2}$, and $^2H_{9/2}$ states.

3.2 Experimental

Materials: K_2LuF_5:x%Yb, 0.5%Er ($x = 0$ - 99) microcrystals were synthesized as described previously[72]. Briefly, lutetium nitrate hexahydrate ($Lu(NO_3{\cdot}6H_2O)_3$) and ytterbium nitrate hexahydrate ($Yb(NO_3)_3{\cdot}6H_2O$) were of 99.99% purity and purchased from Sigma-Aldrich. Potassium hydroxide (KOH), potassium fluoride (KF), ethanol, and oleic acid were analytical grade purchased from Sigma-Aldrich and used without further purification. 18.2 M$\Omega{\cdot}cm$ Milli-Q deionized water was used for each synthesis. For a typical synthesis, 420.8 mg of KOH was dissolved in 1.5 mL of water, followed by 5 mL of ethanol and 5 mL of oleic acid with stirring. Then, 1.6 mL of 0.5M $RE(NO_3)_3$ were added into the mixture. After stirring for 10 min, 1.89 g KF

was dissolved in 3 mL water and added to the mixture dropwise. After additional agitation for 10 min, the resulting mixture was transferred to a 23 mL Teflon-lined autoclave and heated at 220°C for 24 hours. After the autoclave cooled to room temperature, crystals were isolated by washing and centrifuging by ethanol and water three times. After drying the product at 60°C for 12 hours, they were transferred to a Lindberg Blue tube furnace and heated at 300°C in air for 2 hours to remove any residual organic surface ligands. The purity of the obtained compounds was confirmed by XRD.

Spectroscopic Measurements: NIR upconversion excitation at 1020 nm was provided by fiber-coupled single-mode laser diodes (QPhotonics, QFBGLD-1020-400). Direct excitation of $^4S_{3/2}$ state at 532 nm was provided by a single longitudinal mode laser (Coherent Compass 532). Direct excitation of $^2H_{9/2}$ state at 375 nm was provided by a Xe-lamp coupled to an Acton SpectraPro 300i monochromator. Emission spectra were acquired with an Acton SpectraPro 500i spectrograph with a Princeton liquid-nitrogen-cooled Si detector. Various excitation lasers were focused to a diffraction-limited spot (radius = 1.2 μm) using a long working distance 50X objective (Mitutoyo, M Plan Apo). Photoluminescence was collected by the same objective. Six spectra, collected for 0.5 ms each, were averaged to obtain the final PL spectrum.

Absorption spectra were collected using an Agilent Cary 5000 UV-Vis-NIR spectrometer with the sample powder loaded into a helium flow cryostat and cooled to around 80 K.

Time-resolved emission was generated with pulsed 1020 nm excitation. A Tektronics function generator was used to control the laser diode and generate laser pulses of 0.1 ms duration with a frequency of 10Hz. An avalanche photodiode detector (Thorlabs APD430A) was used to collect the luminescence decay signal.

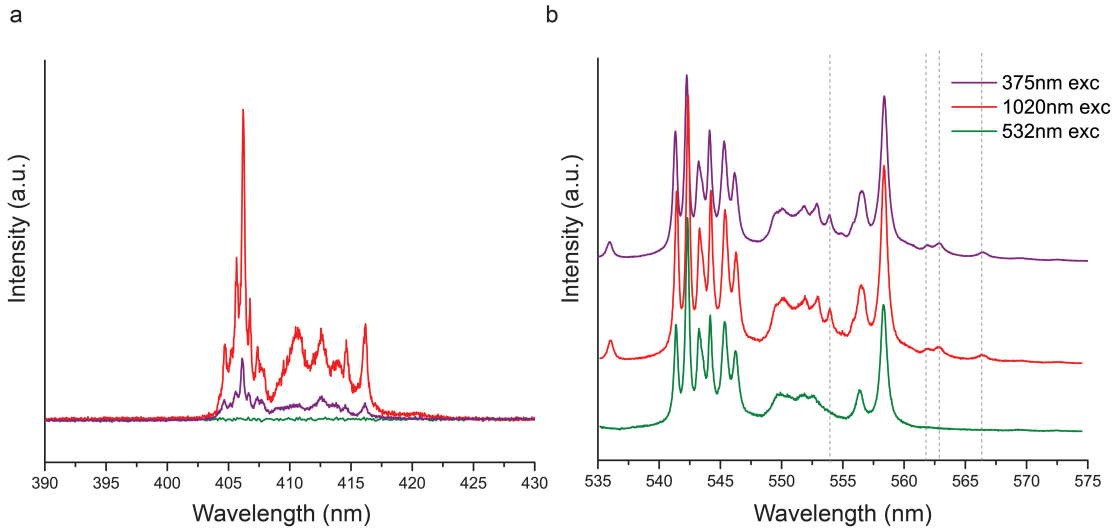

Figure 3.3: PL spectra of a K_2LuF_5:10%Yb, 0.5% Er crystal with 1020 nm (red), 375 nm (purple), and 532 nm (green) excitations at (a) 400 nm 420 nm ($^2H_{9/2} \rightarrow ^4I_{15/2}$) and (b) 535 nm 570 nm ($^2H_{9/2} \rightarrow ^4I_{13/2}$) wavelength ranges. Copyright ©2021 Elsevier.

3.3 Results and discussion

3.3.1 $^2H_{9/2} \rightarrow ^4I_{13/2}$ transition

The UC material used in this work is Yb/Er co-doped K_2LuF_5. Figure 3.3 and Figure 3.4 show the photoluminescence (PL) spectra of a K_2LuF_5:10%Yb, 0.5%Er crystal and absorption of K_2ErF_5. The blue emission (400 - 420 nm) in Figure 3.3a confirms a population of excited $^2H_{9/2}$ states created following NIR excitation. It can relax to the $^4I_{15/2}$ ground state and $^4I_{13/2}$ intermediate excited state, emitting blue and green light, respectively. However, such green emission is difficult to characterize because it overlaps with the $^2H_{11/2} \rightarrow ^4I_{15/2}$ and $^4S_{3/2} \rightarrow ^4I_{15/2}$ emissions of Er^{3+}. To uniquely assign the additional green emission from $^2H_{9/2} \rightarrow ^4I_{13/2}$ transition in this upconversion process, PL of the same sample excited by 375 nm and 532 nm laser

were provided in Figure 3.3 as well. Figure 3.3a shows that the $^2H_{9/2}$ state can be populated upon direct excitation with 375 nm light, whose photon energy is slightly higher than $^2H_{9/2}$. It can also be populated through NIR upconversion with 1020 nm excitation. However, there is no emission observed with 532 nm excitation because the excitation energy is either too low for the direct excitation or too high to accomplish multi-photon upconversion. Although the 532 nm laser is not sufficient to excite the $^2H_{9/2}$ directly, it can excite the $^2H_{11/2}$ and $^4S_{3/2}$ states, whose energy levels are lower than $^2H_{9/2}$. Therefore, the green emission upon 532 nm excitation is solely from the $^2H_{11/2} \rightarrow ^4I_{15/2}$ and $^4S_{3/2} \rightarrow ^4I_{15/2}$ transitions without any potential overlap with the $^2H_{9/2} \rightarrow ^4I_{13/2}$ emission (Figure 3.3b). In contrast, for both 375 nm and 1020 nm excitation wavelengths, there are additional peaks compared to the PL with 532 nm excitation, highlighted by the vertical dashed lines in Figure 3.3b. Since the two excitations can populate the $^2H_{9/2}$ state, these additional peaks must be related to $^2H_{9/2} \rightarrow ^4I_{13/2}$ transition.

Crucially, the absence of corresponding absorption peaks in Figure 3.4 (red arrows) confirms the nature of this emission from a higher excited state to an intermediate excited state, instead of relaxing to the ground state. At room temperature, all of the Er^{3+} ions are in the $^4I_{15/2}$ ground state. There is no absorption from the intermediate excited state to a higher excited state. This demonstrates why the emission from the $^2H_{9/2} \rightarrow ^4I_{13/2}$ transition lacks the corresponding absorption in the same wavelength range while emission and absorption peaks are well matched for the $^2H_{11/2} \rightarrow ^4I_{15/2}$ and $^4S_{3/2} \rightarrow ^4I_{15/2}$ transitions.

The relative intensity of these peaks compared to the $^2H_{11/2} \rightarrow ^4I_{15/2}$ and $^4S_{3/2} \rightarrow ^4I_{15/2}$ increases with the ytterbium doping concentration. The $^2H_{9/2} \rightarrow ^4I_{13/2}$ emission stands out at high Yb^{3+} concentrations, which helps identify all possible $^2H_{9/2} \rightarrow ^4I_{13/2}$ peaks. In Figure 3.5a, thirteen peaks have been assigned to the $^2H_{9/2} \rightarrow ^4I_{13/2}$

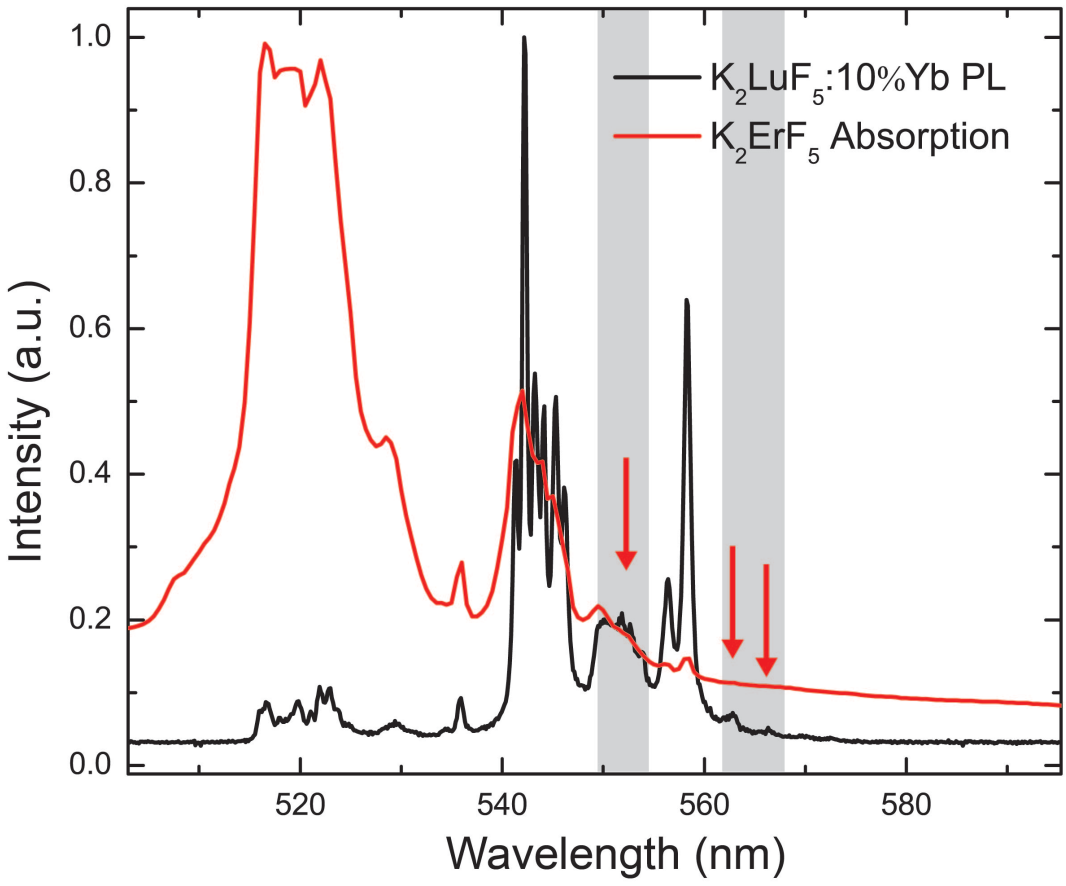

Figure 3.4: PL from a K_2LuF_5:10%Yb, 0.5% Er crystal with an excitation laser of 1020 nm (black) and absorption of a K_2ErF_5 pellet (red). PL in 560 nm - 570 nm range (highlighted by red arrows) lacks corresponding absorption peaks, suggesting the emission from a higher excited state to an intermediate excited state. Copyright ©2021 Elsevier.

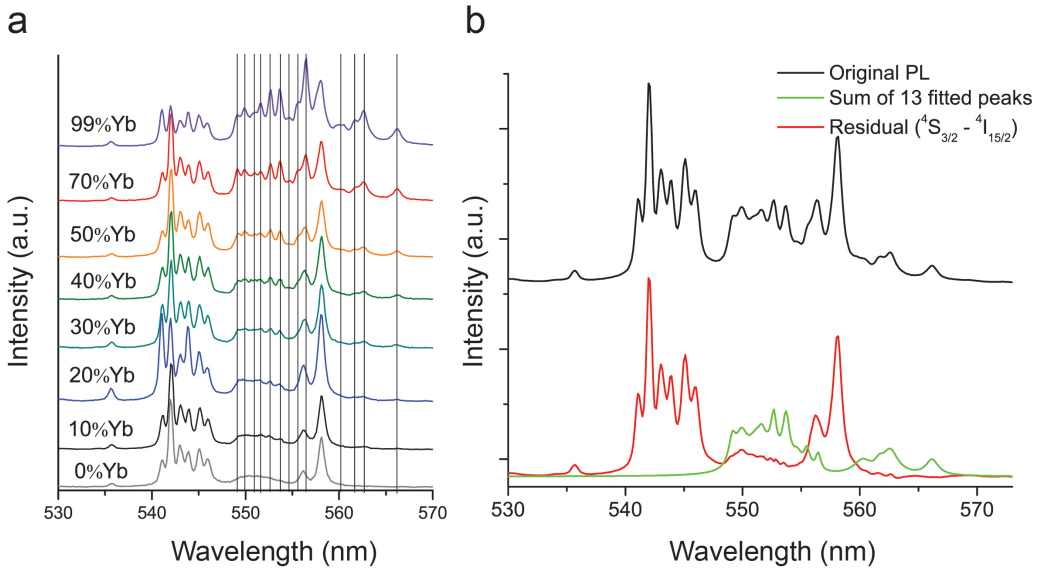

Figure 3.5: (a) Er PL with increased Yb^{3+} concentration. Additional peaks arise in 550 nm - 570 nm range with higher Yb dopant concentration. All PL were collected with a very low irradiance. (b) Fitting and subtraction of the additional peaks in (a) After subtraction, the PL is the same as 0% Yb, 0.5% Er doped sample.

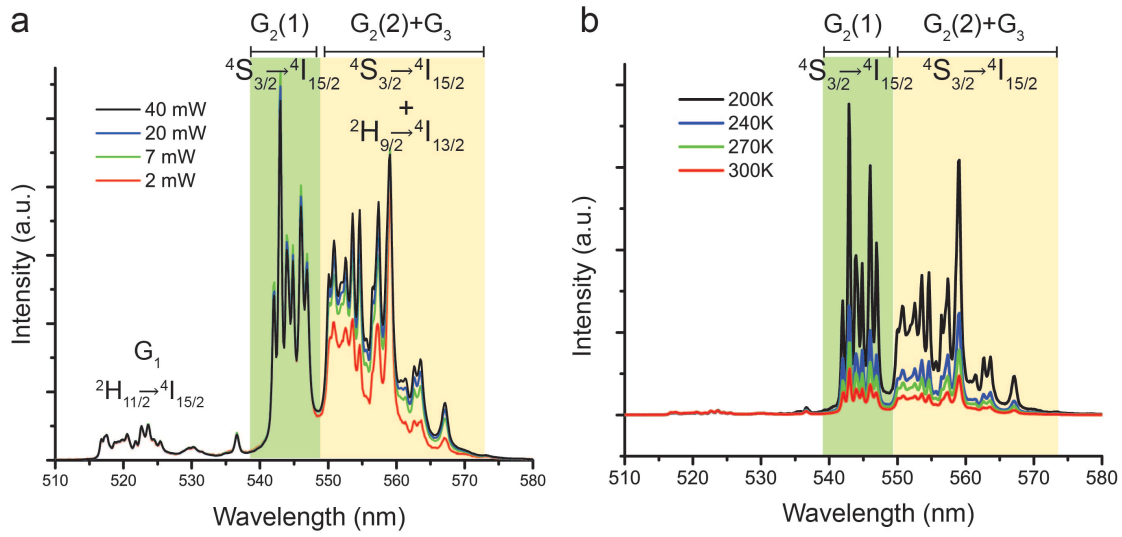

Figure 3.6: (a) Er^{3+} PL excited by various laser powers. (b) Er^{3+} PL at different temperatures. The excitation power is kept at 2 mW. The relative intensity $G_2(1)$, $G_2(2)$ and G_3 to the G_1 share similar response to temperature. All spectra in (a) and (b) are normalized by the intensity of $^2H_{11/2} \rightarrow ^4I_{15/2}$ emission (G_1). With high excitation powers, the normalized intensity of the first half of $^4S_{3/2} \rightarrow ^4I_{15/2}$ emission ($G_2(1)$) remains the same, while the second half of $^4S_{3/2} \rightarrow ^4I_{15/2}$ emission ($G_2(2)$) and $^2H_{9/2} \rightarrow ^4I_{13/2}$ emission (G_3) increase.

transition by comparing the emission with different Yb^{3+} concentrations. Besides these peaks, a total of 26 peaks in the green spectral region between 530 nm and 570 nm are identified and Lorentzian fitted to obtain the center wavelengths and FWHM parameters of the $^2H_{9/2} \rightarrow ^4I_{13/2}$ emission for further subtraction from the raw overlapping PL spectrum. Figure 3.5b shows the sum of 13 fitted Lorentzian peaks (green) from $^2H_{9/2} \rightarrow ^4I_{13/2}$ emission. Residual emission (red) following the subtraction of $^2H_{9/2} \rightarrow ^4I_{13/2}$ peaks is identical to the PL with 532 nm excitation (Figure 3.3b) and the PL from samples without Yb dopant ions (Figure 3.5a), indicating emission solely from the $^4S_{3/2} \rightarrow ^4I_{15/2}$ transition.

3.3.2 Power- and temperature- dependence

Emission from the $^2H_{9/2} \rightarrow ^4I_{13/2}$ transition has a different power dependence from the $^2H_{11/2} \rightarrow ^4I_{15/2}$ and $^4S_{3/2} \rightarrow ^4I_{15/2}$ transitions that are widely used in LIR thermometry. Figure 3.6a plots Er^{3+} PL at various excitation powers. All spectra are normalized by the maximum intensity of the $^2H_{11/2} \rightarrow ^4I_{15/2}$ (G_1) emission at 523 nm. The emission between 539 nm and 549 nm is assigned only to the $^4S_{3/2} \rightarrow ^4I_{15/2}$ transition labeled $G_2(1)$, not affected by the $^2H_{9/2} \rightarrow ^4I_{13/2}$ emission. The spectral range between 550 nm to 570nm arises from overlapping $^4S_{3/2} \rightarrow ^4I_{15/2}$ and $^2H_{9/2} \rightarrow ^4I_{13/2}$ transitions labeled $G_2(2)+G_3$. The emission intensities for both the G_1 and $G_2(1)$ regions have the same power dependence while the mixed $G_2(2)+G_3$ emission intensity increases much more rapidly. Temperature-dependent Er^{3+} PL in Figure 3.6b confirms such different intensity responses of $G_2(1)$ and $G_2(2)+G_3$ to excitation powers in Figure 3.6a are not caused by radiation-induced internal temperature changes, because the relative intensity of both $G_2(1)$ and $G_2(2)+G_3$ have the same response to temperature. Consequently, the observed power dependence of the overlapping $^2H_{9/2} \rightarrow ^4I_{13/2}$ emission will cause significant complications for non-contact optical thermometry using Er^{3+} ions, discussed in more detail below.

To evaluate the impact of $^2H_{9/2} \rightarrow ^4I_{13/2}$ emission on erbium-based LIR thermometry, LIR response as a function of temperature was measured with KLF samples sealed in a cryostat. Figure 3.7a illustrates the experimental setup. During the temperature calibration measurement, the laser irradiance was kept constant to a low value (3 kW/cm^2) in order to minimize any photothermal effects from the laser. Logarithms of PL intensity ratios as a function of the reciprocal of temperature are given in Figure 3.7b, where the linear fittings are used to interpret the temperatures of the same sample with increasing excitation irradiance in Figure 3.7c. Two ratios with different sets of wavelength intervals are used in the temperature calibration, namely

G_1/G_2 and $G_1/(G_2+G_3)$, where G refers to the integrated green PL over the specified range. The $^2H_{11/2} \rightarrow ^4I_{15/2}$ interval is 515 nm 530 nm (G_1) for both analyses, while two different intervals of $^4S_{3/2} \rightarrow ^4I_{15/2}$ emission are used. In the first analysis, the exclusive $^4S_{3/2} \rightarrow ^4I_{15/2}$ emission between 540 nm to 549 nm is used. The second analysis, 540 - 570 nm, is used to cover the full $^4S_{3/2} \rightarrow ^4I_{15/2}$ emission, which overlaps with the $^2H_{9/2} \rightarrow ^4I_{13/2}$ emission G_3.

The two calibration methods based on different wavelength intervals have similar slopes. However, their LIR responses are observed to differ significantly as a function of laser irradiance. In Figure 3.7c, the temperature interpreted from the G_1/G_2 ratio indicates heating when the KLF crystal is pumped with increasing laser irradiance. However, if the LIR analysis includes emission from the overlapping $^2H_{9/2} \rightarrow ^4I_{13/2}$ transition, namely $G_1/(G_2+G_3)$, then an opposite cooling trend is observed, which contradicts with the result without $^2H_{9/2} \rightarrow ^4I_{13/2}$ overlap. Increasing excitation power is used here because the internal temperature change, no matter heating or cooling, is positively correlated to power density[73]. At the low irradiances (< 0.1 MW·cm^{-2}) of 1020 nm laser, the spectral overlap has a negligible effect. However, at the higher laser irradiances used for laser cooling, the effect becomes important (Figure 3.7c) despite the lower absorption coefficient of Yb(III) ions at the laser cooling excitation wavelength of 1020 nm. Typically, irradiance of 1-100 W·cm^{-2}([54, 59]) is used for luminescence thermometry at the excitation wavelength of 980 nm. Such spectral overlap may be negligible considering the low irradiances. However, the absorption coefficient of Yb(III) ions at 980 nm is much higher than 1020 nm used in this work, which may result in non-negligible spectral overlap even at low irradiances.

Similar measurements were performed on crystals with various Yb^{3+} concentrations in order to further evaluate the impact of $^2H_{9/2}$ upconversion on LIR thermometry. A decrease in the $G_1/(G_2+G_3)$ ratio was observed in samples as Yb^{3+}

concentrations were increased from 10% to 99% (Figure 3.7d). A simple consideration of this decrease in the
$G_1/(G_2+G_3)$ ratio would indicate that solid state laser cooing is possible at Yb doping levels of 99%. However, to the best of our knowledge the laser refrigeration of crystals with Yb^{3+} concentration higher than 10% has never been reported in the literature[74, 75] due to non-radiative relaxation that stems from concentration quenching. The measured lifetime of Yb^{3+} also decreases with increased Yb^{3+} concentration, consistent with prior reports of concentration quenching at elevated Yb^{3+} concentrations[74]. These lifetime data contradict the simple interpretation of laser cooling based on the $G_1/(G_2+G_3)$ ratio.

The observations above highlight the crucial importance of using the $^4S_{3/2} \rightarrow ^4I_{15/2}$ emission without overlapping $^2H_{9/2} \rightarrow ^4I_{13/2}$ emission in LIR thermometry based on Er^{3+} ions. The major impact that the $^2H_{9/2} \rightarrow ^4I_{13/2}$ transition has on Er^{3+} based optical thermometry arises from the different upconversion mechanisms of $^2H_{9/2}$ from $^2H_{11/2}$ and $^4S_{3/2}$ states. During the energy transfer up-conversion (ETU), one excited Yb^{3+} ion relaxes to its ground state while simultaneously exciting an Er^{3+} ion. This ETU process can occur several times in succession, resulting in an Er^{3+} ion excited to the $^2H_{9/2}$ state, which is reached after at least three energy transfer steps with a similar excitation wavelength[76].

The number of energy-transfer steps, or photons required in the upconversion process, can be studied by measuring the emission intensity at various powers. Although it is difficult to characterize the $^2H_{9/2} \rightarrow ^4I_{13/2}$ transition due to overlap with other emissions, the blue emission around 410 nm from the same $^2H_{9/2}$ excited state can be measured to study its upconversion mechanisms. The slopes of the double logarithmic plots of red, green, and blue emission in Figure 3.8b suggest that the $^2H_{9/2}$ upconversion is a 3- or 4-photon process, while the $^2H_{11/2}$ and $^4S_{3/2}$ upconversions

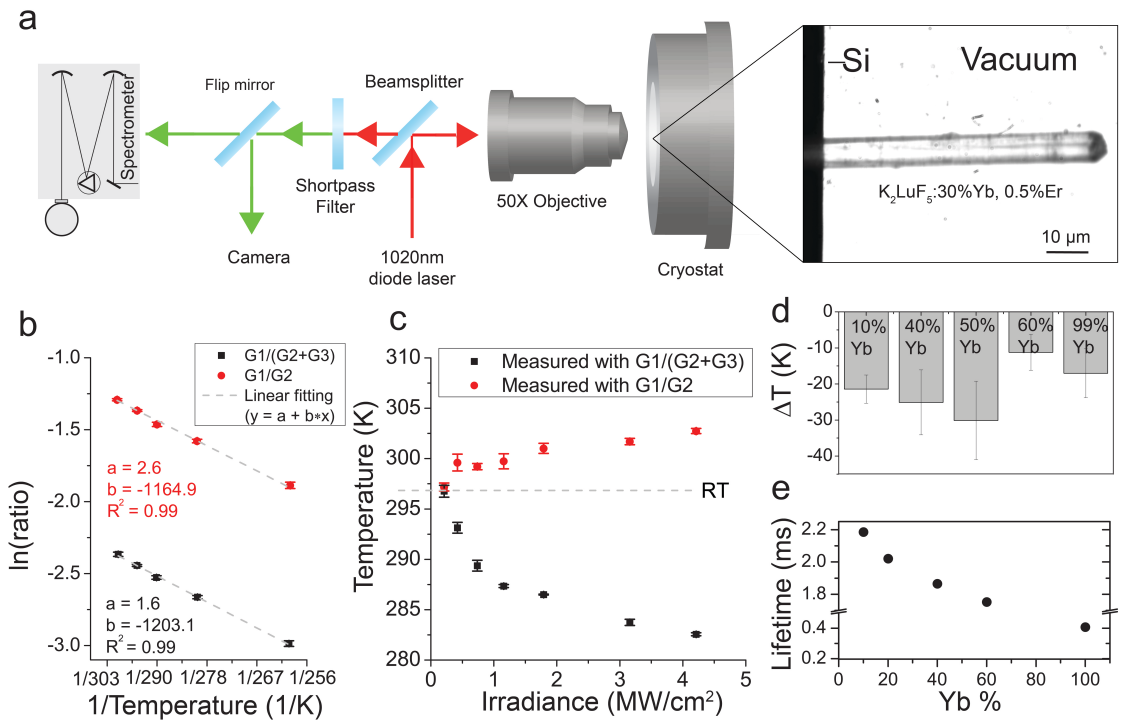

Figure 3.7: (a) PL measurement setup. (b) Temperature calibrations using ratios of the $^2H_{11/2} \rightarrow ^4I_{15/2}$ emission intensity to the total intensity of $^4S_{3/2} \rightarrow ^4I_{15/2}$ full emission overlapping with $^2H_{9/2} \rightarrow ^4I_{13/2}$ emission ($\ln[G_1/(G_2+G_3)]$, black), and to the first half of $^4S_{3/2} \rightarrow ^4I_{15/2}$ emission without additional $^2H_{9/2} \rightarrow ^4I_{13/2}$ emission overlap ($\ln[G_1/G_2)]$, red). (c) Calibrated temperatures of the crystal excited by increased 1020 nm laser power with two different Er^{3+} PL ranges. The selection of wavelength intervals results in opposite temperature interpretations. (d) The misinterpreted temperatures of K_2LuF_5:0.5%Er/x%Yb crystals doped with various Yb concentrations using intensity ratios of $G_1/(G_2+G_3)$. (e) Decreasing lifetime of the Yb^{3+} $^2F_{5/2}$ state of K_2LuF_5crystals with increasing Yb% due to concentration quenching.

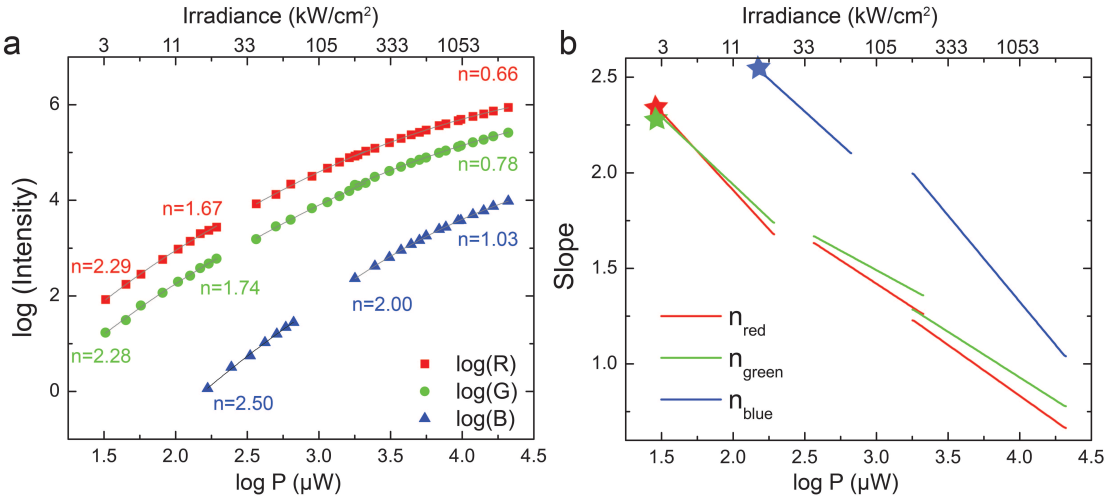

Figure 3.8: (a) Double logarithmic plots of red, green, and blue emission intensities versus 1020 nm laser power. (b). The slopes of the double logarithmic plots. The higher slope of the blue emission compared to the green emission suggests the different power response of $^2H_{9/2} \rightarrow ^4I_{13/2}$ from other $^2H_{11/2} \rightarrow ^4I_{15/2}$ and $^4S_{3/2} \rightarrow ^4I_{15/2}$ green emissions. The population of the $^2H_{9/2}$ excited state involves 3- or 4-photon upconversion.

are 2- or 3-photon process. Although it is challenging to quantify the exact number of photons in these upconversion processes, the slope of blue emission is always higher than that of green and red emissions. The different amounts of photons required agree with power-dependent measurements performed with 1.54 μm excitation showing that ground state luminescence from $^2H_{9/2}$ and $^4S_{3/2}$ involve 4-photon and 3-photon upconversion, respectively[77].

There are different possible upconversion pathways to the $^2H_{9/2}$ state[78]. The most accepted one proposes that the $^4F_{9/2}$ level is the initial state in the energy transfer step leading to the $^2H_{9/2}$ state[79, 80, 81]. Therefore, upconversion to $^2H_{9/2}$ requires at least one more photon than to the $^4F_{9/2}$, $^2H_{11/2}$, and $^4S_{3/2}$ levels. This explains the larger slope of $^2H_{9/2} \rightarrow ^4I_{13/2}$ emission in the 550 nm 570 nm spectral region in comparison with the $^2H_{11/2} \rightarrow ^4I_{15/2}$ and $^4S_{3/2} \rightarrow ^4I_{15/2}$ transitions with increasing excitation power. If the $^2H_{9/2} \rightarrow ^4I_{13/2}$ emission is included in the LIR analysis, it will lead to an incorrect interpretation of the temperature. The same problem arises for Er^{3+} thermometry using red / green emission ratios[68].

3.3.3 Implications for Yb/Er LIR thermometry

In recent years more advanced LIR techniques have been reported based on temperature-dependent luminescence intensity distributions, such as differential luminescence thermometry that monitors time-differencing luminescence[40]. However, the wavelength overlap of $^4S_{3/2} \rightarrow ^4I_{15/2}$ and $^2H_{9/2} \rightarrow ^4I_{13/2}$ emissions cannot be avoided. Careful wavelength interval selection or $^2H_{9/2} \rightarrow ^4I_{13/2}$ emission subtraction must be made for accurate temperature measurement. Perhaps the best solution is to fix the pump power and avoid a power-dependent temperature measurement. However, for some applications, such as examining the cooling properties of micro- or nano-size laser cooling materials, a power-dependent measurement cannot be avoided. A pump-

probe method in a confocal system[57] can be applied that an additional constant power probe laser is used, and only the PL excited by the probe laser is collected via the confocal setup.

The host materials and dopant concentrations must also be considered. Overlap of $^2H_{9/2} \rightarrow ^4I_{13/2}$ and $^4S_{3/2} \rightarrow ^4I_{15/2}$ emissions is also observed in other popular fluoride host materials such as $NaYF_4$[70, 57] and $LiYF_4$, and in oxide host materials[69]. Recent work suggests that the lattice phonon energy strongly affects the red emission intensity and also the energy transfer efficiency to the $^4F_{9/2}$ [82, 81], which is the intermediate excited state before upconverting to the $^2H_{9/2}$ state. Host materials with low lattice phonon energies are preferred. The sensitizer Yb^{3+} concentration should be lower than 20% to avoid energy clustering, i.e., the excitation energy is preserved in a sub-lattice domain of Yb^{3+} clusters, which enhances upconversion to $^2H_{9/2}$ [83].

3.4 Conclusion

We have demonstrated the existence of $^2H_{9/2} \rightarrow ^4I_{13/2}$ green PL in Yb^{3+}/Er^{3+} co-doped K_2LuF_5. At room temperature, this emission covers a wide wavelength range (545 nm to 570 nm) such that it overlaps the $^4S_{3/2} \rightarrow ^4I_{15/2}$ emission. Peaks at 560 nm - 570 nm do not overlap with other transitions and are characteristics of $^2H_{9/2} \rightarrow ^4I_{13/2}$ emission. Such emission exists not only in K_2LuF_5 microcrystals but also other Yb^{3+}/Er^{3+} co-doped fluoride and oxide materials.

We have shown that $^2H_{9/2} \rightarrow ^4I_{13/2}$ emission is more sensitive to pump power than $^2H_{11/2} \rightarrow ^4I_{15/2}$ and $^4S_{3/2} \rightarrow ^4I_{15/2}$ emission because it requires more energy-transfer steps during upconversion. It leads to incorrect temperature readout when this emission is included in the LIR analysis, especially when high pump powers are used.

Finally, we conclude that the LIR wavelength intervals need to be examined care-

fully to avoid the overlapping emission from $^2H_{9/2} \rightarrow ^4I_{13/2}$. Suggestions have been made on optical experimental setup and selection of host materials and dopant concentrations.

Chapter 4

SYNTHESIS AND CHARACTERIZATION OF POTASSIUM LUTETIUM FLUORIDE (KLF) MICROCRYSTALS

4.1 Introduction

Among the laser cooling crystals, $YLiF_4$ is the best-studied material as it set the cooling record of 91K for solid-state refrigeration. Beyond $YLiF_4$, advances are quickly being made with other host materials within the alkali-RE-fluoride family. Recently $NaYF_4$ nanowires were reported to achieve internal laser cooling within an aqueous solution[17]. Laser cooling of bulk KYF_4 crystals has also been observed[11] using Czochralski crystal growth. This work investigates a novel hydrothermal route to synthesize potassium-RE-fluoride phases that are challenging to grow using bulk crystal growth methods.

Within the alkali-RE-fluoride family, potassium-based materials have been studied less than their Na and Li counterparts, due in part to the complexity of the potassium-lutetium-fluoride phase diagram. The investigation of $(KF)_x{\cdot}(REF_3)_y$ systems started over half a century ago[84] and five stable crystallographic phases are known including K_3REF_6, K_2REF_5, $KREF_4$, KRE_2F_7, and KRE_3F_{10}[85, 86]. In bulk Czochralski or Bridgman growth, only two stable phases, $KREF_4$ and KRE_3F_{10}, can be synthesized[86], with the rest only accessible through other post-synthetic modifications. This multitude of phases can been represented by writing the stoichiometric formulae in a binary form as $(KF)_x{\cdot}(REF_3)_y$. Changing the KF/REF_3 binary compound ratio results in different crystalline structures. This observation has at-

tracted interest in potassium-RE-fluoride and their application of laser cooling, as other members in this family, such as $LiYF_4$ (tetragonal phase) and $NaYF_4$ (α-cubic and β-hexagonal phases), are known to have only one stoichiometry. Beyond the diversity of phases, recent work has also explored replacing the common host element yttrium with lutetium[10], as the lutetium-lithium-fluoride phase diagram exhibits congruent melting[87]. There is also a close match in cation size between Lu^{3+} (861 pm) and Yb^{3+} (868 pm)[88].

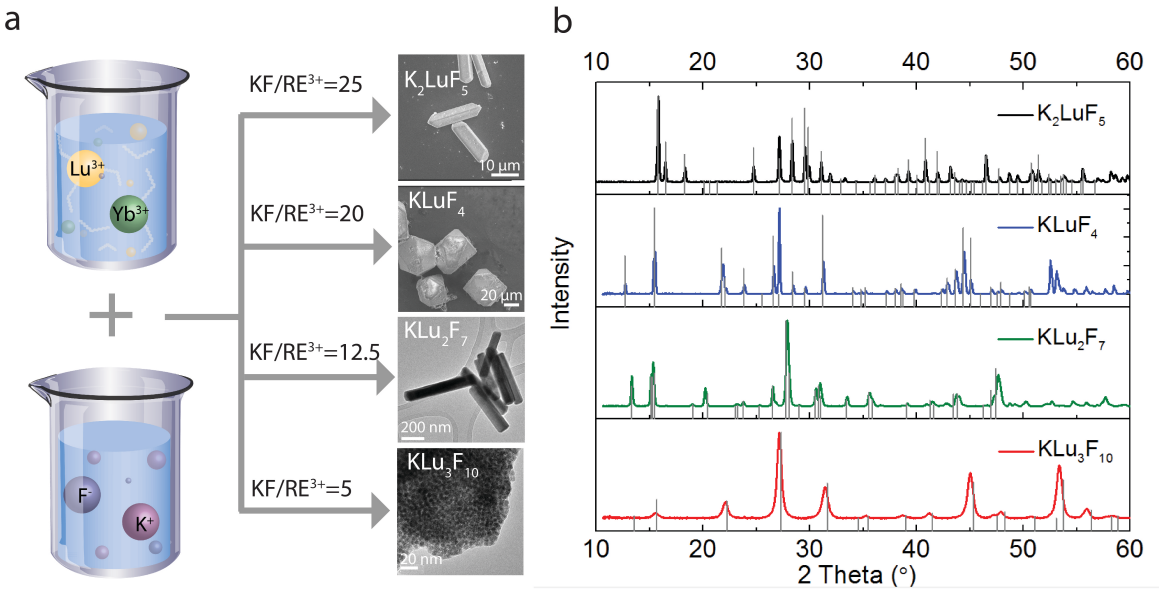

Figure 4.1: (a) Microscopic images of KLF crystals synthesized with various molar ratios of KF to RE^{3+}. (b) XRD patterns of KLF samples synthesized with KF/RE = 25, 20, 12.5, 5 (from top to bottom). The standard data of K_2LuF_5 (PDF Card 04-005-6013), $KLuF_4$ (PDF 04-019-4298), KYb_2F_7 (PDF 00-027-0459, KLu_2F_7 is not available in the database), KLu_3F_{10} (PDF 04-002-4130) are given as references. Copyright ©2021 American Chemical Society.

In this work we report the rapid, low-cost hydrothermal synthesis of four $(KF)_x{\cdot}(REF_3)_y$ crystallographic phases (KLu_3F_{10}, KLu_2F_7, $KLuF_4$, and K_2LuF_5), including several that are challenging to grow with bulk growth methods. Each crystalline phase ex-

hibits distinct morphologies, with sizes ranging from nanometers to hundreds of micrometers. Fluorescence spectra and emission lifetimes of the four crystalline phases were characterized based on the point-group symmetry of trivalent cations in each crystal phase. Yb(III) lifetimes in $KLuF_4$, and K_2LuF_5 were measured to be above 2 ms, primarily due to a combination of their relatively weak oscillator strength[86] and radiation trapping. It is beneficial to use laser hosts with long fluorescence lifetimes for energy storage and Q-switching[86]. The laser-refrigeration performance of each phase was examined via (i) optomechanical eigenfrequencies of the crystals on cantilevers in vacuum and (ii) the Brownian dynamics of crystals optically-trapped in water. Micron-scale Yb:$KLuF_4$ shows the most significant cooling among all four crystalline phases investigated, with minimum temperatures observed by 8.57 ± 2.07 K below room temperature. This is the first experimental laser cooling demonstration of hydrothermal potassium lutetium fluoride materials in both aqueous media and vacuum, and this technology may be further developed in the future for use in micron-scale radiation balanced lasers.

4.2 Synthesis and characterization

4.2.1 Hydrothermal synthesis of potassium lutetium fluorides

Rapid, low-cost hydrothermal syntheses were used to grow the Yb-doped $(KF)_x{\cdot}(LuF_3)_y$ crystals. The synthesis was performed with the following minor modifications to Ref [89]. Lutetium nitrate ($Lu(NO_3)_4$) and ytterbium nitrate ($Yb(NO_3)_3$ were of 99.99% purity and purchased from Sigma-Aldrich. Potassium hydroxide (KOH), potassium fluoride (KF), ethanol, and oleic acid were analytical grade purchased from Sigma-Aldrich and used without further purification. 18.6MΩ Milli-Q deionized water was used for each synthesis. For a typical synthesis, 420.8 mg of KOH was dissolved in 1.5 mL of water, followed by 5 mL of ethanol and 5 mL of oleic acid with stirring.

Table 4.1: Crystallographic information of K_2LuF_5, $KLuF_4$, KLu_2F_7, and KLu_3F_{10}

Sample	Crystal System	Space Group	Yb^{3+} Site Symmetry	Lattice Parameter	Centro / non-centro
K_2LuF_5	Orthorhombic	Pnma	C_2	a = 10.699 Å, b = 6.534 Å, c = 7.145 Å	Centrosymmetric
$KLuF_4$	Trigonal	$P3_121$	C_1	a = b = 8.012 Å, c = 10.058 Å (α = β = 90°, γ = 120°)	Noncentrosymmetric
KLu_2F_7	Orthorhombic	$Pna2_1$	C_2, C_1	a = 11.716 Å, b = 13.241 Å, c = 7.739 Å	Noncentrosymmetric
KLu_3F_{10}	Cubic	$Fm\bar{3}m$	C_{4v}	a = b = c = 11.305 Å	Centrosymmetric

Then, 1.44 mL of 0.5M $Lu(NO_3)_3$ and 0.16 mL of 0.5M $Yb(NO_3)_3$ were added into the mixture. After stirring for 10 min, 3 mL of aqueous KF solution was added dropwise. The molar concentration of the KF solution depends on the target product. After additional agitation for 10 min, the resulting mixture was transferred to a 23 mL Teflon-lined autoclave and heated at 220°C for 24 hours. After the autoclave cooled to room temperature, crystals were isolated by washing and centrifuging by ethanol and water three times. The first time must be washed with ethanol to avoid microemulsion formation. After drying the product at 60°C for 12 hours, they were transferred to a Lindberg Blue tube furnace and heated at 300°C for 2 hours to remove the organic surface ligand.

Four phases, KLu_3F_{10}, KLu_2F_7, $KLuF_4$, and K_2LuF_5, were successfully synthesized by varying the concentration of the KF precursor. Figure 4.1 shows the morphologies and powder X-ray diffraction (XRD) patterns of these four phases synthesized with different KF/RE^{3+} ratios, ranging from 5 to 25. As shown, the as-synthesized samples exhibit distinct shapes and lattice structures. Progressively increasing the KF/RE^{3+} ratio changes the morphology of products in the following sequence: nanoparticles, nanorods, micropolyhedra, and finally, microrods. In general, a higher KF/RE^{3+} ratio exhibits a larger crystal size. The K_3LuF_6 phase was

not observed using hydrothermal synthesis, even with a KF/RE^{3+} ratio as high as 60. This is consistent with previous experiments showing that only four phases of $(KF)_x \cdot (YbF_3)_y$ crystals are observed in hydrothermal synthesis[89].

The diffraction pattern of the product prepared with $KF/RE \geq 25$ can be indexed to orthorhombic K_2LuF_5. The crystal structure of the orthorhombic phase is determined with lattice parameters of a = 10.699 Å, b = 6.534 Å, c = 7.145 Å, and a space group of Pnma. When the KF/RE molar ratio decreases to 20 the XRD peaks index to $KLuF_4$. The XRD analysis result gives an unusual trigonal symmetry of space group P3121 (a = b = 8.012 Å, c = 10.058 Å, $\alpha = \beta = 90°$, $\gamma = 120°$), which is non-centrosymmetric and enantiomorphic, although the handedness of the specific enantiomorph is remains a subject for future work. Upon a further decrease of the KF/RE molar ratio to 12.5, a new phase of orthorhombic KLu_2F_7 was synthesized. No XRD pattern is available in the PDF 2019 database, but the diffraction peaks are similar to those of orthorhombic KYb_2F_7, which is an appropriate comparison due to the similar ionic size of Yb^{3+} and Lu^{3+}. In Figure 4.1b), the XRD patterns are slightly shifted to higher angles with respect to the KYb_2F_7 reference because the Lu^{3+} ionic size (0.861 Å) is slightly smaller than that of Yb^{3+} (0.868 Å)[88], and thus has a smaller lattice size compared to the reference KYb_2F_7. The KLu_2F_7 phase has space group Pna21 with lattice parameters of a = 11.716 Å, b = 13.241 Å, c = 7.739 Å. When the KF/RE molar ratios decreases to 5, a cubic phase KLu_3F_{10} of space group $Fm\bar{3}m$ (a = b = c = 11.305 Å) is observed. More details of these four crystallographic phases are listed in Table 4.1. Among these phases, KLu_2F_7 and $KLuF_4$ are non-centrosymmetric, which also makes them candidate materials for non-linear optics.

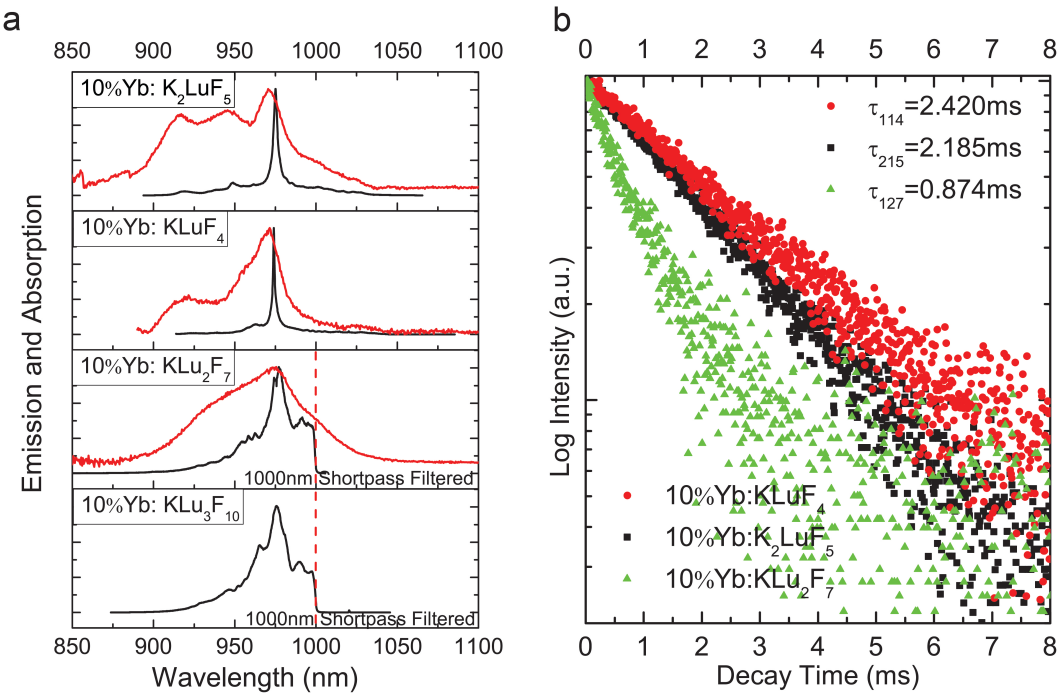

Figure 4.2: (a) Room temperature PL spectra of Yb(III) ions $^2F_{5/2}$ - $^2F_{7/2}$ electronic transition of 10%Yb:K_2LuF_5, 10%Yb:$KLuF_4$, 10%Yb:KLu_2F_7 and 10%Yb:KLu_3F_{10} under 1020nm laser excitation. (b) PL decay profiles of $^2F_{5/2}$ - $^2F_{7/2}$ transitions of 10%Yb:K_2LuF_5, 10%Yb:$KLuF_4$ and 10%Yb:KLu_2F_7. The fitted fluorescence lifetime is provided.

4.2.2 Optical characterization

Figure 4.2 shows the PL of 10%Yb:K_2LuF_5, 10%Yb:$KLuF_4$, 10%Yb:KLu_2F_7 and 10%Yb:KLu_3F_{10} upon 1020 nm laser excitation. The electronic energy configuration of Yb^{3+} in the KLF host matrix consists of a $^2F_{7/2}$ ground state and a $^2F_{5/2}$ excited state manifolds, both splitting into Stark levels due to the electrostatic crystal field of the host materials. If the Yb^{3+} point symmetry is lower than cubic (O, O_h, T_d), the $^2F_{5/2}$ and $^2F_{7/2}$ states would split into 3 and 4 Kramers doubly-degenerate Stark levels, otherwise it would be 2 and 3 crystal-field levels for each manifold[38]. Each double-degeneracy only lifts under an applied magnetic field. The full emission spectra of Yb^{3+} $^2F_{5/2}$ -$^2F_{7/2}$ transitions for 10%Yb:K_2LuF_5 and 10%Yb:$KLuF_4$ single crystals were recorded by using the time-gated spectroscopy. Although there are twelve allowed transitions for these two phases, only one dominant peak around 974 nm was observed. For the 10%Yb:$KLuF_4$ sample, the full width at half maximum (FWHM) of the primary peak is less than 2 nm without any further processing of the crystal. A side peak around 1030 nm is reported in structurally similar Yb:KYF4[11]. However, we did not observe such peaks in our detector range.

Besides the intense emission at 974 nm, 10%Yb:K_2LuF_5 and 10%Yb:$KLuF_4$ both have fluorescence lifetimes longer than 2 ms (Figure 4.2b). For 10%Yb:KLu_2F_7 and 10%Yb:KLu_3F_{10}, the measured Yb emission lifetimes are short compared to the other samples as 10%Yb:KLu_2F_7 has a fluorescence lifetime of 874 μs and for 10%Yb:KLu_3F_{10} the fluorescence lifetime was faster than the 100 microsecond resolution of our detector. Due to the relatively short fluorescence lifetime, the time-gated method for a full range emission spectrum did not work well, and a 1000 nm short-pass filter was applied to block the laser line. The spectra below 1000 nm were recorded for 10%Yb:KLu_2F_7 and 10%Yb:KLu_3F_{10}. According to Figure 4.2a, the PL from these two crystalline phases are much broader than the previous two phases.

The Stark multiplet structure of excited and ground states determines the respective relaxation channels resulting in Stokes and anti-Stokes energy transfer[90]. Such differences in spectral lines result from differences in the local symmetry and strength of the electrostatic crystal field[91].

The lifetime we measured is the inverse of the total decay rate $W = W_r + W_{nr}$, which has radiative (W_r) and nonradiative (W_{nr}) components. The radiative decay rate depends on the oscillation strength related to the local symmetry environment of Yb^{3+} while the nonradiative decay rate is affected by the lattice phonon energy, dopant concentration, and defects with high energy vibrational modes. According to the energy gap dependence law[12], the nonradiative rate increases rapidly with the high vibration energy of the lattice and/or defects. As W_{nr} is temperature dependent, the lifetime change of materials could be used for probing local temperature at nanometer scale[92]. In our study, the starting materials, synthesis method, and Yb-doping concentration of these KLF crystals are the same. Some potential reasons for the lifetime difference can be ruled out, such as impurities and defects inside the crystal, energy transfer pathways that depend on dopant concentration, and lattice phonon energies. In general, the fluoride phonon energy is low. FTIR spectra with the highest vibrational mode of each crystalline phase are in Figure 4.3.

The long emission lifetimes of 10%Yb:K_2LuF_5 and 10%Yb:$KLuF_4$ are attributed to the low nonradiative decay rate and also potential radiation trapping in large-size crystals[93]. Radiative and nonradiative relaxation mechanisms can be modified by the local symmetry structure of the host lattice and crystal size, respectively[94]. Here the radiative decay rate cannot be estimated without more detailed spectroscopic data. Surface defects are one of the main causes of nonradiative decay for these fluoride crystals. A large crystal volume significantly lowers the surface-to-volume ratio and thus decreases nonradiative rates[95]. Yb^{3+} ions exhibit significant

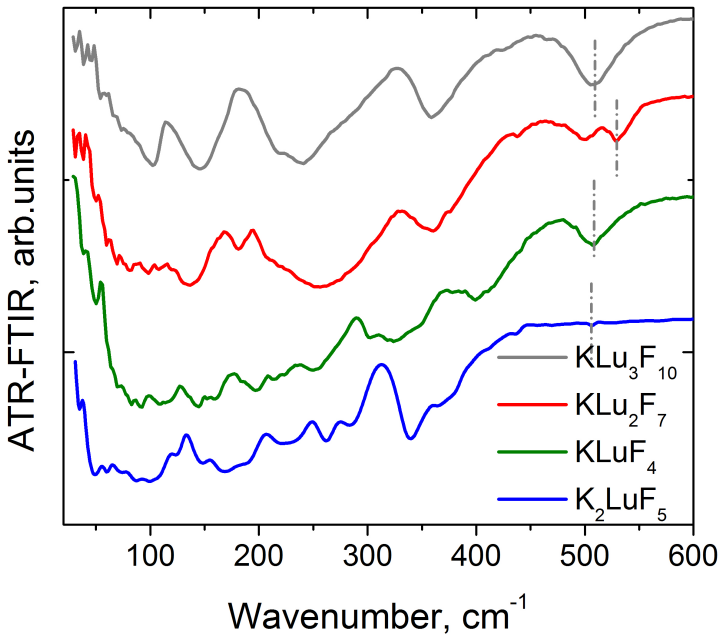

Figure 4.3: ATR-FTIR spectra for all four KLF crystollographic phases.

overlap between absorption and emission spectra. Therefore the reabsorption of emission is non-negligible in crystals with characteristic dimensions on the order of 100 micrometers. This can result in a measured fluorescence lifetime as much as 30% higher than the expected value[96]. In this approximation, the corrected lifetimes of 10%Yb:K_2LuF_5 and 10%Yb:$KLuF_4$ are 1.68 ms and 1.86 ms, respectively. The sharp and intense emission at 974 nm for these two samples is possibly the result of reabsorption. Such fluorescence reabsorption is an important factor for laser media, as it can be used as an additional pumping source, recycling energy that would otherwise be lost as the fluorescence. This can therefore have a substantial influence on laser efficiency[93]. This reabsorption is even more important for laser refrigeration applications when total internal reflection has to be used for pumping in order to enhance the low *f-f* absorption. If laser cooling can be achieved in these crystals, they could be promising candidates for radiation-balanced microlasers.

4.3 Temperature measurement

4.3.1 Opto-mechanical eigenfrequency measurement in vacuum

The as-synthesized crystals were transferred onto a cadmium sulfide nanoribbon cantilever (CdSNR) with low NIR absorption to measure the temperature via the cantilevers optomechanical eigenfrequency[97]. As the temperature decreases, Youngs modulus of the CdSNR increases, and thus the eigenfrequency increases as well. The experimental setup and an optical micrograph of a 10%Yb:$KLuF_4$ crystal on the CdSNR in a vacuum cryostat is shown in Figure 4.4a and Figure 4.4b. Details for device fabrication are discussed further in the experimental section below. Figure 4.4c shows a representative eigenfrequency spectrum fit numerically with a Lorentzian. The eigenfrequency at various temperatures was calibrated and linearly fit (Figure 4.4d) with a slope of 1.98 ± 0.17 Hz/K for calibration of subsequent laser cooling

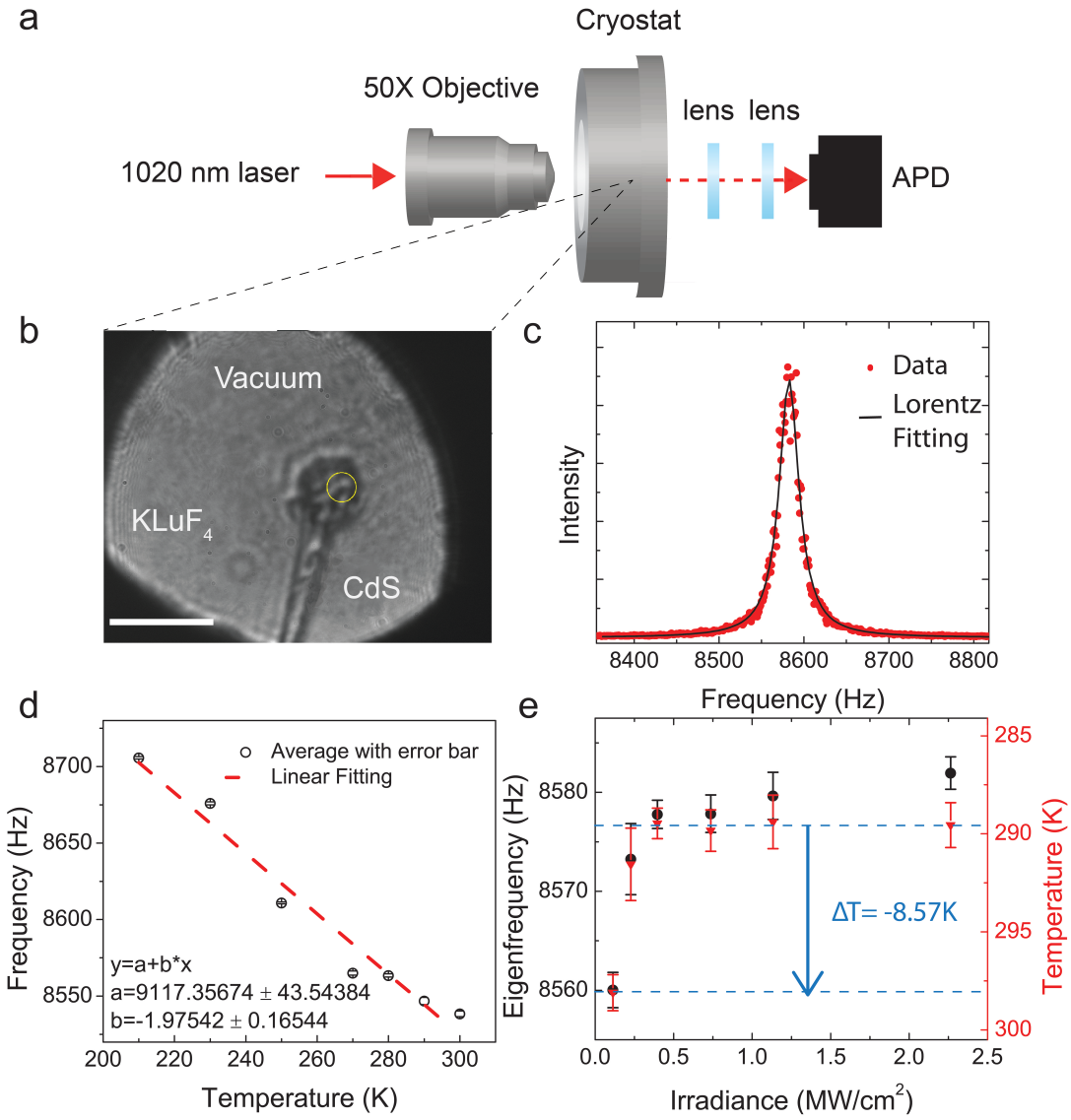

Figure 4.4: (a) Schematic of the experimental setup for the eigenfrequency measurement. (b) A microscopic image of a CdSNR with a 10%:$KLuF_4$ crystal. scale bar: 10 μm. (c) A representative Lorentzian fitting curve (black) of the eigenfrequency peak in the Fourier transferred signal plot (red). (d) Frequency vs. temperature calibration of the CdSNR + crystal cantilever. Black circle: average frequency of six measurements. The error bar stands for one standard deviation. Red: linear least-squares fit. The eigenfrequency decreases when increasing the temperature. (e) The frequencies measured (black) at various irradiances and the frequencies with trapping force caused frequency increase subtracted (red). The trapping effect subtracted frequencies are used to fit the temperature.

experiments. When excited by 1020 nm laser, the eigenfrequency was observed to increase with increasing laser irradiance, indicating net cooling of the cantilever. The eigenfrequency blue-shifts for 21.92 ± 3.42 Hz at the maximum irradiance (Figure 4.4e).

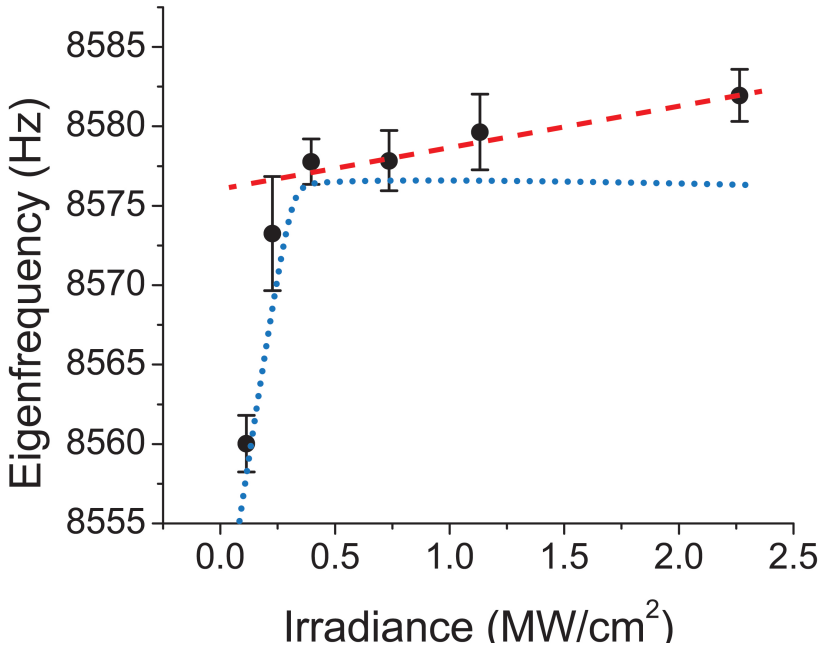

Figure 4.5: Schematic of laser trapping force subtraction. Red dashed line is the fitted eigenfrequency increase due to trapping effect. Blue dotted line is the eigenfrequency curve with trapping effect subtracted.

The cantilevers eigenfrequency depends not only on its temperature-dependent Youngs modulus but also on potential laser trapping forces, where the laser trap can be modeled as a Hookean spring located at the end of the cantilever. With the increased laser irradiance, the spring constant increases, and thus the cantilever eigenfrequency increases. After subtracting the increase in eigenfrequency related to

optical trapping, the blue shift due to the temperature change is 16.93 ± 4.09 Hz (see Figure 4.5). According to the temperature calibration, this indicates a temperature decrease of 8.57 ± 2.07 K (Figure 4.4e) for 10%Yb:$KLuF_4$. Laser cooling is not observed in other crystal phases. The CdSNsR with other crystals either have a decreasing eigenfrequency, suggesting heating, or burnt upon laser irradiance (see Figure 4.6.

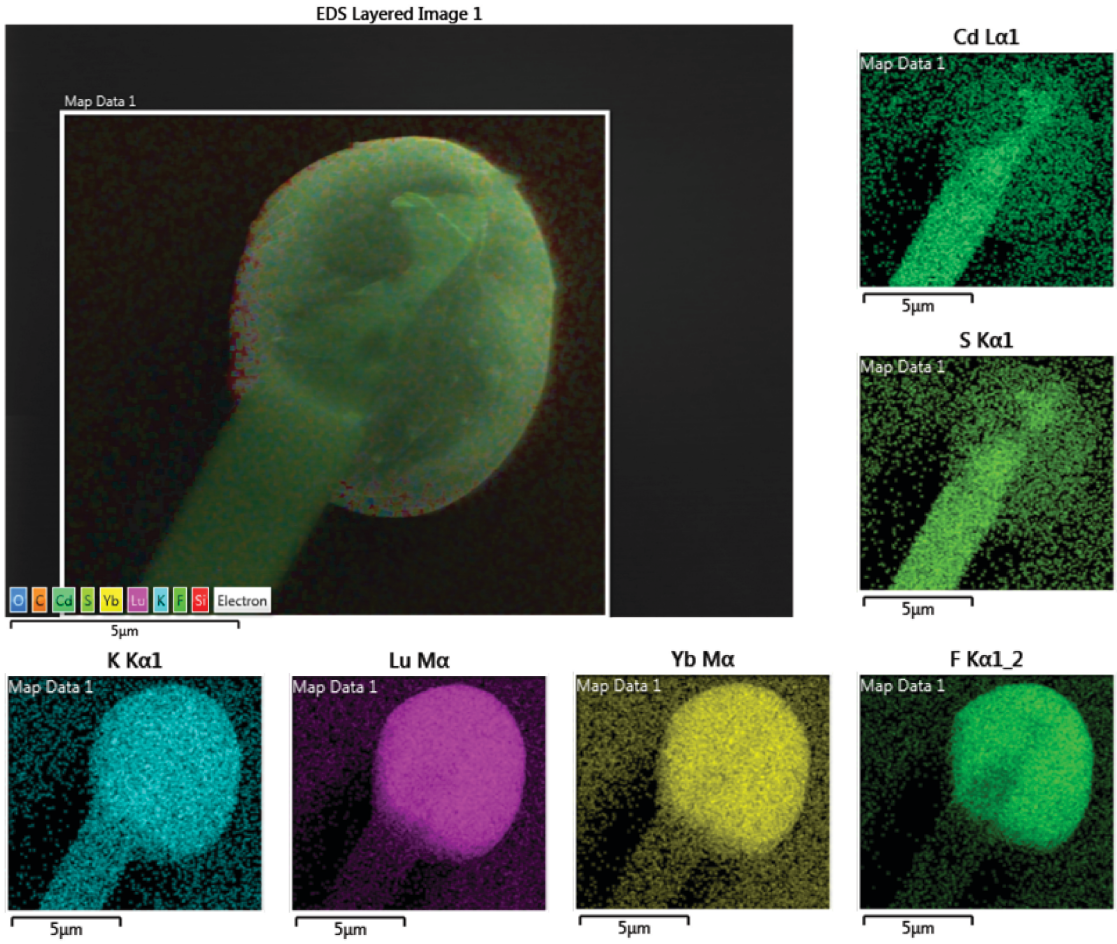

Figure 4.6: SEM image and EDS analysis of a burnt cantilever. Element maps of K, Lu, Yb, F, Cd, and S are provided. The CdS burnt with KLF nanocrystals and formed a new compound with Cd and S evenly distributed in it.

4.3.2 Cold-brownian-motion analysis of particles trapped in water

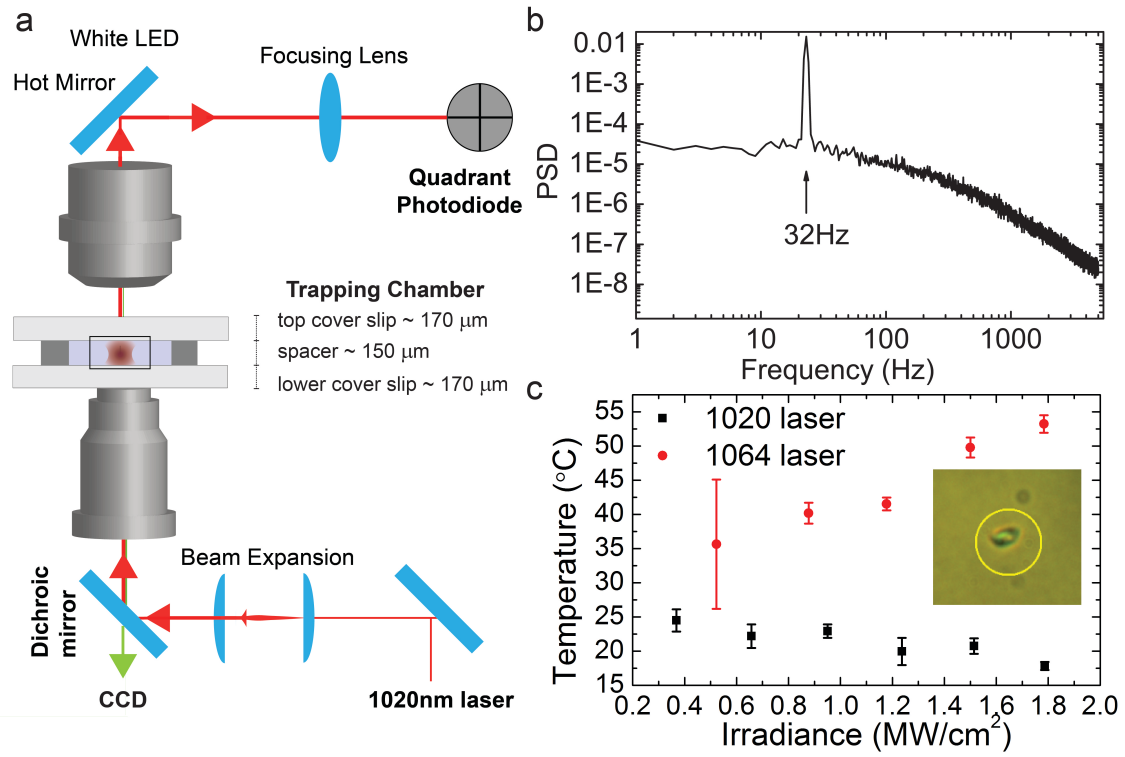

Figure 4.7: (a) Schematic of laser trapping setup. (b) A representative power spectrum of a trapped particle undergoes the Brownian motion in water with 32 Hz oscillation. (c) The temperature of 10%Yb:$KLuF_4$ ground crystal trapped by 1020 nm laser and 1064 nm laser in water.Copyright ©2021 American Chemical Society.

In addition to laser cooling in vacuum, the laser cooling performance of 10%Yb:$KLuF_4$ was observed in water as well. A home-built laser trapping instrument illustrated in Figure 4a was used to measure the temperature of an individual 10%Yb:$KLuF_4$ microcrystal through the analysis of the particles cold Brownian motion at a trapping wavelength of $\lambda = 1020$ nm. In order to minimize the heating of the trapping chamber, the microcrystals were trapped at a distance of 40 μm away from the quartz substrate, approximately in the middle of the fluid chamber. The dynamics of a

trapped particle were observed by recording the forward-scattered laser light via a quadrant photodiode (QPD). The power spectral density (PSD) vs. frequency was obtained by performing the Fourier transform as plotted in Figure 4.7b. The temperature was extracted from the PSD by the method in Refs[17, 98]. In brief, a 32 Hz oscillation of the trapping chamber was driven by the piezo-stage to convert the photovoltage signal in units of volts to units of length [m]. The local temperature of the trapped 10%Yb:$KLuF_4$ and surrounding water decreased 7.2 ± 0.6 K below room temperature, as shown in Figure 4c. As a control, we also measured the temperature of 10%Yb:$KLuF_4$ trapped in water with 1064 nm laser, which is not resonant with Yb^{3+} but can heat the surrounding water. With the same temperature extraction method, the sample temperature increased above 50°C. Optical trapping experiments with the 10%Yb:K_2LuF_5 phase observed reduced heating in water as shown in Figure 4.8.

4.4 KLF growth mechanism

Control over both crystallographic phases and their corresponding morphologies requires a deep understanding of crystal growth. Some preliminary investigations on the KLF growth were performed. We do not have a solid conclusion on the growth mechanisms yet, but this will be part of the future works.

4.4.1 Thermodynamic stability of four crystallographic phases

Time series syntheses of KLF with different starting KF/RE ratios were performed. A common synthetic method described in the hydrothermal synthesis section was used. The heating temperature was 220°C and the heating time ranges from 0 h to 24 h. After washing with water and ethanol, the powder XRD was performed with the collected samples to identify the crystallographic phase. Figure 4.9 summarizes

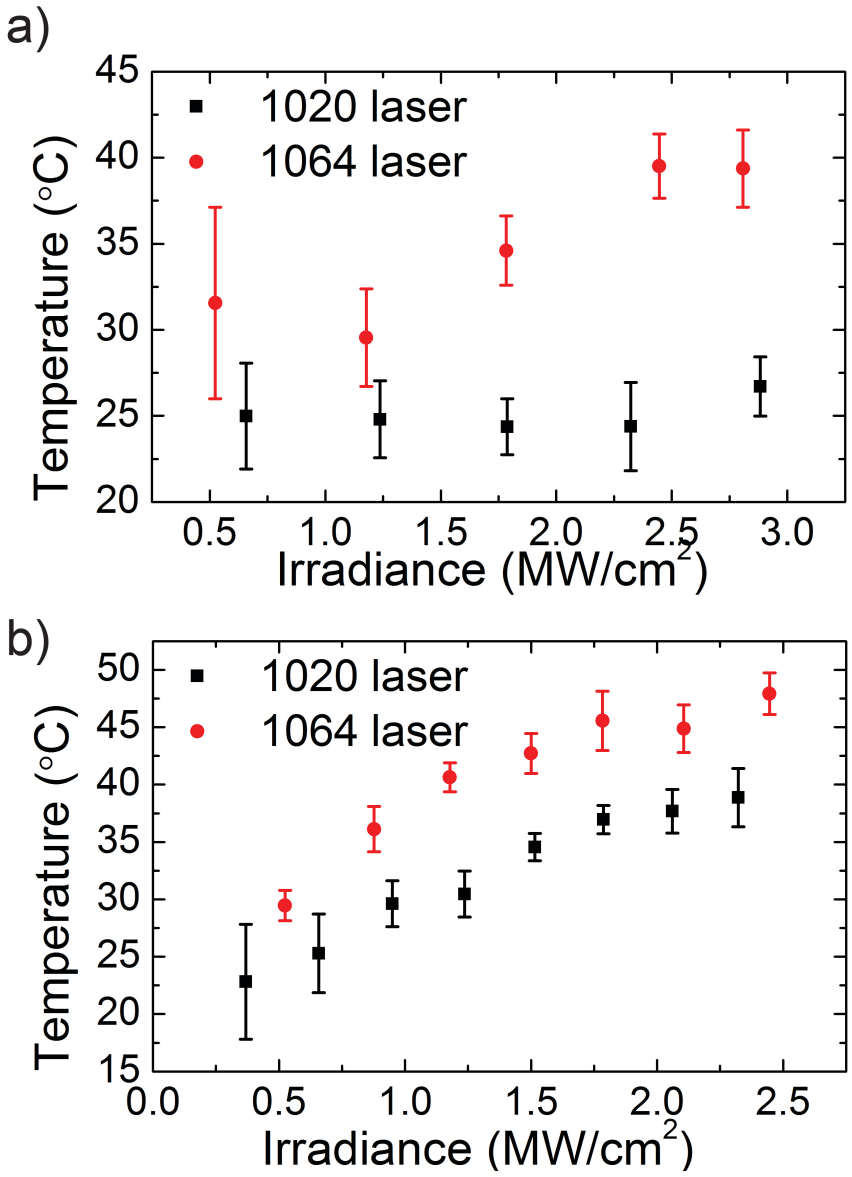

Figure 4.8: (a) The temperature of 10%Yb:K_2LuF_5 ground crystal and (b) a SiO_2 bead trapped by 1020 nm laser and 1064 nm laser in water.

the KLF crystals obtained with increasing heating time and increasing KF/RE ratio. Detailed XRD data can be found in the following figures.

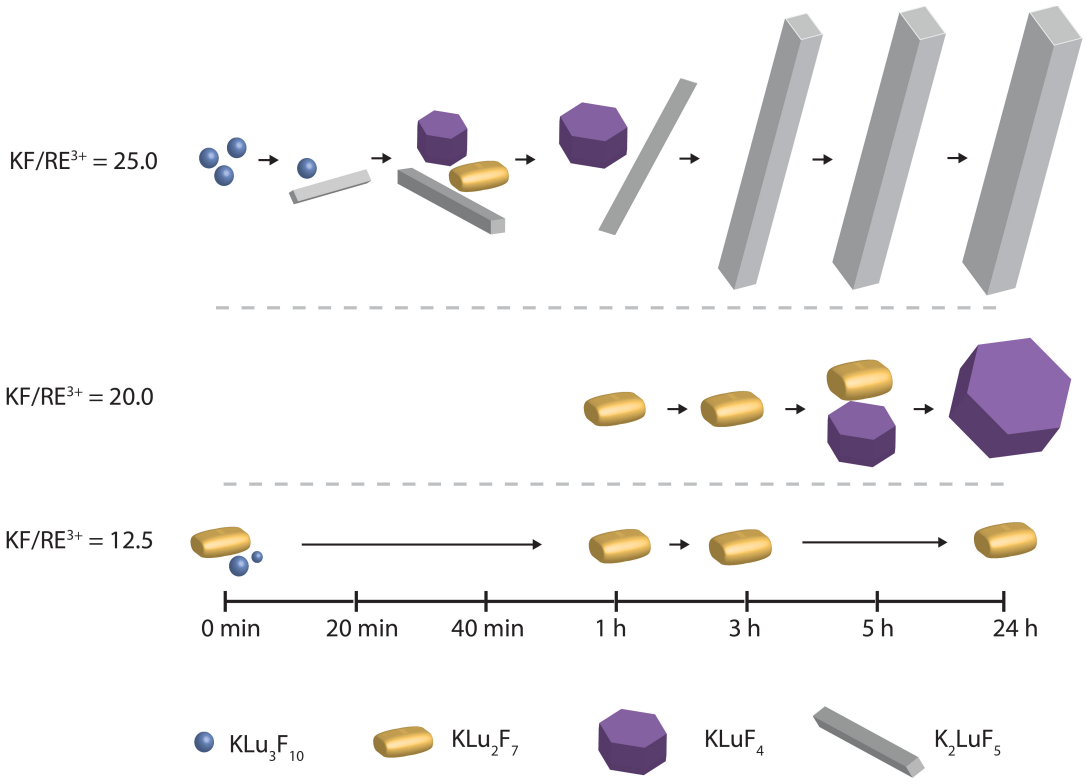

Figure 4.9: Potassium lutetium fluoride products of various KF/RE^{3+} ratios with increasing heating time in the autoclaves.

For the starting KF/RE ratio of 25, the cubic phase KLu_3F_{10}, the orthorhombic K_2LuF_5, the orthorhombic KLu_2F_7, and the trigonal $KLuF_4$ appeared in sequence in the first hour (Figure 4.10). After 3 hours heating, the pure K_2LuF_5 crystals formed and the other three crystallographic phases disappeared by the order of KLu_3F_{10}, KLu_2F_7, and $KLuF_4$. According to the COMSOL simulation (Figure 4.11), it takes 50 mins to reach the steady temperature inside the liner. The products at each temperature are represented on the temperature curve in Figure 4.11.

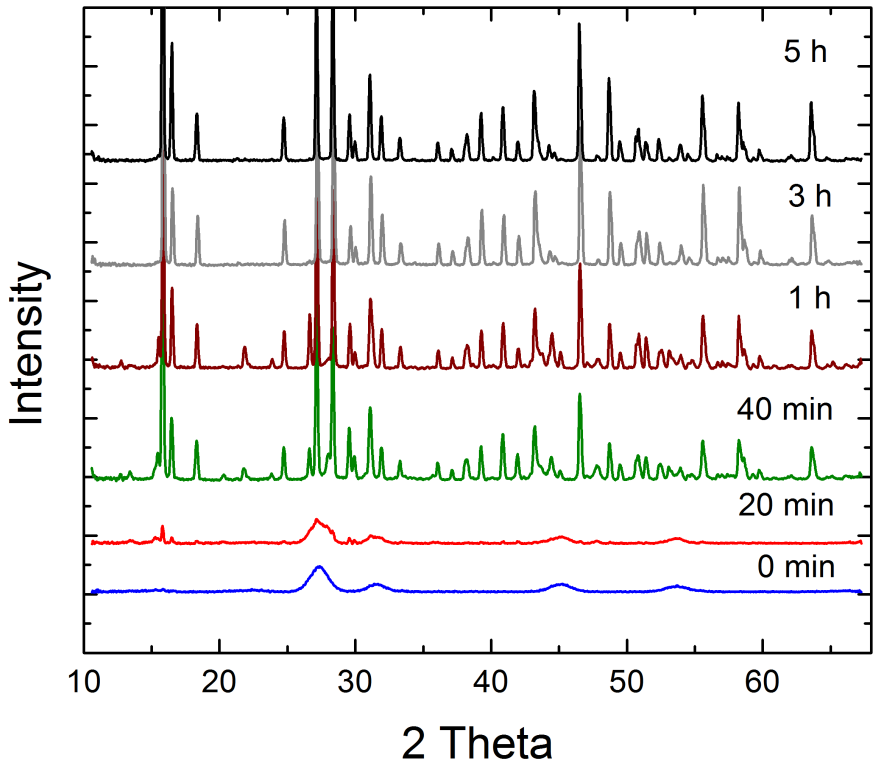

Figure 4.10: XRD of K_2LuF_5 synthesis with KF/RE =25 at 0 min, 20 min,40 min, 1 h, 3 h, and 5h. Without any heating, the product is the pure KLu_3F_{10}. After heating for 20 min, K_2LuF_5 peaks start to appear, which suggests the nucleating and growing of the target phase. After 40 min heating, the KLu_3F_{10} phase is gone and two new phases $KLuF_4$ and KLu_2F_7 appear and coexist with the K_2LuF_5. After 1-hour heating, the KLu_2F_7 disappears. After 3-hour heating, the pure K_2LuF_5 is obtained and the size keeping growing.

According to Figure, the thermodynamic stability of these crystals can be inferred by their "disappearing" temperature. The thermodynamic stability is K_2LuF_5 > $KLuF_4$ > KLu_2F_7 > KLu_3F_{10}.

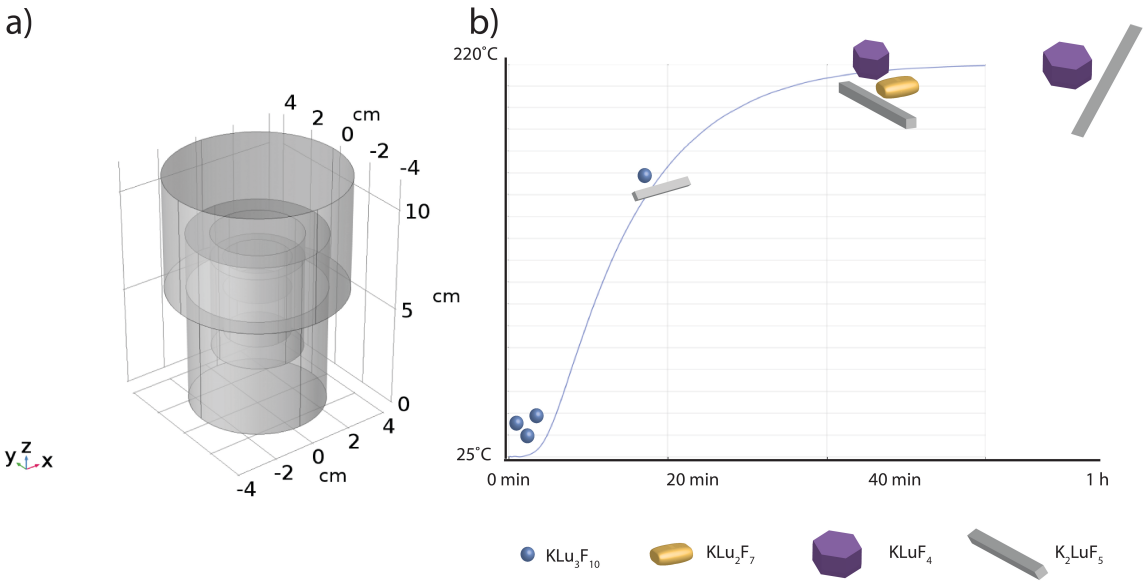

Figure 4.11: (a) The heat transfer model of a Teflon-lined autoclave. (b) Simulated temperatures of the mixture in the Teflon liner. The corresponding products at different heating times are labelled.

When the KF/RE starting ratio is 20, with which the final product is $KLuF_4$, the temporary products after 1h and 3 h heating are both KLu_2F_7. The $KLuF_4$ peaks starts to show after 5 h heating (Figure 4.12). However, the solvent mixture temperature inside the reactor has already reached 220°C for at least 2 hours before the formation of $KLuF_4$. The Scherrer analysis shows an increase in the KLu_2F_7 size from 297.4 ± 19.4 nm at 1 h to 334.6 ± 35.3 nm at 3 h, and to 360.9 ± 35.6 nm at five h, which suggests some KLu_2F_7 crystals are still growing when $KLuF_4$ starts to form.

When the KF/RE ratio is 12.5, the product is always KLu_2F_7 except some KLu_3F_{10}

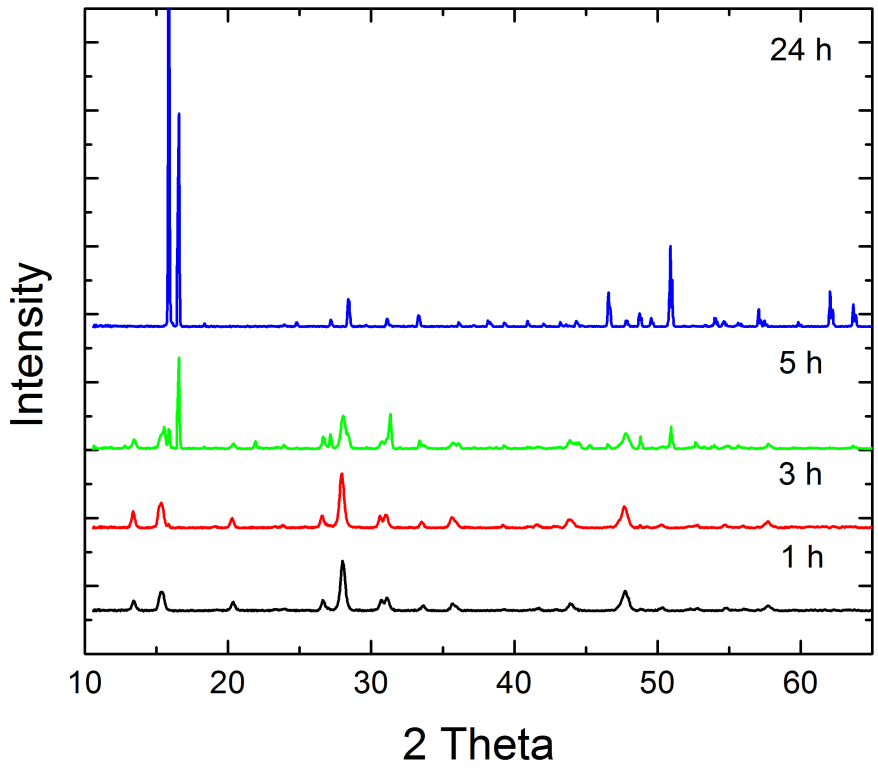

Figure 4.12: XRD of $KLuF_4$ synthesis with KF/RE =20 at 1 h, 3 h, 5h, and 24 h. For the first 3 hour, only KLu_2F_7 is observed. The 5-hour result show the first existences of the target phase $KLuF_4$, and then they grow into big microcrystals.

nanoparticles form before heating (Figure 4.13).

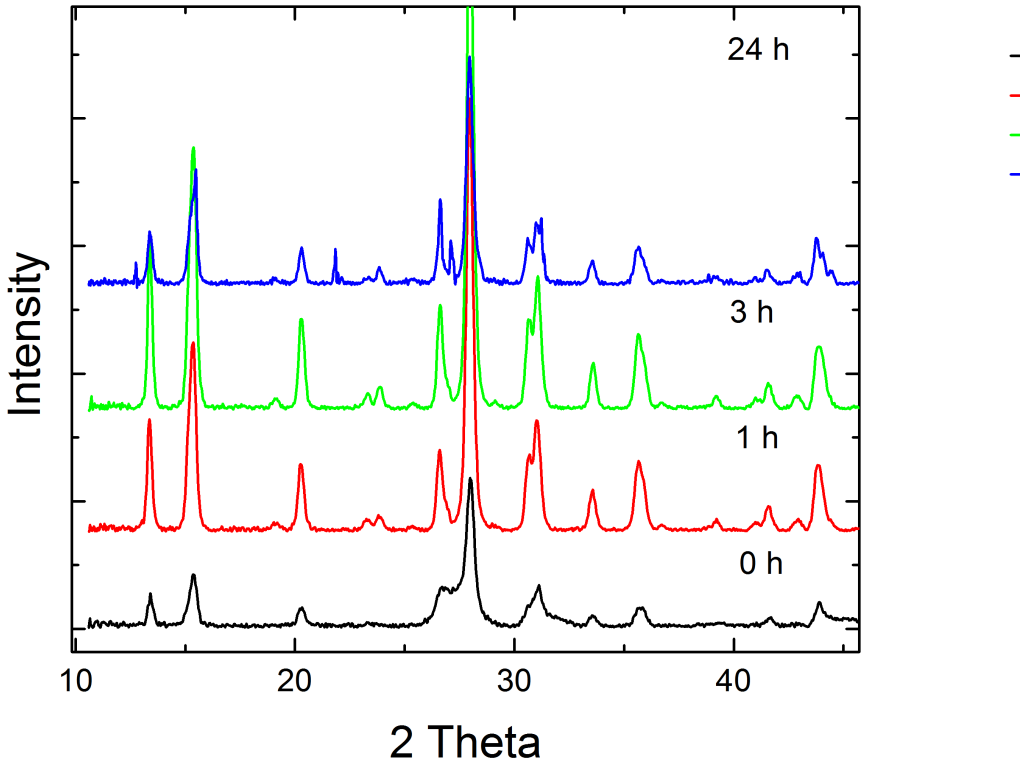

Figure 4.13: XRD of KLu_2F_7 synthesis with KF/RE =12.5 at 0 h, 1 h, 3 h, and 24h. Small amount of KLu_3F_{10} nanoparticles form before heating. Then they turn to KLu_2F_7. However, peaks of $KLuF_4$ appear after 24-hour heating.

4.4.2 K_2LuF_5 growth velocity

Control over both crystallographic phases and their corresponding morphologies requires a deep understanding of crystal growth. Among the various KLF crystal systems, K_2LuF_5 is a good candidate to study crystallization kinetics in nanometer- and

micron size-scales because of its rod-like morphology and high growth speed. The size and morphology of K_2LuF_5:10%Yb synthesized under 1 h, 3 h, and 5 h heating are in Figure 4.14. The growth velocity of K_2LuF_5 is at least 0.77 μm/min along the growth direction and 0.10 μm/min perpendicular to the growth direction in the first hour.

We also observed that the doping concentration of Yb^{3+} ions has an effect of controlling the length of K_2LuF_5 rods, with the length of the rods increasing with higher concentrations of Yb^{3+}. While the crystal length is obviously affected, the crystal width does not change significantly. Statistics for K_2LuF_5 crystal length and width are illustrated in Figure 4.15 with different Yb^{3+} doping levels. Morphology differences such as the aspect ratio for various lanthanide hydroxides have been reported[99]. It has been proposed that the surface energy of the particle changes the growth rate and, therefore, the aspect ratio. However, when there is 100% Yb in the crystal, i.e., K_2YbF_5, the crystal length is only around 20 um, much shorter than expected. A detailed study of the factors that affect crystal length remains a subject for future work.

4.5 Conclusions

Potassium lutetium fluoride is a less-explored member of the alkali-RE-fluoride family as it forms several different crystalline structures with various KF/LuF_3 binary compound ratios. In this article we present the low-cost, rapid hydrothermal synthesis of four distinct phases of potassium lutetium fluoride with the general stoichiometric formula $(KF)_x{\cdot}(LuF_3)_y$ including $KLuF_4$ (trigonal), KLu_2F_7 (orthorhombic), KLu_3F_{10} (cubic), and K_2LuF_5 (orthorhombic). Each phase was substitutionally doped with 10% ytterbium ions, and two of these phases ($KLuF_4$ and K_2LuF_5) were observed to be viable candidates for solid-state laser refrigeration. Laser refrigeration was demon-

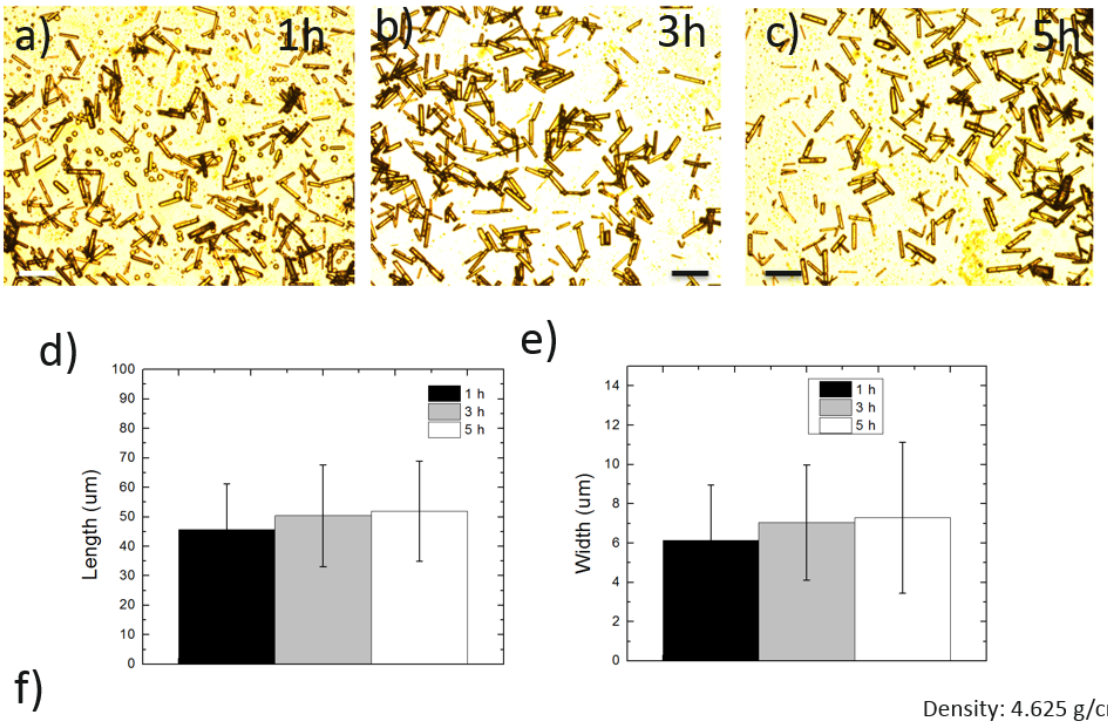

Density: 4.625 g/cm³

hour	length (um)	width (um)	unit volume (um³)	unit mass (mg)	total mass (mg)	total crystal amount
1	45.66354	6.13293	1717.534	7.94875E-06	98.5	1.24E+07
3	50.4029	7.04672	2502.818	1.1583E-05	163.4	1.41E+07
5	51.98448	7.29185	2764.072	1.27921E-05	201.4	1.57E+07

Figure 4.14: Optical microscopic images of K_2LuF_5 synthesized for (a) 1 hour, (b) 3 hours, and (c) 5 hours. Scale bar = 100 um. (d) The average length and (e) width statistics of K_2LuF_5 synthesized for 1 hour, 3 hours, and 5 hours. (f) A summary table of crystal size, mass, and number.

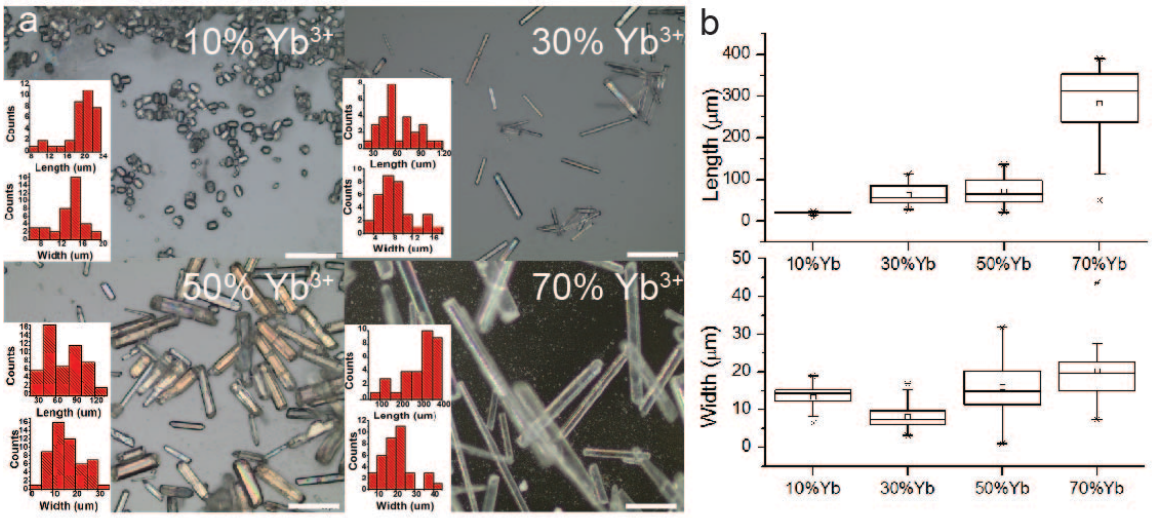

Figure 4.15: (a) Optical microscopic images of $10\%Yb^{3+}$/ $0.5\%Er^{3+}$: K_2LuF_5, $30\%Yb^{3+}$/ $0.5\%Er^{3+}$: K_2LuF_5, $50\%Yb^{3+}/0.5\%Er^{3+}$: K_2LuF_5, $10\%Yb^{3+}/0.5\%Er^{3+}$: K_2LuF_5. In-set: length and width distributions. (b) Length and width statistical plot of K_2LuF_5 samples doped with 10% - 70% Yb and 0.5% Er.

strated using both the optomechanical cantilevers in vacuum and also through observing the Brownian dynamics of the crystals optically trapped in water. Yb:$KLuF_4$ shows the most significant cooling with minimum temperatures observed to be 8.57 $\pm$ 2.07 K below room temperature. Fluorescence spectra and emission lifetimes of the four crystalline phases were characterized based on the point-group symmetry of trivalent cations in each crystal phase. This is the first experimental laser cooling demonstration of potassium lutetium fluoride materials in both aqueous media and vacuum. Furthermore, each crystalline phase exhibits distinct morphologies, which may be advantageous in the future development of micron-scale radiation-balanced lasers. There are some preliminary findings on crystal growth, which need more work in the future to explore the growth mechanisms.

Chapter 5

X-RAY INDUCED POINT DEFECTS IN YB:YLF MICROCRYSTALS AND THEIR IMPACT TO OPTICAL REFRIGERATION

5.1 Introduction

Solid-state laser refrigeration offers a promising, non-contact approach to optically control the operational temperature of materials in extreme environments, including nuclear and space applications with no moving parts or mechanical vibrations. However, extreme environments also expose laser cooling materials to ionizing radiation damage that can alter macroscopic properties, including corrosion resistance[100], refractive index[101], optical absorption and emission, etc. Experimental and theoretical studies have been conducted to identify the microscopic origins of these changes, such as element segregation[100] and changes in lattice structure[102]. The generation of point defects through ionization or atomic displacement is one of the main mechanisms that change the performance of materials in extreme conditions. Point defects introduce notable changes in materials' electronic energy level structure, causing their own energy levels and bands to appear. In the case of laser cooling fluoride materials, point defects such as fluoride color centers are potential sources of background absorption and changes of other optical properties in radiation-balanced lasers that can lower the cooling efficiency or even cause heating. Production of radiation-induced defects have been reported with x-ray[103], gamma ray[104, 105, 106, 107], electron beam[108, 106, 107], and femtosecond pulsed laser radiation[108]. Besides producing and identifying radiation-induced defects, estimating the influence of ionizing radia-

tions on the spectroscopic properties of rare earth elements is also necessary, especially in luminescent optical refrigeration applications.

Changes in optical properties of YLF following exposure to ionizing radiation can alter the cooling performance of Yb:YLF. During irradiation, structural defects such as vacancies or interstitials can be created and cause definite changes to the crystal's optical properties. In this work, only point defects induced by ionizing irradiation will be considered. The most common center generated under such irradiation is the v_k (F_2^-) center (localized holes). Although there are four possible kinds of v_k centers in the YLF, none of these possible v_k centers are thermally stable. The most stable v_k center relaxes after 60 min at 77 K[109]. Another common defect in inorganic halide crystals is the F-type center, a halide ion vacancy with a trapped electron. F-centers can also aggregate and interact with each other. These defects have absorption bands in ultraviolet, visible, and near-infrared ranges.

In this work, Yb:YLF microcrystals were irradiated with x-rays to induce color centers in solid-state laser cooling materials. Meanwhile, laser cooling properties were compared to study the impacts of x-ray radiation on optical refrigeration optics. F-centers stable at room temperature were induced after x-ray irradiation. There are at least eight different types of point defects induced, with different thermal stabilities. Such point defects were confirmed with electron paramagnetic resonance spectroscopy and thermoluminescence spectroscopy. Non-contact thermometry was used to evaluate the cooling performance before and after the x-ray irradiation. Yb(III) photoluminescence was measured, and the mean emission wavelength was analyzed to extract the local temperature. The cooling performance of the YLF microcrystals deteriorated dramatically after irradiation, with most of the measured microcrystals unable to demonstrate measurable cooling after exposure to x-rays. Both increased background absorption and higher nonradiative relaxation rates are possible reasons

for the changes in the cooling properties. The absorption spectrum and Yb(III) excited state lifetime were measured to investigate the failure of optical refrigeration in x-ray irradiated Yb:YLF microcrystals.

Although x-ray induced point defects deteriorate the cooling performance of Yb:YLF, anti-Stokes emission of point defects observed in other materials brings the possibility of laser cooling[110]. The mechanism of such materials relies on the anti-Stokes emission of F-centers instead of lanthanides doping. The existence of different kinds of luminescent centers and the possibility of varying their relative concentration by changing the irradiation, annealing, and bleaching conditions make these crystals attractive from the point of view of finding a medium for laser cooling. The strong electron-phonon interaction in these centers results in broad emission bands.

5.2 X-ray irradiation of YLF microcrystals

Yb:YLF microcrystal powders were sealed in a Kapton film envelope. The thickness of the loose powder inside the envelope is roughly around 100 - 300 um. Room temperature irradiation of the envelope with Yb:YLF samples was accomplished using an x-ray tube (35kV@300uA, Moxtek Magpro). The distance between the sample and the x-ray tube is 3 cm. The sample was irradiated using the above parameters for 26 hours.

5.3 Characterizations of X-Ray induced point defects

5.3.1 Absorption

Optical absorption induced by X-ray radiation has been reported in doped and pure YLF[111]. A four-band pattern was found within 200-550 nm and no induced absorption was observed above 700 nm.[111] The position of the F-center absorption band is determined by the structure of the material, namely the symmetries and the distances

between the fluorine cite and surrounding cations. With the same symmetry, larger lattice constant induces the low energy shift of the bands. Sato *et al*[111] ascribe the peak around 340 nm to an F-center. The two bands around 280 nm and 420 nm are assigned to v_k centers. The induced absorption peak at 520 nm is ascribed to F_2 centers.

5.3.2 Thermoluminescence

Thermoluminescence (TL) measurements were performed on x-ray irradiated fluoride ceramic materials in order to compare the relative increase in color centers formed following x-ray irradiation. TL is a simple diagnostic for materials that relies on the emission of photons as point defects change their oxidation state, or heal following thermal annealing. Light is collected from small sample volumes as the temperature is ramped, and the total emitted optical intensity is plotted versus the instantaneous temperature (Figure 5.1). YLF powders adhered to the substrate disk with a thin layer of silicone vapor spray. YLF powders were heated in a nitrogen-protected chamber to collect TL using a photomultiplier. A yellow color glass filter (GG475, 475 nm long pass filter). The sample was heated at a rate of 1°C/s from room temperature to 500°C. The background has been subtracted. The following general order kinetics equations (GOK) were used to deconvolute the TL curves. [112, 113]

$$I(T) = I_m b^{\frac{b}{b-1}} e^u [1 + Z_m + (b-1)(1 - \frac{2kT}{E})(\frac{T^2}{T_m^2} e^u)]^{-\frac{b}{b-1}}, \tag{5.1}$$

where

$$u = \frac{E}{kT} \frac{T - T_m}{T_m}, \tag{5.2}$$

and

$$Z_m = 1 + (b-1)\frac{2kT_m}{E} \tag{5.3}$$

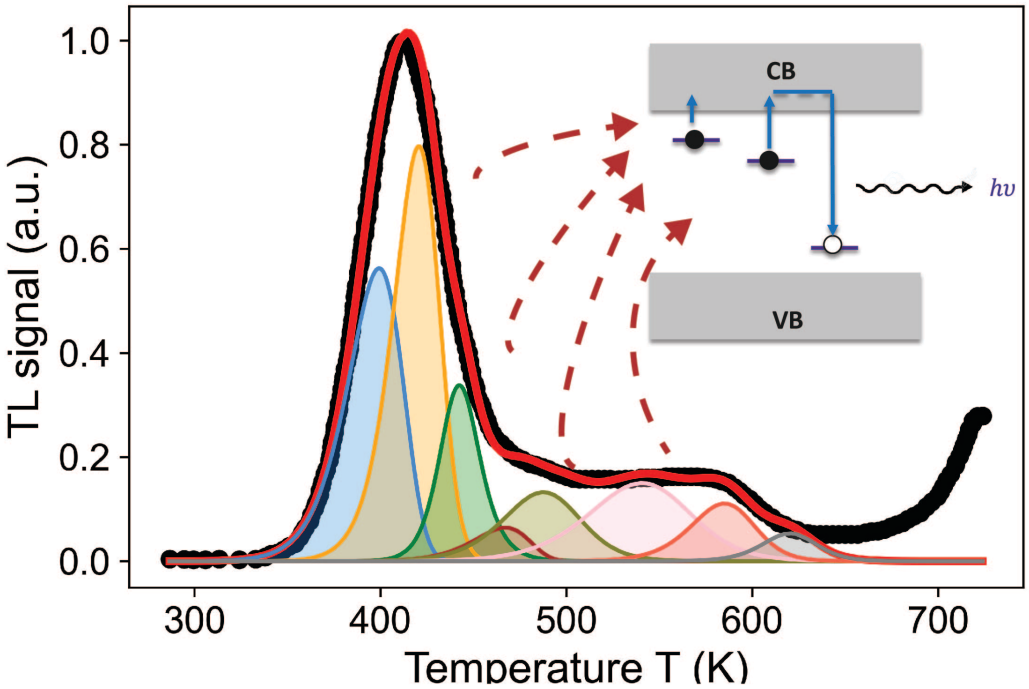

Figure 5.1: Thermoluminescence of x-ray irradiated Yb:YLF microcrystals and results of fitting. Eight glow peaks are fitted. Black dotted line: experimental data; red solid line: cumulative fit peaks.

In this expression, b is the kinetic order of the TL process, with a typical value between 1 and 2, I_m is the maximum intensity of the glow peak in counts per K, T_m is the temperature at peak maximum in K.

Table 5.1: **TL fitting parameters using the General Order Kinetics (GOK) model.**

Peak No.	I_m	b	E (eV)	T_m (K)
1	0.56	1.04	0.92	399.24
2	0.80	1.20	1.34	420.68
3	0.34	2.01	2.28	442.47
4	0.06	1.00	1.23	467.21
5	0.13	1.50	1.19	487.50
6	0.15	1.45	1.08	540.38
7	0.11	1.46	2.08	585.04
8	0.05	1.68	3.02	620.30

Eight peaks with peak maxima listed in Table 5.1 were observed with the x-ray irradiated sample. One of the irradiated samples was annealed at 473K prior the TL measurement to discharge the defects related to the first three main peaks and confirm the existence of other peaks at higher temperatures instead of artifacts from the intense main peak. The as-synthesized Yb:YLF was also tested. No TL emission was observed with Yb:YLF without irradiation. After irradiation, the TL curves show that at least eight trap centers are involved in the charge localization in YLF, which means eight different defects are formed, either before or during the x-ray irradiation.

Defects could appear at any stage of the materials life, during the crystal growth, or during its exploitation in extreme ionizing radiation. It is noted that several thermal activation temperatures are below the crystal growth temperature (220°C/493K), which implies such defects can not be formed during synthesis ("primary origin"). Instead, it is a result of the irradiation process ("secondary origin"). The defects related to higher activation temperature thermoluminescence peaks are more stable and may

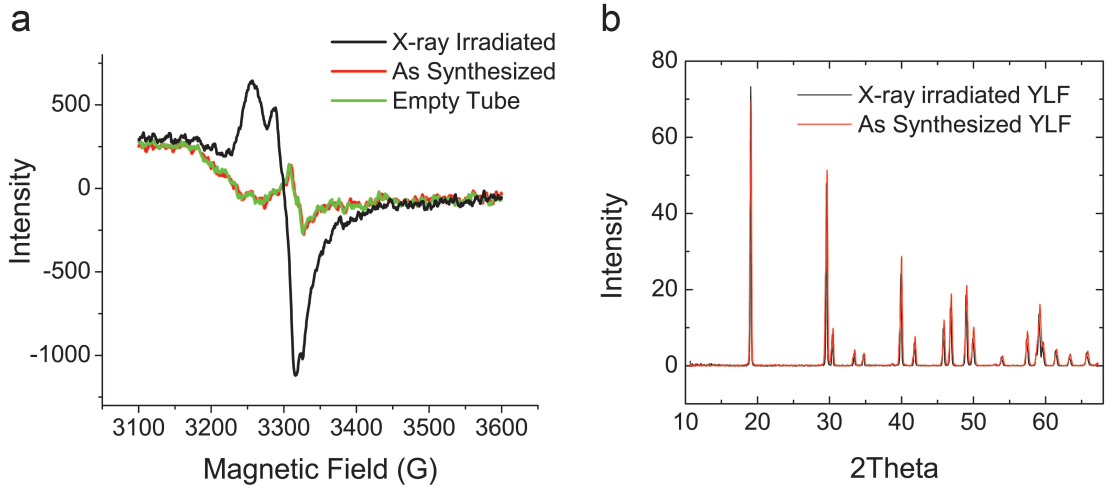

Figure 5.2: (a) EPR spectra of YLF microcrystals before (red) and after (black)X-ray irradiation and the background reference spectrum of an empty quartz tube. (b) X-ray diffraction of YLF powders before (red) and after (black) X-ray irradiation.

have both origins: primary, if formed during crystal growth, or secondary by later irradiation.

5.3.3 EPR

Electron paramagnetic resonance spectroscopy was used to detect the increased concentration of F-centers. The CW-EPR spectra were measured with a Bruker EMX spectrometer equipped with a Bruker SHQE resonator. The experimental sample was measured at room temperature with 1.0 mW microwave at 9.30138 GHz. The modulation frequency, amplitude, and sweep rate were were set to 100 kHz, 0.4 mT, and 0.358 mT s^{-1}, respectively.

Figure 5.2a shows EPR spectra of YLF crystals that have been irradiated with x-rays, a control YLF sample that was not irradiated with x-rays, as well as a spectrum of an empty quartz tube used for EPR measurements. According to the estimated

g values, which are close to $g = 2.0$, the EPR spectrum of the observed radiation defect is possibly caused by an electron trap center[109]. The F-center (a fluorine vacancy with a trapped electron) would be considered as the possible model for this defect. Clearly, high-energy x-ray irradiation increased the concentration of fluoride vacancies in the YLF crystal lattice.

More elaborate studies of this defect using optical spectroscopy and x-ray diffraction analysis, should be done in order to clarify the nature of the all radiation effects in these materials.

5.3.4 PL

Although absorption is an established method to characterize color centers in YLF. However, it is hard to obtain high quality absorption spectrum of micro-size samples with scattering suppressed or subtracted. Absorption of X-ray induced color centers can be measured with bulk YLF, which is part of the collaboration with with Dr. Markus P. Hehlen and Dr. Azzurra Volpi at University of New Mexico.

Some aggregate color centers also exhibit efficient fluorescence due to dipole-allowed electronic transitions. Both Stokes and anti-Stokes emission were observed with F-center aggregates in NaF[110]. The hydrotherapy synthesized YLF also has a broad emission band at 478 nm before X-ray irradiation, which means there are some color centers formed during the crystal growth. After irradiation, two new emission bands at 514 nm and 666 nm arise. The broad emission bands indicate strong electronphonon interactions in these centers. The two new emission peaks generated after X-ray irradiation are tentatively assigned to color aggregates. Without more reference data, it is hard to specify the color centers in YLF based on the emission. More detailed simulation of electronic transition may be helpful.

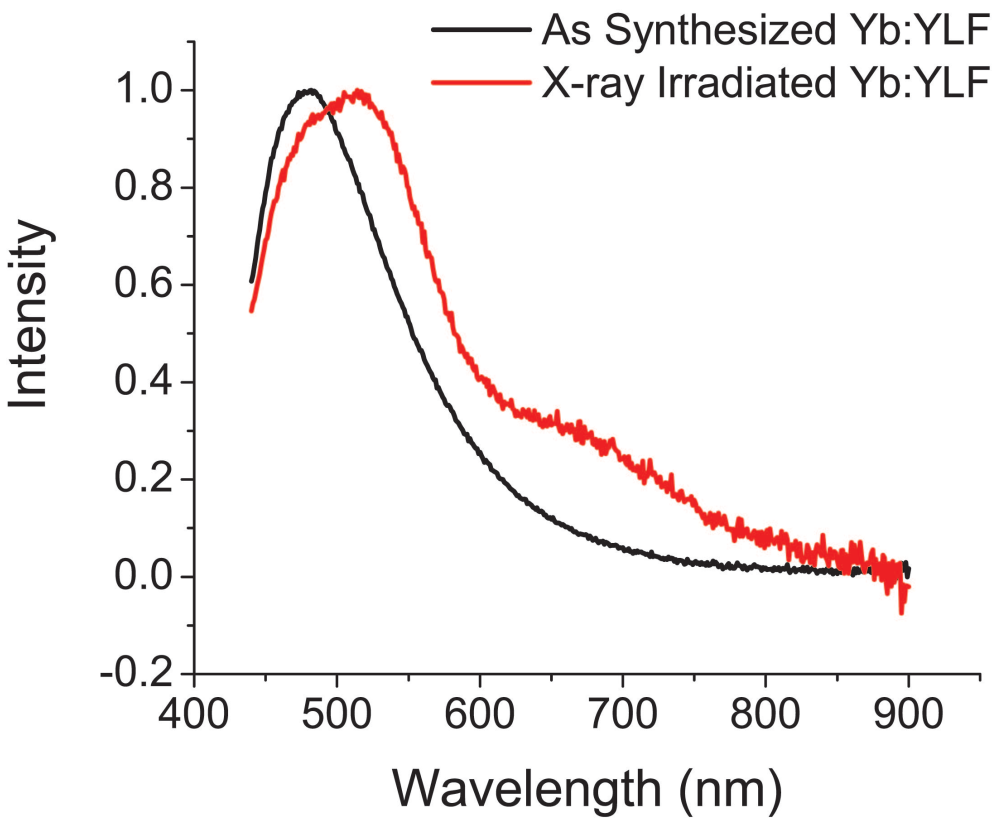

Figure 5.3: Normalized photoluminescence of ensemble as synthesized Yb:YLF without X-ray irradiation and X-ray irradiated Yb:YLF. The excitation wavelength is 420 nm. The YLF powers are bonded on a quartz coverslip with PMMA.

5.3.5 PLE

With the emission at 500 nm -700 nm, PLE spectra can be collected to study the absorption bands. PLE spectroscopy is a useful method to investigate the electronic level structure of materials with low absorption. It also helps suppress the scattering effect for small particles. Peaks in the PLE spectra represent absorption bands of the material. Figure 5.4 gives the PLE of as-synthesized Yb:YLF and X-ray irradiation Yb:YLF. A broad absorption band from 230 nm to 400 nm was observed, with a sharp PLE peak at 234 nm and a broad tail on the red side. Such features were observed in both irradiated and non-irradiated Yb:YLF. Again, there are defects forming during the synthesis. Figure 5.3 and Figure 5.4 show the absorption bands and corresponding emissions of those intrinsic defects of Yb:YLF without X-ray irradiation. After irradiation, the relative intensity of the peak at 245 nm is higher. This is probably the X-ray induced absorption band, either from a new color center ot the increase of a existed color center during crystal growth. induced absorption at 245 nm, which could be V_K centers.

There are studies on laser cooling of color centers in fluorides[110] and diamonds[114].The anti-Stokes emission occurs due to the population of vibronic levels of the centers ground electronic state by room-temperature phonons followed by absorption of a photon with energy below that of the zero-phonon transition in the center.

5.4 Laser cooling of Yb:YLF with X-ray induced point defects

When exposed to high intensities of radiation, radiation defects form, and functional decline is implied. In the case of laser refrigeration, which has stringent requirements for material quality, any changes in absorption or quantum efficiency can cause the failure of cooling. To investigate the impacts of color center formation in Yb:YLF, cooling tests were performed on as-synthesized Yb:YLF and x-ray irradiated Yb:YLF.

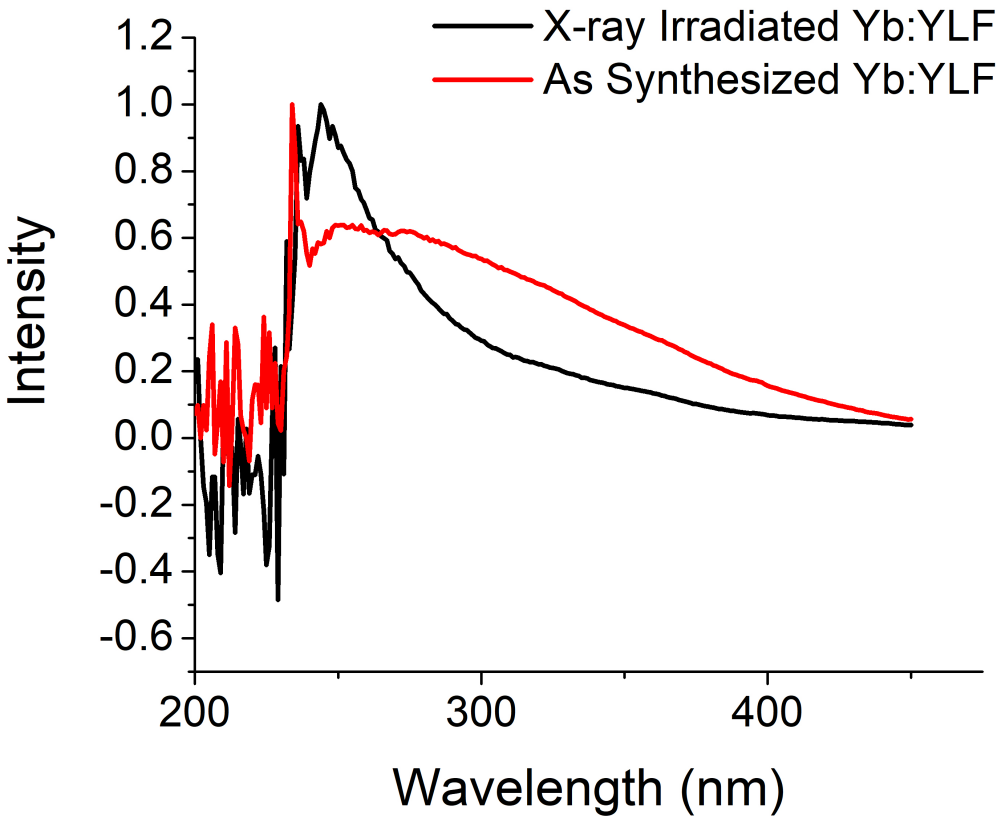

Figure 5.4: Normalized PLE spectra of X-ray irradiated Yb:YLF and as synthesized Yb:YLF. The emission wavelength:500 nm - 700 nm.

15 as-synthesized Yb:YLF and 15 x-ray irradiated Yb:YLF were tested.

To investigate the impacts of color center formation in Yb:YLF, cooling tests were performed on as synthesized Yb:YLF and X-ray irradiated Yb:YLF. Yb:YLF microcrystals sitting on a silica optical fiber were sealed in a cryostat. A similar setup in Figure 3.7a was used to pump individual microcrystals and to collect Yb PL. The mean fluorescence of Yb was analyzed to obtain the temperature change. 15 as synthesized Yb:YLF and 15 X-ray irradiated Yb:YLF were tested. The mean-wavelength vs. temperature calibration was performed by controlling the temperature of the cryostat and collecting corresponding mean wavelength shift. The $dT/d\lambda$ coefficients applied to the as synthesized Yb:YLF and X-irradiated Yb:YLF microcrystals were the average of three calibration of non-irradiated Yb:YLF and three irradiated Yb:YLF, respectively.

Without x-ray radiation, 14 out of 15 microcrystals were able to cool upon 1020 nm laser excitation. The average cooling temperature at the maximum excitation power of 50 mW is -14.3± 8.4 °C below room temperature. After irradiation, only 4 out of 15 Yb:YLF still cool, and the mean temperature of those cooling crystals decreases to -5.1± 4.4 °C below room temperature. The rest of the x-ray irradiated Yb:YLF heated up in response to the laser excitation, with the average temperature increase of 11.6± 19.7 °C above room temperature.

5.5 Discussions

There are three main hypotheses for the detrimental effects of the defects formed in the Yb:YLF, namely increased nonradiative relaxation, increased background absorption, and Yb^{2+} formation.

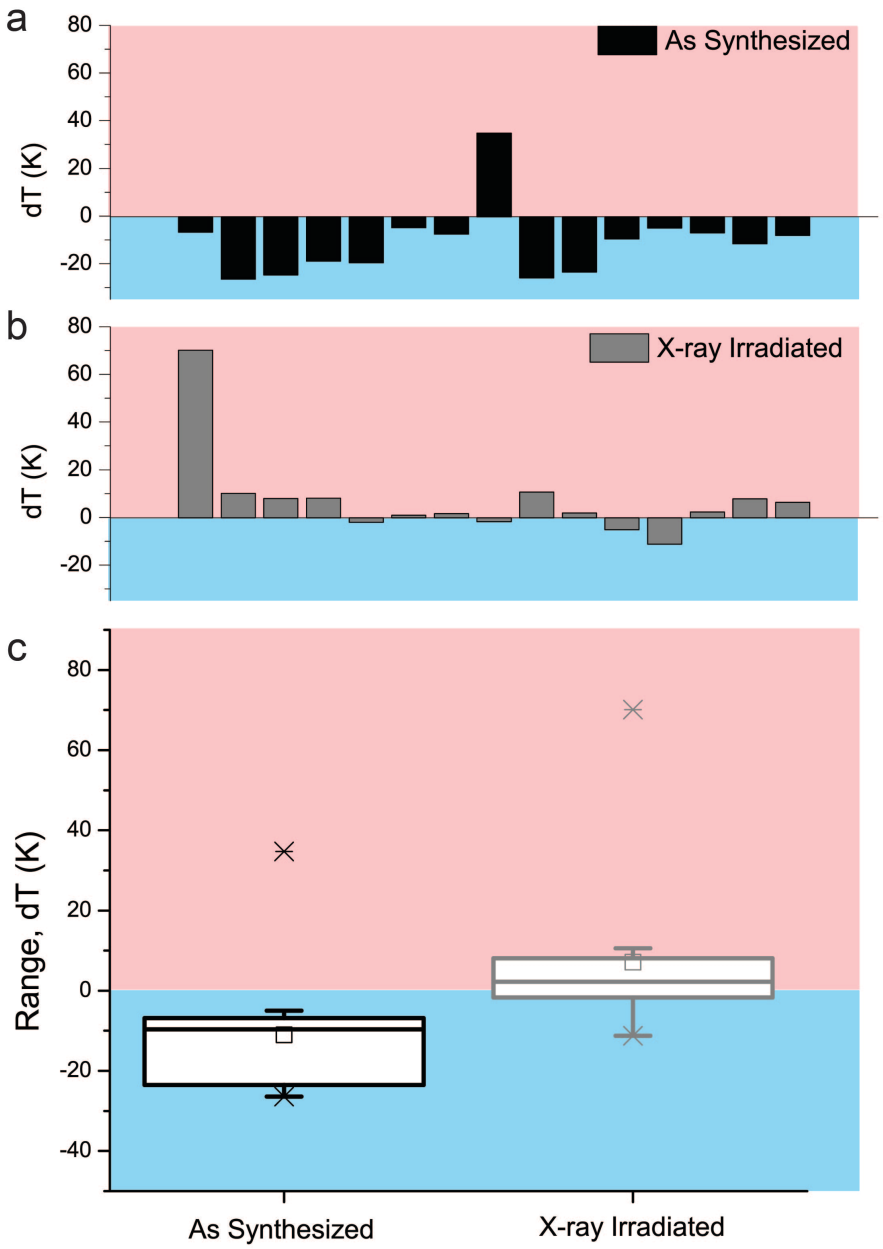

Figure 5.5: (a) Temperature change of 15 as synthesized Yb:YLF and 15 X-ray irradiated Yb:YLF upon 1020 nm laser excitation. (b) Statistic summary of temperature changes for as synthesized Yb:YLF and X-ray irradiated Yb:YLF.

5.5.1 Yb^{3+} Lifetime

The interaction of color centers and Yb^{3+} can alter the population of Yb^{3+} excited state. The energy transfer between Yb^{3+} and defects can increase the nonradiative relaxation rate and lower the cooling efficiency. Therefore, the defects may alter the relaxation rate of Yb^{3+} $^2F_{5/2}$ state.

The Yb^{3+} lifetime was measured to study the interaction between Yb^{3+} and defects. Same samples for the cooling test were used. Eight microcrystals were randomly selected from the as-synthesized YLF and x-ray irradiated YLF. In the decay curve obtained for the $^2F_{2/5}$ level for the YLF samples shown in Figure 5.6, the lifetime of both non-irradiated and irradiated Yb:YLF exhibits an exponential decay. However, there is a significant lifetime decrease after x-ray irradiation. The mean lifetime reduced from 1.75±0.01 ms to 1.53±0.05 ms Such change in lifetime is probably due to enhanced nonradiative relaxation or energy transfer between Yb ions and defects produced in samples. Similar lifetime decreases have also been observed in Yb-doped oxide glass[107], Tm-doped YLF bulk crystals[108], and Er-doped silica fibers[115]. Color centers were produced after irradiation, and the decreased lifeitme was attributed to nonradiative energy transfer from the excited lanthanides to radiation induced point defects.

5.5.2 Background Absorption

Defects with UV-Vis and NIR absorption bands can lower the cooling efficiency or even cause heating. The absorption in NIR can compete with the Yb^{3+} ions for 1020 nm absorption efficiency. The UV-Vis absorption band can recycle the Yb^{3+} emission and lower the escape efficiency via reabsorption, which decreases the external quantum efficiency. Either has a negative effect on the cooling efficiency described in Equation 1. However, it is challenging to measure the absorption spectra of individual

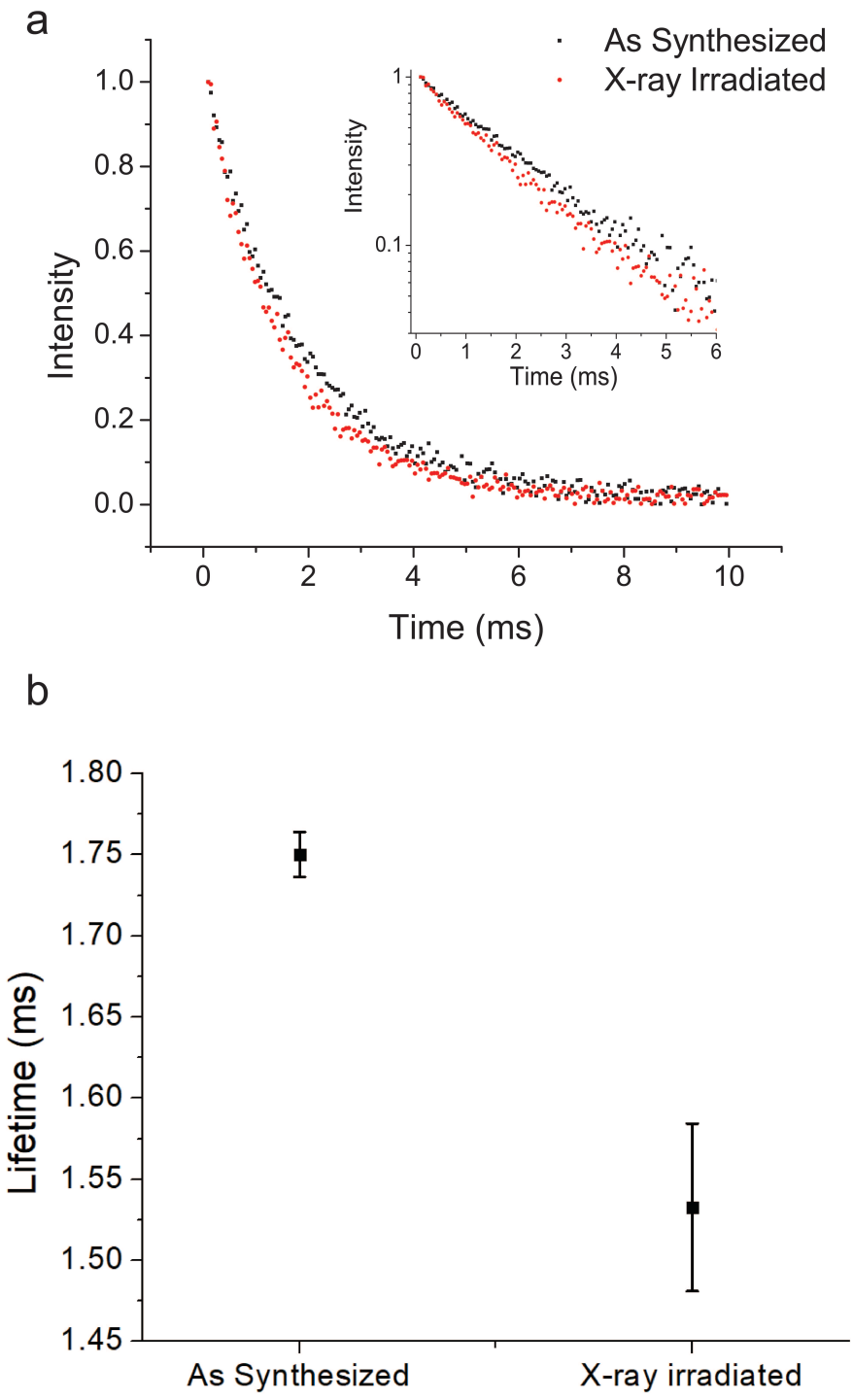

Figure 5.6: (a) The Yb $^2F_{5/2}$ excited state emission decay curves (insert: logarithm scale) and (b) fitted lifetime of five irradiated and five non-irradiated Yb:YLF micro-crystals.

microcrystals. Although there are some changes in the absorption and emission bands after x-ray irradiation according to the PLE and PL spectra in Figure **??**, the absorption cross-section cannot be compared quantitatively. The absorption measurement in bulk crystals is required.

5.5.3 Yb^{2+}

Yb^{3+} can be reduced to Yb^{2+} with the presence of free electrons. It is possible that Yb(III) was partially reduced to Yb(II), which has an absorption band in the visible region. A study shows the presence of Yb^{3+} in YLF reduced the intensity of the total irradiation-induced absorption, especially the amplitude of the F-absorption[116]. One possible explanation is the reduction of Yb^{3+} to Yb^{2+} as the competition of Yb^{3+} with F vacancies in capturing free electrons after x-ray irradiation.[117]. The presence of Yb(II) and Yb(III) can be distinguished by x-ray absorption near edge structure (XANES)[118]. This is one promising direction of future work.

5.6 Summary

Point defects are formed in Yb:YLF microcrystals after X-ray irradiation. Two defects with different thermal stability are formed according to TL spectra. These defects are assigned to F-centers tentatively based on EPR spectra. The laser cooling performance of such Yb:YLF deteriorated a lot after irradiation. This is probably due to the increased non-radiative relaxation rate with the interaction of point defects and Yb^{3+}.

Although X-ray induced point defects deteriorate the cooling performance of Yb:YLF, anti-Stokes emission of point defects observed in other materials brings the possibility of laser cooling[110]. The mechanism of such materials relies on the anti-Stokes emission of F-centers instead of lanthanides doping. The existence of different

kinds of luminescent centers and the possibility to vary their relative concentration by changing the irradiation, annealing and bleaching conditions make these crystals attractive from the point of view of finding a medium in which laser cooling may be observed. The strong electronphonon interaction in these centers results in broad emission bands.

Chapter 6

DESIGN OF A RADIATION-BALANCED FIBER-LASER VIA OPTICALLY ACTIVE CLADDING MATERIALS

6.1 Introduction

Ytterbium-based fiber-lasers are capable of operating at high (kW) continuous-wave powers due to a combination of high optical-optical conversion efficiency and broad gain bandwidth [119]. This has led to a number of important applications[120, 121] including additive manufacturing [122] and interstellar propulsion [123]. The superior power-scaling properties of Yb stem from an exceptionally low quantum defect for laser diode pumping. The low thermal load of Yb allows high dopant concentrations and thus high pump absorption per unit length. The development of clad-pumped fiber lasers remarkably scaled up the output power to kilowatt levels by improving the pumping configuration [124]. The output beams of individual fiber sources could be further combined coherently to reach higher output powers [125], approaching the megawatt range. In general, the key factors limiting the fiber laser performance are thermal management, optical nonlinearity, and damage [119]. Although optical fibers can dissipate heat due to their large surface area-to-volume ratio, significant heating of the core still occurs during high power operation. For clad-pumped fiber lasers, the thermal damage to the outer polymer cladding is a serious problem limiting the output power. For core-pumped fiber lasers, the degradation of the polymer coating is not as serious of a problem, but thermally-induced changes in the refractive index of the fiber lead to a thermal lensing effect, which reduces the effective mode area and results in multi-mode behavior [126, 127]. Such thermally-induced mode

distortion limits the power scaling of fiber lasers [128]. Current strategies to improve operational performance focus on increasing the material's thermal tolerance, such as using high-temperature polymers, all-glass fibers [119] and new pumping technologies like tandem-pumping to decrease the thermal loading density [129, 130].

One proposed approach for the development of high power lasers is radiation balanced lasing based on spontaneous, anti-Stokes photoluminescence [30]. ZBLAN glass is an available candidate for fiber materials. However, it is sensitive to humidity and lacks mechanical strength [131]. There have been theoretical modelings focused on the potential for radiation-balanced lasing based on Yb-doped silica fiber gain media [37, 36]. However, there were no reports of radiative cooling of Yb-doped silica glass materials for a long time. These observations have motivated the composite design of a fiber laser using optically active nanocrystals within the first cladding layer to extract the heat from the core during optical pumping. In principle, a composite cladding material that incorporates RE-doped nanocrystals could be used to extract heat from an optical fiber.

Recently, the cooling of Yb-doped silica glass has been achieved due to the improvement of fabrication techniques[35, 33]. The composite cladding design is therefore updated to an all-glass fiber amplifier. Also, clad pumping is adapted to provide higher pump power compared to core pumping.

This chapter first discusses a design for a radiation-balanced fiber-laser that uses a Yb:YLF/glass-based composite cladding material. The light in the composite cladding can cool the core Yb/SiO_2 gain medium based on the assumption that the Yb doped glass core cannot radiatively cool itself. In this design, nanocrystals in the cladding serve as the primary optically-active source for cooling. As a proof of principle, laser cooling of a YLF/polymer composite cladding material is experimentally demonstrated using far-field excitation. In addition, a detailed photothermal

heat transport analysis within both the core and cladding of such lasers is provided. Finally, the heat conduction equation is solved analytically to determine the core and cladding temperature distribution.

Then, a multi-mode clad pumped all-glass fiber laser design is introduced. All possible modes have been analyzed to determine the cladding size for the most efficient pumping. Both heating effects in the core due to high Yb-dopant concentration and laser cooling in the cladding via the cooling grade Yb-doped silica glass are considered.

6.2 Design of a single-mode fiber laser via optically active composite cladding materials

Here we consider a single-mode fiber with a step-index profile with the highest output laser quality. For simplicity, in this work, we consider the case of pumping the fiber laser through the inner core. The first cladding can serve as the pump in many high-power fiber laser designs. The model we present below is general, and in future work, we will treat the case of pumping the core through a multi-mode fiber cladding. As illustrated in Fig. 6.2, the core material is Yb-doped glass with a small diameter. This Yb-doped glass amplifies the laser signal and generates heat inside the core. The cladding consists of a thin inner region doped with YLF nanocrystals and an outer region free of nanocrystals. The cladding has a lower optical refractive index than the core. Here R_{co} and R_{cl} are the core radius and total cladding radius, which are 0.69 μm and 62.5 μm, respectively. Additional fiber parameters are listed in Table 6.1.

The analysis below demonstrates that the fiber design based on a Yb:YLF-composite cladding has a lower temperature throughout the entire fiber than the case of fiber without the nanocrystal-composite cladding. Furthermore, the model we present is general and may be extended to multi-mode fiber designs, including those with optically active glass-based cladding materials, including Yb/SiO_2 or Yb/ZBLAN. We do not consider the case of radiation balanced lasing through an optically-active

nanocrystal-composite fiber-core, given the likelihood of detrimental Rayleigh scattering that would prevent high power lasing within the core.

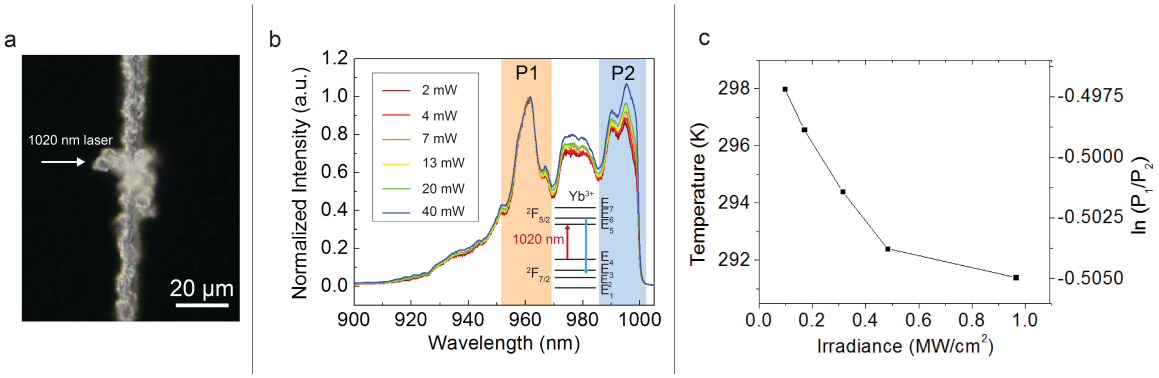

Figure 6.1: (a) Optical microscope image of Yb:YLF microcrystals on an etched fiber. (b) Yb:YLF photoluminescence spectra at various laser irradiances, normalized to the P1 peak. At higher irradiance the P2 peak increases in intensity. P1 and P2 are electronic transitions $E_6 - E_2$ and $E_5 - E_2/E_3$, respectively. Energy levels values could be found in Ref [132]. The integration ranges for P1 and P2 are from 952 nm to 968 nm and 986 nm to 1000 nm, respectively. (c) The integrated intensity ratio of P1 and P2 peaks with the corresponding calibrated temperature at each laser irradiance. Copyright ©2021 Optica Publishing Group.

6.3 Laser cooling of a YLF/polymer composite cladding material

6.3.1 Ytterbium-Doped Lithium Yttrium Fluoride Synthesis

The hydrothermal method used to synthesize single crystals of 10%Yb:YLF nanocrystals was performed following modifications to Roder *et al.* [98]. Yttrium chloride hexahydrate ($YCl_3{\cdot}6H_2O$) and ytterbium chloride hexahydrate ($YbCl_3{\cdot}6H_2O$) were of 99.999% and 99.998% purity, respectively. Lithium fluoride (LiF), lithium hydroxide monohydrate ($LiOH{\cdot}H_2O$), ammonium difluoride (NH_4HF_2), and ethylenediaminetetraacetic acid (EDTA) were analytical grade and used directly in the synthesis without

any purification. All chemicals were purchased from Sigma-Aldrich. For the synthesis of Yb:YLF, 0.585 g (2 mmol) of EDTA and 0.168 g (4 mmol) $LiOH{\cdot}H_2O$ were dissolved in 10 mL Millipore DI water and heated to approximately 80 °C while stirring. After the EDTA was dissolved, 1.8 mL of 1.0 M YCl_3 and 0.2 mL of 1.0 M $YbCl_3$ were added and continuously stirred for 1 hour. This mixture is denoted as solution A. Subsequently, 0.105 g (4 mmol) of LiF and 0.34 g (8 mmol) of NH_4HF_2 were separately dissolved in 5 mL Millipore DI water and heated to approximately 70°C while stirring for 1 hour. This solution is denoted as solution B. After stirring, solution B was added dropwise into solution A while stirring to form a homogeneous white suspension. After 30 minutes, the mixture was transferred to a 23 mL Teflon-lined autoclave (Parr 4747 Nickel Autoclave Teflon liner assembly) and heated to 180 °C for 72 hours in an oven (Thermo Scientific Heratherm General Protocol Oven, 65 L). After the autoclave cooled to room temperature, the Yb:YLF particles were sonicated and centrifuged at 4000 rpm with ethanol and Millipore DI water three times. The final white powder was then dried at 60°C for 12 hours, followed by calcination at 300°C for 2 hours inside a quartz tube in a furnace (Lindberg blue).

6.3.2 PL Measurements and Temperature Calibration

A 1020 nm laser from a fiber-coupled single-mode laser diode (QPhotonics, QFBGLD-1020-400) was focused to a diffraction-limited spot (radius = 1.2 μm) using a long working distance 50x objective (Mitutoyo, M Plan Apo), and the same objective collected photoluminescence (PL). The PL spectra were recorded with a spectrometer (Ocean Optics, NIR512). A 1000 nm short-pass filter (Thorlabs, FESH1000) was used to filter the laser line. Ten spectra, collected for 100 ms each, were averaged to obtain the final PL spectrum. The temperature-calibrated PL spectra were obtained using a cryostat (Janis, ST500) in which the sample temperature was maintained at various

points from 300 K to 350 K by a temperature controller (Lake Shore, 335) with a resolution of 0.01 K.

6.3.3 YLF temperature analysis

Hydrothermal synthesis is a fast and scalable method to produce high-quality 10%Yb:YLF laser-cooling materials. Figure. 6.1(a) shows a cladding-etched bare glass fiber with YLF crystals attached to it using a layer of commercially available fluoropolymer CYTOP with an ultra-low NIR absorption coefficient. The fiber was illuminated perpendicularly in the far-field with a 1020 nm continuous-wave (CW) laser focused onto a crystal at a range of irradiances up to 1 MW/cm^2. PL spectra were normalized to the peak at 960 nm. These PL spectra arise from ytterbium's electronic transitions between $^2F_{5/2}$ and $^2F_{7/2}$ manifolds illustrated in Fig. 6.1b. The 1020 nm laser pumps a hole from energy level E_5 energy level E_4. The holes are then upconverted further by phonons within the $^2F_{7/2}$ manifold followed by anti-Stokes emission. The radiative relaxation following upconversion transports the heat extracted from the lattice to free space, resulting in cooling. The intensity ratio of P1 and P2 bands in Fig. 6.1(b) is temperature dependent based on a Boltzmann distribution, and lower ratio values correspond to lower temperatures. More detailed spectroscopic properties such as absorption and emission cross-sections of bulk crystals can be found in the literature [133, 134]. Nanoscale materials have large surface-area-to-volume ratios, which can lead to a considerable amount of non-radiative surface losses. Non-radiative relaxation can be mitigated through the use of undoped surface-capping layers[135]. Theoretical predictions also have been made that nanoscale grains may also have different vibrational density of states that may help enhance laser refrigeration[136]. We assume there is no significant spectroscopic change for the particles in Fig. 6.1a compared to the bulk crystals as our single-crystal emission profile is similar to those of bulk

crystals. After calibrating the intensity ratio to the temperature, we have found that the Yb:YLF crystal decreases in temperature by 6.6 K as shown in Fig. 6.1(c). At each laser irradiance, a mean P1/P2 ratio was obtained by averaging six measurements, and the error bars represent one standard deviation, which is smaller than 1% of the mean values. The hydrothermally-synthesized laser cooling Yb:YLF nanocrystals can be mixed within the cladding material at various volumetric fractions. When the nanocrystals are embedded in the cladding near the core-shell interface, we expect that the evanescent field will optically pump the cooling materials and lower the local temperature through anti-Stokes photoluminescence. Rayleigh scattering can be reduced by index matching the composite host material with the index of YLF (n_{YLF} ~1.47).

6.4 Heat-transfer analysis

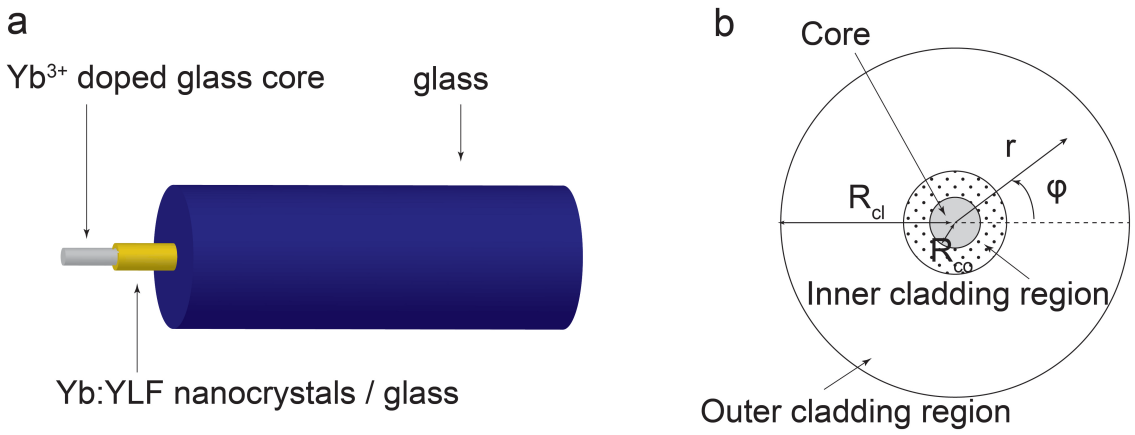

Figure 6.2: (a) The core of the fiber is Yb-doped glass. The inner region of the cladding (yellow) is composed of glass and YLF nanocrystals, and the outer region of the cladding (blue) is made of the same glass as the inner cladding region, but with no Yb:YLF. (b) The fiber cross-section.

Although both analytical and numerical solutions for the optical fiber temperature

distribution have been developed in the past, they are limited to simpler fiber designs. Previous analyses considered radial heat transfer alone involving several approximations [137]. For example, the heat source was assumed constant inside the core, and the heat generated in the cladding was neglected [138]. The heat source profile was simplified and limited to the core in previous numerical solutions. The evanescent field in the cladding and the pumping mode were not considered, including the cases of clad-pumped fibers [139, 140]. Here we apply the waveguide theory of optical fibers to establish the rigorous electromagnetic heat source [141] extending across both core and cladding regions. The evanescent power extending into the cladding layer is considered and utilized as the excitation source of the laser refrigeration materials.

For a cylindrical optical fiber the temperature is described in three dimensions by the energy equation:

$$\rho\hat{c}\frac{\partial T}{\partial t} = \kappa[\frac{1}{r}\frac{\partial}{\partial r}(r\frac{\partial T}{\partial r}) + \frac{1}{r^2}\frac{\partial^2 T}{\partial \phi^2} + \frac{\partial^2 T}{\partial z^2}] + \dot{Q}''', \tag{6.1}$$

in which ρ is the mass density of the fiber [kg/m^3], $\hat{c}$ is the heat capacity [J/(kg·K)], κ is the thermal conductivity [W/(m·K)], T is the temperature [K], $\dot{Q}'''$ is the rate of heat generation (or depletion) per unit volume due to electromagnetic (EM) heating or cooling [J/(m$^3 \cdot s$)]. The EM heat source (or sink) is discussed in more detail in section 6.5. In this model, it is assumed that the thermal properties of the core and cladding are the same because they are similar glass materials. If the thermal properties of the core and cladding are different, then there is no analytical solution. The heat source is found to be nearly independent of the angular coordinate, ϕ. Consequently, the angular conduction term in Eq.6.1 can be neglected.

It is convenient to write the energy equation in a dimensionless form:

$$\frac{\partial \Theta}{\partial \tau} = \frac{1}{\xi}\frac{\partial}{\partial \xi}(\xi\frac{\partial \Theta}{\partial \xi}) + (\frac{R_{co}}{L})^2\frac{\partial^2 \Theta}{\partial \zeta^2} + S(\xi, \phi, \zeta), \tag{6.2}$$

by introducing the dimensionless variables:

$$\Theta = \frac{T - T_\infty}{T_\infty}, \xi = \frac{r}{R_{co}}, \zeta = \frac{z}{L}, \tau = \frac{\kappa}{\rho \hat{c}} \frac{t}{{R_{co}}^2}, S = \frac{R_{co}^2 Q'''}{\kappa T_\infty}. \tag{6.3}$$

Here Θ is the dimensionless temperature, and T_∞ is the temperature of the surrounding medium, which is also the initial temperature of the fiber.

The solution is in a product form

$$\Theta(\xi, \zeta, \tau) = \sum_m \sum_n A_{mn}(\tau) X_m(\xi) Z_n(\zeta), \tag{6.4}$$

where

$$X_m(\xi) = J_0(\gamma_m \xi), \ m = 1, 2, 3, ... \tag{6.5}$$

$$Z_n(\zeta) = \cos(n\pi\zeta), \ p = 0, 1, 2, 3, ... \tag{6.6}$$

J_0 in Eq.6.5 is the zero-order Bessel function. The eigenvalues γ_m satisfy the boundary condition

$$\left. \frac{dX_m(\xi)}{d\xi} \right|_{\xi_s} = -\mathrm{Bi} \cdot X_m(\xi_s), \tag{6.7}$$

in which $\xi_s = R_{cl}/R_{co}$, and the Biot number is defined by

$$\mathrm{Bi} = \frac{\mathrm{Nu} \cdot \kappa_s \cdot R_{co}}{2\kappa R_{cl}}. \tag{6.8}$$

The Nusselt number (Nu) is given by

$$\mathrm{Nu} = \frac{2R_{cl}h}{\kappa_s}, \tag{6.9}$$

where h is the heat transfer coefficient for transport between the fiber and the surroundings, and κ_s is the thermal conductivity of the surroundings. For heat transfer

from a cylinder to a stagant medium Nu = 0.32 [142]. The time-dependent coefficients $A_{mn}(\tau)$ in Eq.6.4 are given by

$$A_{mn}(\tau) = \frac{1 - e^{(-\lambda_{mn}^2 \tau)}}{\lambda_{mn}^2} \int_0^{\xi_s} \int_0^1 \frac{S(\xi', \phi, \zeta') \xi' X_m(\xi') Z_n(\zeta') d\xi' d\zeta'}{\|X_m\|^2 \|Z_n\|^2}, \tag{6.10}$$

in which

$$\lambda_{mn}^2 = \gamma_m^2 + \left(\frac{R_{co}}{L}\right)^2 (n\pi)^2, \tag{6.11}$$

and the norms are

$$\|X_m\|^2 = \int_0^{\xi_s} \xi' [J_0(\gamma_m \xi')]^2 d\xi', \tag{6.12}$$

$$\|Z_n\|^2 = \int_0^1 \cos^2(n\pi\zeta') d\zeta'. \tag{6.13}$$

The primes indicate dummy variables of integration.

The steady state solution is obtained by taking the limit as $\tau \to \infty$ to give

$$A_{mn} = \frac{\int_0^{\xi_s} \int_0^1 S(\xi', \phi, \zeta') \xi' X_m(\xi') Z_n(\zeta') d\xi' d\zeta'}{\lambda_{mn}^2 \|X_m\|^2 \|Z_n\|^2}, \tag{6.14}$$

6.5 Electromagnetic heat source

The volumetric rate of heat generated inside the fiber is related to the EM-field associated with the laser irradiation [146], which is given by the equation

$$\dot{Q}'''(r, \phi, z) = \frac{1}{2} \sigma_i (\boldsymbol{E} \cdot \boldsymbol{E^*}), \tag{6.15}$$

Table 6.1: **Fiber parameters**

Parameters	Values
Core radius R_{co}	0.69 μm
Composite cladding radius	5 μm
Total cladding radius R_{cl}	62.5 μm
Fiber length L	1 m
Wavelength λ	1020 nm
Core refractive index N_{co}	1.52+3.88E-8i [143]
Cladding glass refractive index N_{matrix}	1.4705 + 1.003E-8i [144]
Yb:YLF refractive index N_{YLF}	1.4705 + 5.346E-6i [145]
Glass thermal conductivity κ	1.5 W/(m·K)
Air thermal conductivity κ_s	0.02624 W/(m·K)
Pumping irradiance	100 kW/(m^2)
Room temperature T_∞	298 K

where $\boldsymbol{E}$ and $\boldsymbol{E^*}$ are the internal electric-field vector and its complex conjugate, respectively, and σ_i is the effective conductivity of the fiber core or cladding material. Two wavelengths propagate through the fiber during lasing - the pump and lasing wavelength. We do not distinguish between these two wavelengths for simplicity in this model. Only one high-power fundamental mode was considered as the EM heat source. Since Yb:YLF can be refrigerated optically in a wide excitation wavelength range (1005 nm -1065 nm, at room temperature [23]), both pump and lasing wavelengths could lie in this range and excite the cooling of Yb:YLF within the cladding. It is not necessary to calculate the heat sources for the pump and lasing wavelengths separately. In this case, we assume that the propagating light wavelength is 1020 nm, under which excitation Yb:YLF has been predicted to reach its lowest temperature [147]. We also make the simplifying assumptions that the anti-Stokes emission from YLF within the cladding is not reabsorbed and that Rayleigh scattering is negligible. Snyder and Love [141] have tabulated the components of the electric vectors for optical fiber waveguides having a step-index profile which we use below. Figure.

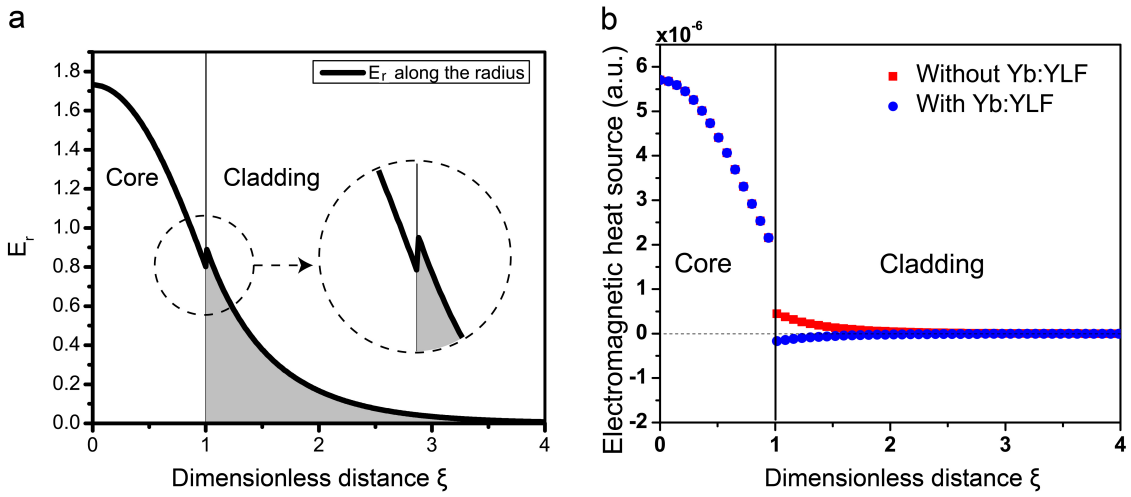

Figure 6.3: The EM-field within a single-mode guided step index fiber. (a) The radial electric field in the core and cladding for $\phi = 90°$. (b) The radial distribution of the EM heat source within the fiber without Yb:YLF cladding (red) and a fiber with 10% volume fraction of Yb:YLF mixed into the cladding (blue). Copyright ©2021 Optica Publishing Group.

6.3(a) shows the radial component of the electric field at $z = 0$, $\phi = 90°$ for a vertically polarized (along $\phi = 90°$) laser propagating in the z-direction. The highlighted discontinuity at the core-cladding interface is due to the boundary condition:

$$n_{co}^2 E_r^{co}|_{\xi=1} = n_{cl}^2 E_r^{cl}|_{\xi=1}. \tag{6.16}$$

The optical field extending into the cladding excites the YLF leading to local laser refrigeration. This evanescent field penetrates only a short distance into the cladding layer, so the Yb:YLF nanocrystals only need to be incorporated in that narrow region. In our design, the thickness of this inner region of the cladding, which contains the cooling materials, is slightly greater than the evanescent penetration thickness. This inner cladding layer is composed of YLF nanocrystals uniformly dispersed within a

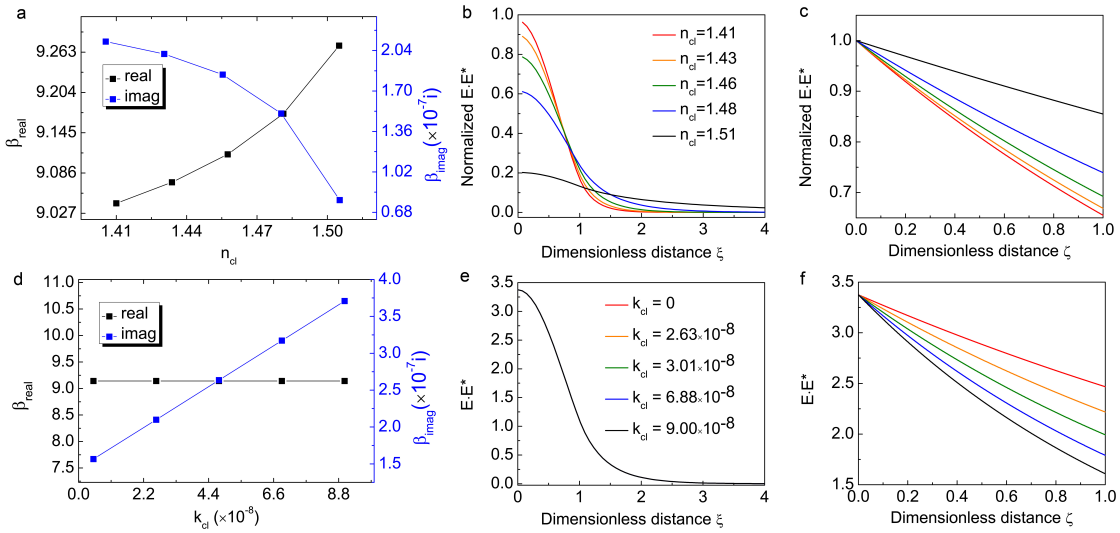

Figure 6.4: The effects of the cladding refractive index on the EM-field. Here refractive indices of core and the fiber geometry are the same. (a) Propagation constant of the fiber with various values of n_{cl}. (b) Radial distribution of annular normalized $E \cdot E^*$. (c) Longitudinal distribution of $E \cdot E^*$. Color legends are the same as (b). To compare the longitudinal decay rate, the maxima of the energy flux are normalized to 1. (d) Propagation constant of the fiber with various values of k_{cl}. (e) Radial distribution of $E \cdot E^*$. (f) Longitudinal distribution of $E \cdot E^*$. Color legends are the same as (e). Here, (e) and (f) are not normalized because $E \cdot E^*$ does not change with various k_{cl} at $\zeta = 0$.

glass matrix. This glass matrix is not Yb-doped as the core glass, but it still absorbs slightly and generates heat. The outer cladding without the nanocrystals serves only as a mechanical supporting layer to protect the core. Since there is no electric field in this region, only the heat generated inside the core and the inner cladding region are considered.

The effective electrical conductivity of the fiber core or cladding materials is given by

$$\sigma_i = \frac{4\pi \mathrm{Re}\{N_i\}\mathrm{Im}\{N_i\}}{\lambda \mu c}, \tag{6.17}$$

in which $N_i = n_i + ik_i$ is the complex refractive index of the fiber core or cladding. $n_i = \mathrm{Re}\{N_i\}$ is the real part and $k_i = \mathrm{Im}\{N_i\}$ is the imaginary part of the refractive index. λ is the wavelength in free space, μ is the magnetic permeability, and c is the velocity of light in vacuum. The heat source in the core is

$$\dot{Q}'''_{co}(r,\phi,z) = \frac{1}{2}\sigma_{co}(\boldsymbol{E}\cdot\boldsymbol{E^*}) = \frac{2\pi n_{co}k_{co}}{\lambda\mu c}(\boldsymbol{E}\cdot\boldsymbol{E^*}). \tag{6.18}$$

The EM source in the cladding is composed of the heating associated from the matrix material and the cooling due to the Yb:YLF nanocrystals. The thermal source in the cladding is given by

$$\begin{aligned}\dot{Q}'''_{cl}(r,\phi,z) = (1-v)\frac{1}{2}\sigma_{cl}^{\mathrm{matrix}}(\boldsymbol{E}\cdot\boldsymbol{E^*}) \\ +(-)v\eta_{cooling}\frac{1}{2}\sigma_{cl}^{\mathrm{YLF}}(\boldsymbol{E}\cdot\boldsymbol{E^*})\end{aligned} \tag{6.19}$$

where v is the volume fraction of Yb:YLF nanocrystals in the composte matrix, $\sigma_{cl}^{\mathrm{matrix}}$ and $\sigma_{cl}^{\mathrm{YLF}}$ are the effective conductivities for the matrix glass material and Yb:YLF nanocrystals in the cladding respectively, and $\eta_{cooling}$ is the cooling efficiency of the Yb:YLF. n_{YLF}, k_{YLF} and n_{matrix}, k_{matrix} are the real and imaginary terms of the

refractive indices for Yb:YLF and the cladding glass materials. The competition of the heating and cooling processes in the cladding depends on the volume fraction of YLF in the cladding, the refractive indices of YLF and matrix materials, and also the overall cooling efficiency. According to calculations shown in Fig. 6.3(b), when there is no Yb:YLF cooling nanocrystals in the cladding, both the core and cladding layers act as heating sources. When Yb:YLF nanocrystals are incorporated in the cladding with a volume fraction of 10 %, and the cooling efficiency of Yb:YLF is 2% ($v = 10\%, \eta_{cooling} = 2\%$), the cladding layer acts as a cooling source. The theory predicts heating in the cladding can be completely eliminated with a YLF volume fraction of 8%.

6.5.1 Electric Fields

The refractive index is the most important material property for optical fiber in that every waveguide parameter depends on it. For the core material, it is obvious that larger k results in higher absorption and increased heat generation. However, the effect of the cladding refractive index is less obvious. We have investigated how varying both the real and imaginary components of the refractive index of the cladding impacts laser cooling. The core parameters were assumed to remain constant while changing the real or imaginary components of the cladding. For a single-mode fiber, the single-mode condition: $V = (2\pi/\lambda)a(n_{co}^2 - n_{cl}^2)^{1/2} < 2.405$ is satisfied. Therefore, $\Delta n = n_{co} - n_{cl}$ should be smaller than 0.12. The electric field, which is the solution of the Maxwell equations for the waveguide boundary condition [141], is given by

$$\boldsymbol{E}(r, \phi, z) = \mathbf{e}(r, \phi)e^{i\beta z}, \tag{6.20}$$

in which β is the propagation constant. All the components of $\mathbf{e}(r,\ \phi)$ are listed in Table 12-3 in [141]. The propagation constants for fibers with various values

of n_{cl} and k_{cl} are plotted in Fig. 6.4(a) and Fig. 6.4(d). The real part of the propagation constant describes the rate of phase change with z, while the imaginary part constitutes the decay rate of the electric field. For small n_{cl}, or a larger Δn, β_{real} is smaller and the electric field is more confined within the core (Fig. 6.4(b)). β_{imaj} decreases with increasing n_{cl}, which implies a lower decay rate along the z-axis (Fig. 6.4(c)). This suggests that a smaller Δn is helpful for cooling because more energy flux is produced in the cladding layer to excite the composite cooling region adjacent to the core. However, there is a trade-off in that more pump power is required to achieve an equivalent output power from the core. Additionally, the coupling efficiency of the pump also needs to be considered. When tuning the imaginary part of the cladding refractive index, β_{real} does not change with k_{cl} while the imaginary part of the propagation constant, β_{imag}, increases with larger k_{cl}. With the same β_{real}, the radial electric field distributions are identical when k_{cl} is varied. To reduce the energy decay along z, a smaller k_{cl} for the cladding layer is optimal.

6.5.2 Parametric Study - YLF Fraction

To evaluate the cooling performance of the nanocrystals in the fiber, we calculated temperature distributions using the analytical solution presented above implemented using the Python programming language. The YLF volume fractions ranged from 0% to 10%. The other parameters used in the calculations are listed in Table 6.1. To minimize the scattering in the inner layer of the cladding, the cladding glass was selected to match the real part of the refractive index of the Yb:YLF nanocrystals. This can be achieved by adjusting the concentration of dopants within the glass. We used effective medium theory [148] for composite materials to calculate the effective refractive indices for the more complicated condition in which the indices of the Yb:YLF and glass do not match. These cases are discussed in Section 6.5.3. Figure. 6.5 shows the

temperature of the fibers with 0%, 5%, and 10% Yb:YLF nanocrystals in the inner cladding layer. Figure. 6.5(a) is a plot of the fiber temperature distribution from the center to the outer surface of the cladding. Clearly, increasing the volume fraction of Yb:YLF within the cladding leads to a decrease in the steady-state temperature of the fiber. Temperature reductions of 12 K for a 5% Yb:YLF incorporated fiber and 19 K for a 10% Yb:YLF incorporated fiber (Fig. 6.5(b)) are predicted. Experimentally it is realistic to pursue a volume fraction of up to 20% YLF, which would reduce temperatures even further.

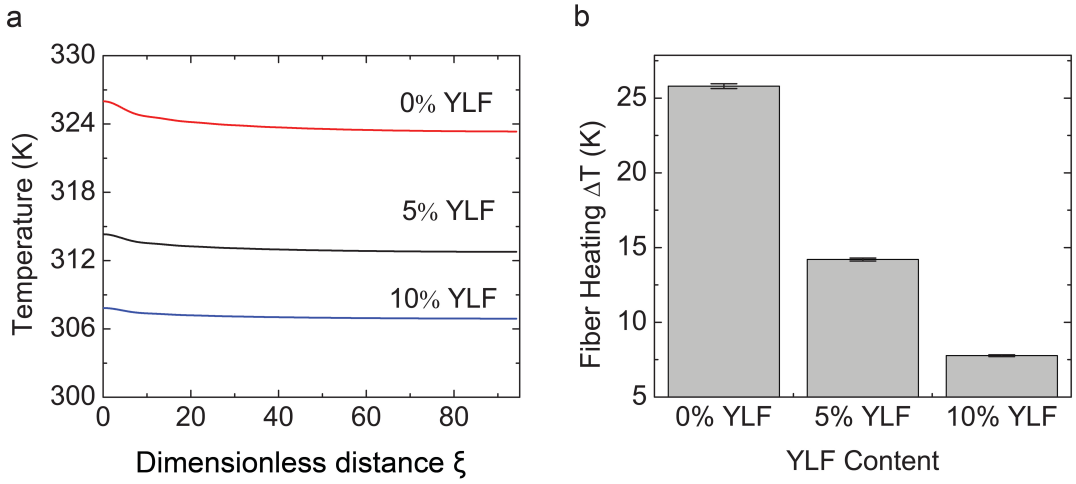

Figure 6.5: The fiber temperature for various volume fractions of Yb:YLF Incorporated in the inner cladding layer. (a) The radial temperature distribution for no Yb:YLF, 5%, and 10% Yb:YLF in the inner cladding. (b) The average temperature for the whole volume of the fiber for various amounts of Yb:YLF. Copyright ©2021 Optica Publishing Group.

6.5.3 Parametric Study - Cladding Glass Refractive Index

In Section 6.5.1 we considered how the complex electric field depends on the cladding's refractive. In section 6.5.2 we considered the effect of the nanocrystal's volume frac-

tion on cooling. Here in section 6.5.3 we discuss the temperature response to various cladding glass refractive indices when 10% of Yb:YLF nanocrystals are doped within the inner cladding. Effective medium theory [148] may be used to calculate the effective refractive index of a composite material with 10% Yb:YLF - 90% glass. The real and imaginary terms of the effective refractive index are defined as

$$n_{eff} = [A + (A^2 + B^2)^{1/2}]^{1/2}/2, \tag{6.21}$$

and

$$k_{eff} = [-A + (A^2 + B^2)^{1/2}]^{1/2}/2, \tag{6.22}$$

respectively. The coefficients A and B are defined by

$$A = v(n_{YLF}^2 - k_{YLF}^2) - (1 - v)(n_{matrix}^2 - k_{matrix}^2), \tag{6.23}$$

and

$$B = 2n_{YLF}k_{YLF}v + 2n_{matrix}k_{matrix}(1 - v). \tag{6.24}$$

Under the same assumption as Section 6.5.1, the core index N_{co} and Yb:YLF nanocrystal index N_{YLF} are constants listed in Table 6.1. The real refractive index of the cladding glass n_{matrix} was the only variable. Here only the change in real refractive index was considered because the imaginary refractive index had a negligible effect on the radial electric field distribution according to Fig. 6.4(e). The effective cladding refractive indices calculated with the above equations are listed in Table 6.2.

The effective thermal conductivity of this inner cladding region layer was not considered. The reason is, first, the fluoride thermal conductivity is similar to glass; second, it is a very thin layer incorporated with nanocrystals compared to the entire cladding region without the nanocrystals. It's reasonable to neglect the thermal con-

ductivity variation for the heat transfer model, which considers the thermal properties of the entire fiber. However, this thin layer is where the evanescent field is located. So the optical properties of this region are important, and we must apply the effective medium theory to obtain a reliable EM-field distribution.

Table 6.2: **Waveguide parameters: effective refractive indices and propagation constants**

n_{matrix}	n_{eff}	k_{eff}	Propagation constant β
1.4100	1.4162	3.5638E-07	9.0490+6.3301E-07i
1.4280	1.4323	3.5262E-07	9.0703+7.0196E-07i
1.4460	1.4485	3.4883E-07	9.0962+7.9586E-07i
1.4640	1.4646	3.4499E-07	9.1288+9.4015E-07i
1.4820	1.4809	3.4110E-07	9.1716+1.1776E-06i
1.5000	1.4971	3.3783E-07	9.2325+1.6104E-06i

To calculate the EM source and the resulting fiber temperature, we assumed the pumping beam had the same transverse intensity profile as the guided mode. That is to say, no matter how much the numerical aperture changes with the cladding index, the total power coupled into the beam is the same for fibers with different cladding indices. Thus the power density at the beginning of the fiber (z = 0) should be normalized as

$$\int_0^{\xi_s}\int_0^{2\pi} \mathbf{E}(\xi',\phi',0)\cdot\mathbf{E}^*(\xi',\phi',0)d\phi' d\xi' = \text{Irradiance} \tag{6.25}$$

When the n_{matrix} is high, the effective n_{cl} is close to the n_{co}. As plotted in Fig. 6.4(b), more electric field power extends into the cladding layer. After the normalization, the power in the core is much lower than those with lower effective cladding indices, which means lower heat generated inside the core. This agrees with the calculated equilibrium temperature results in Fig. 6.6. When n_{matrix} is small, the EM energy

is confined more within the core due to the larger index difference between the core and cladding, and thus a higher temperature.

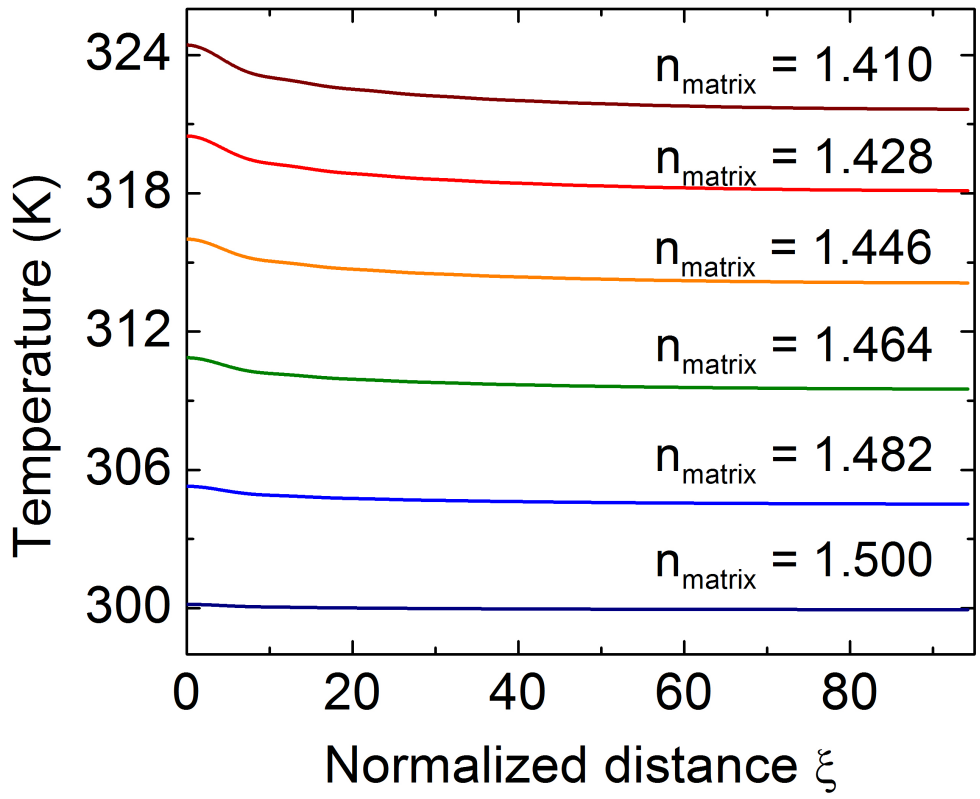

Figure 6.6: The radial temperature distribution of fibers with various cladding glass refractive indices, $v = 10\%$. Copyright ©2021 Optica Publishing Group.

6.5.4 Parametric Study - Cladding Thickness

We have also investigated the impact of the cladding thickness on steady-state temperatures. Figure 6.7 shows the time-dependent center temperature ($\xi = 0$) of the fiber as a function of cladding thickness. Clearly, as the cladding thickness increases,

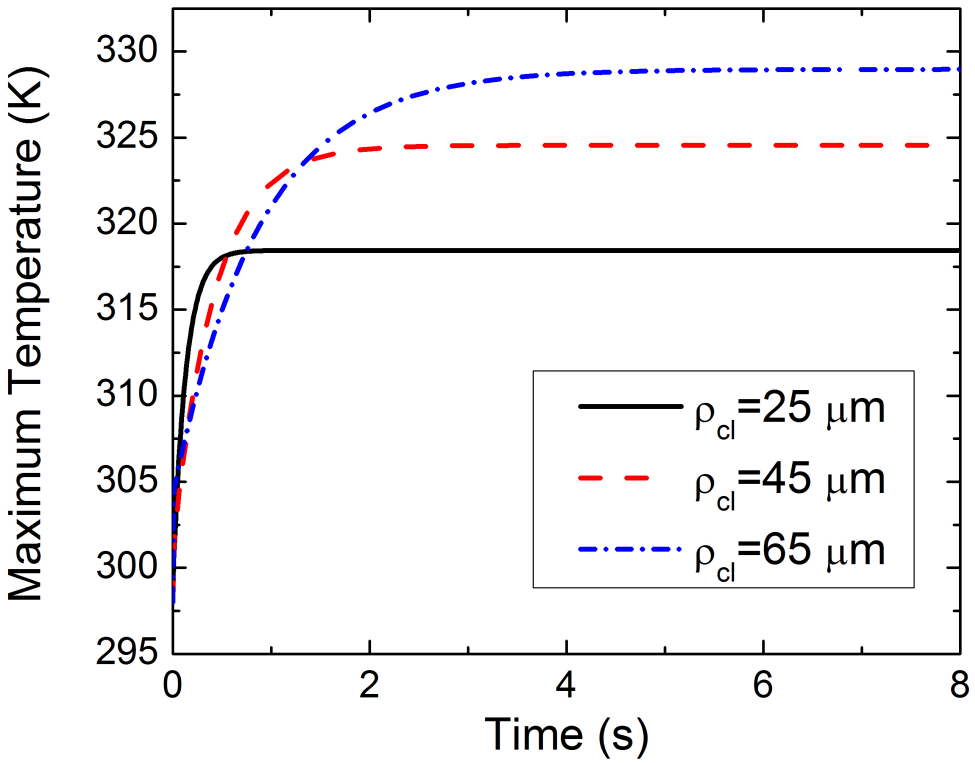

Figure 6.7: The time-resolved temperature for various cladding thicknesses. Copyright ©2021 Optica Publishing Group.

the overall temperature of the fiber increases. It is also obvious that longer times are required to reach a steady state with increased cladding thickness. Ideally, the cladding should be as small as possible, but sufficient thickness is needed to ensure satisfactory mechanical properties or a multi-mode pumped-cladding configuration.

6.6 Design of a multi-mode clad-pumped all-glass fiber laser

In contrast to our previous work, multi-mode fiber laser designs rely on a multi-cladding configuration rather than core-pumping. Recently, laser cooling of Yb-doped silica glass has been observed based on pioneering work by the Mafi group and collaborators. We have continued discussions with the Mafi group towards an analytical, core-pumped heat-transfer model to develop an all-glass cladding-pumped fiber RBL design.

With an anti-Stokes cooling inner cladding, the fiber is cladding-pumped at the wavelength of 1040 nm, amplifying the signal of 1060 nm in the core. The silica glass in the single-mode core has a high Yb doping level for lasing, whereas the inner cladding consists of cooling-grade silica glass with a low Yb concentration. Multi-mode pump sources propagate along with the inner cladding, scaling up the signal in the core and extracting the heat generated inside the core due to quantum defects and concentration quenching.

Figure 6.8 shows a schematic of the new fiber design. The core glass is heavily doped with Yb and works as the gain medium. The diameter is 2 um. The 125 um diameter inner cladding glass is the cooling grade silica glass 2.06 wt.% Yb^{3+} (in the form of Yb_2O_3) and co-doped with Al_2O_3 and F^- The cooling efficiency is 1.15%. The outer cladding is pure silica glass, and the diameter is 200 um.

A cladding-pumped, which uses a more sophisticated double-clad fiber structure,, is applied to provide higher pump power. The pump is coupled into the inner cladding.

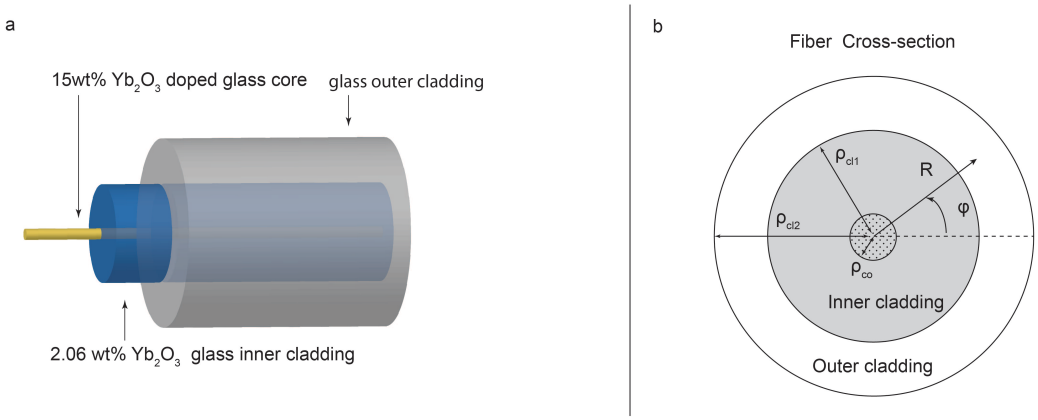

Figure 6.8: (a) The schematic of the clad-pumped single mode fiber. The amplified laser signal at 1060 nm wavelength propagates in the single mode Yb-doped core and the pump light at 1040 nm wavelength propagates in the multi-mode inner cladding. (b) The fiber cross-section

The large size of the inner cladding allows pumping with numerous pump diodes that provide several kilowatts of low-cost, low-brightness optical power[149].

The pump-induced single-mode laser (1060 nm) propagates in the core and generates heat. The pump light propagates in the multi-mode inner cladding and provides cooling power. Details of the fiber parameters are provided in Table 6.3

Table 6.3: Fiber parameters.

Parameter	Core	Inner cladding	Outer cladding
Radius (μm)	1	62.5	100
Refractive index (real)	1.52	1.47	1.45
Refractive index (imaginary)	3.88e-8	4.06e-9	1e-9
Guided wavelength (μm)	1.04, 1.06	1.04	N.A.
Thermal conductivity	1.7 W/(m K)		

Due to the large inner cladding size, more than a hundred optical modes are

allowed. However, three dominant modes contribute to more than 99% of the total intensity. The are HE11, HE13, and HE15 modes. The sum of the three modes has a nearly Gaussian profile, simplifying analytical calculations. The lasing signal is confined in the core. Figure 6.9b and Figure 6.9c show the radial distributions of the pump light in the cladding and the lasing signal in the core. The maximum lasing irradiation is 4.4 kW/cm^2 and the maximum pump irradiance is 9.6W/cm^2.

The signal at 1060 nm wavelength and pump at 1040 nm are guided simultaneously in a fiber amplifier. The signal propagates in the single-mode core, amplified by the pump. Heat is generated because of the quantum defects and parasitic background absorption. The heat power can be defined as $P_{heating} = P_0 \alpha \eta_{heating}$, where α is the absorption coefficient, $\eta_{heating}$ is the Heating efficiency

$$\eta_{heating} = 1 - \eta_{eqe}\eta_{abs}\frac{\lambda_p}{\lambda_s}, \tag{6.26}$$

Here η_{eqe}, η_{abs} are the external quantum efficiency and the resonant absorption efficiency of the core glass. The 1040 nm pump is coupled into the inner cladding. Part of the pump is absorbed by the core material and amplifies the signal, which generates heat. The rest is absorbed by the cooling-grade inner cladding and extracts heat by anti-Stokes cooling. The cooling efficiency is defined similarly as the heating efficiency

$$\eta_{cooling} = \eta_{eqe}\eta_{abs}\frac{\lambda_p}{\lambda_s} - 1, \tag{6.27}$$

The η_{eqe} and η_{abs} of the inner cladding must be near unity to achieve cooling, which requires high quality of the materials.

The volumetric rate of heat generated inside the fiber (S), as a function of the

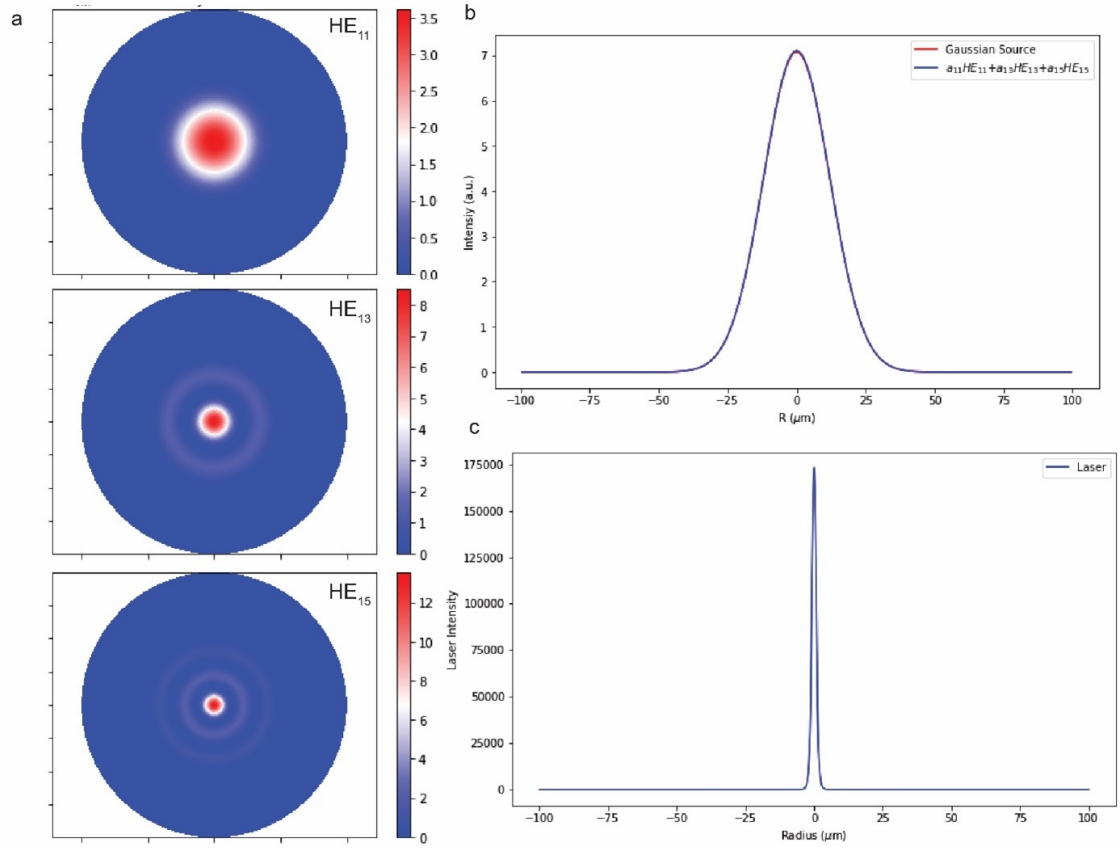

Figure 6.9: (a) Three dominant modes HE11, HE13, and HE15. (b) Intensify profiles of the Gaussian pump source and three dominant modes. When the pump beam size is 40% of the inner cladding size, the sum of the three most intensive guided modes HE11, HE13, and HE15 has a nearly Gaussian profile. (c) The radial intensity profile of the lasing signal at 1060 nm wavelength.

coordinates is expressed as

$$S(r,\phi,z) = \frac{1}{2}\sigma_i(E \cdot E^*), \tag{6.28}$$

where E is the internal electric-field amplitude vector, which could be derived by solving the Maxwell's equations with boundary conditions of the proposed fiber. E^* is its complex conjugate of the electric field and σ_i is the effective conductivity of the fiber core or cladding materials, which is given by

$$\sigma_i = \frac{4\pi Re\{N_i\}Im\{N_i\}}{\lambda\mu c}, \tag{6.29}$$

in which $N_i = n_i + ik_i$ is the complex refractive index of the fiber core or cladding, where $n_i = Re\{N_i\}$ and $k_i = Im\{N_i\}$, λ is the wavelength of the free space, μ is the magnetic permeability, and c is the velocity of light in vacuum.

Therefore, the heating source in the core is induced by both the amplified signal propagating inside the core and a portion of the pump in the core

$$S_{co}(r,\phi,z) = \frac{2\pi Re\{N_{co}\}Im\{N_{co}\}}{\lambda_s\mu c}(E_s \cdot E_s^*)\eta^s_{heating} + \frac{2\pi Re\{N_{co}\}Im\{N_{co}\}}{\lambda_p\mu c}(E_p \cdot E_p^*)\eta^p_{heating}. \tag{6.30}$$

The cooling source of the cladding is generated by the evanescent field of the signal in the cladding and the majority of the pump light in the inner cladding. The cooling source in the cladding is given by

$$S_{cl}(r,\phi,z) = -\frac{2\pi Re\{N_{cl}\}Im\{N_{cl}\}}{\lambda_s\mu c}(E_s \cdot E_s^*)\eta^s_{cooling} - \frac{2\pi Re\{N_{cl}\}Im\{N_{cl}\}}{\lambda_p\mu c}(E_p \cdot E_p^*)\eta^p_{cooling}. \tag{6.31}$$

The volumetric electromagnetic sources in the core and cladding are plotted in

Figure 6.10. Although there is some pump amplitude in the core, the intensity is very weak compared to the amplified lasing signal. Any cooling/heating effects caused by the pump light are negligible compared to the lasing signal-induced heat. In this design, the heating induced by the evanescent field is much less than that in the core because of the low Yb concentration in the cladding. The evanescent field from the lasing mode can only reach a shallow layer of the inner cladding.

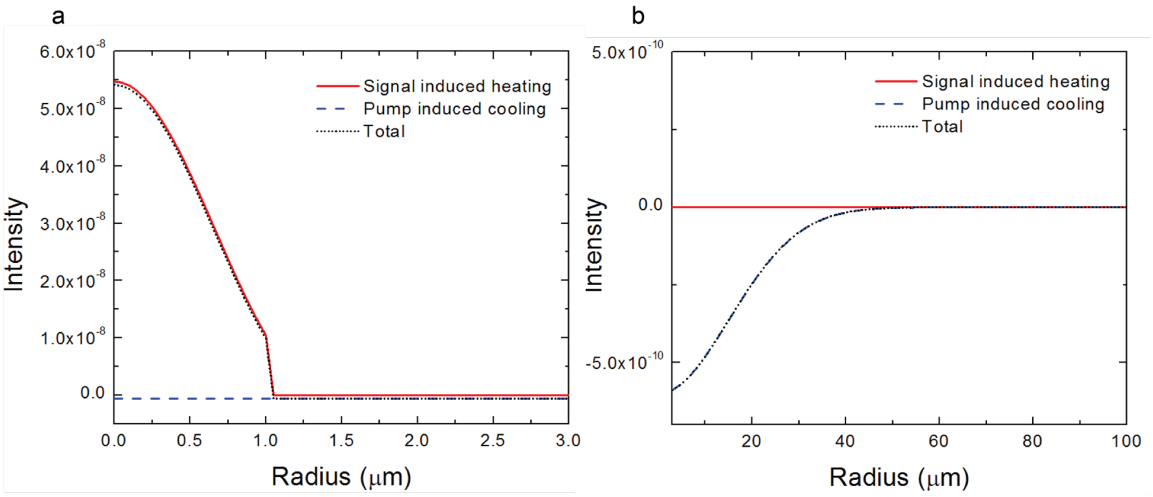

Figure 6.10: Radial distributions of the volumetric electromagnetic source in the core (a) and the cladding (b).

The volumetric electromagnetic source in the inner cladding is dominated by the cooling power induced by the pump at 1040 nm. Although the volumetric cooling power in the cladding is very weak compared to the heat power in the core, the total cooling power is considerable because of the large inner cladding size. The radial and axial steady-state temperatures are presented in Figure 6.11. To achieve radiation-balanced lasing, parameters such as fiber geometry, material refractive indices, pump powers need to be studied and selected carefully to maintain the operating temperature.

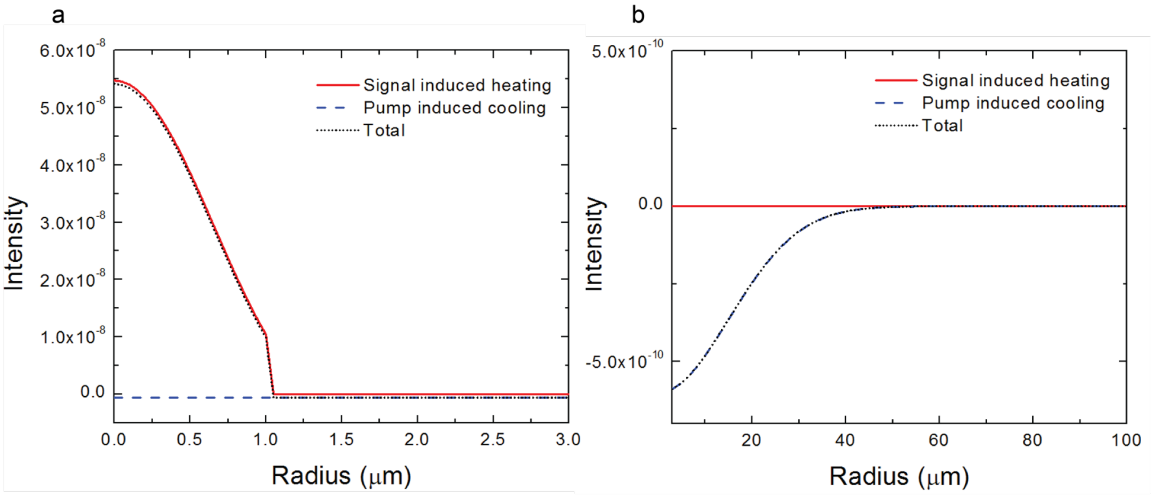

Figure 6.11: Radial (a) and axial (b) temperature distribution of the fiber at the steady state..

6.7 Conclusions

Two radiation balanced fiber laser designs are explored: a single-mode core-pumped fiber laser and a multi-mode clad pumped fiber laser. Both lasers can be cooled through anti-Stokes photoluminescence generated within the fiber's first cladding layer. In the first design, the cladding material is a composite with Yb:YLF nanocrystals dispersed within the glass host matrix. Experimental proof of the principle of fiber cooling is demonstrated using far-field excitation of a YLF/polymer composite cladding material. Cooling grade Yb-doped silica glass is used in the second design. The heat diffusion equation was solved analytically for both the core and cladding based on the assumption that they have identical thermal conductivities.

The first model shows a significant temperature decrease of 19 K when the Yb:YLF nanocrystals within the composite cladding have a volume fraction of 10%. The reduced heating of the fiber suggests that pumping the entire cladding may lead to

further reductions in temperature.

In this core-pumped design, the evanescent field from the core is the sole source of laser cooling. The temperature decrease is limited to the low power fraction of the evanescent field compared to the power inside the core, implying that pumping through the cladding can lead to even more cooling. This model has been extended to multi-mode clad-pumped fiber-lasers, which have much more power in the cladding.

In the second design, the pump coupled into the inner cladding amplifies the signal propagating inside the core and lowers the temperature of the entire fiber. In our design, the inner cladding material is cooling-grade ytterbium-doped silica glass. In addition, analytical models of heat transfer within the fiber were studied. This model shows a significant temperature decrease of the double-clad fiber amplifier due to anti-Stokes cooling of the inner cladding.

Chapter 7

CLOSING REMARKS AND CONCLUSIONS

7.1 Summary of results

For the last five years in the Pauzauskie lab, I have been focusing on developing and characterizing RE doped fluoride nanocrystals for laser cooling and their applications to radiation-balanced lasers. A low-cost, scalable, and environmentally friendly hydrothermal method has been investigated extensively to yield a final recipe for synthesizing high-quality fluoride nanocrystals in different phases, sizes, morphologies, and dopant concentrations. The hydrothermal growth mechanism has also been revealed a little bit in the thesis, which can help obtain complex structures of fluoride nanocrystals to meet requirements for future laser cooling or upconversion applications. A variety of non-contact thermometries were used to detect the temperature of synthesized materials in different size scales. For example, mean fluorescen wavelength and cold Brownian motion analyses. Laser cooling of Yb^{3+} doped KLF nanocrystals phase has been for the first time. Furthermore, point defects in fluoride materials are studied as a possible source that deteriorates the cooling performance. Optically generating local refrigeration fields around individual nanocrystals holds promises for applications in radiation-balanced laser devices. In addition, a YLF-polymer composite cladding is proposed in a single-mode core-pumped fiber laser design. The light propagation and heat transfer are modeled. This design is further updated to an all-glass multi-mode fiber laser which provides higher cooling power via clad pumping. In addition to laser cooling, the upconversion Er^{3+} ratiometric thermometry are revised to avoid the power-dependent green emission that lowers the accuracy.

7.2 Future directions

Cooling was not observed in two KLF crystallographic phases, KLu_3F_{10} and KLu_2F_7, due to the high surface-to-volume ratios. The laser cooling efficiency of nanocrystals can be further enhanced by minimizing the surface quenching. Multiphonon relaxation can happen through interaction with phonons in the host lattice and through interaction with molecular groups that are attached toto the surface of the host materials and surface defects.[150] The energy migration between different active ions may transport excited state energy to the surface, which causes heating of the surface. In order to minimize the energy transfer between internal active ions to surface-active ions, the RE ion-doped nanocrystal can be coated with non-dopant host materials. This will insulate the internal active ions transport energy outside.

Such core-shell structure has been adapted to sub 10 nm size Yb:$NaYF_4$ nanoparticles. A $NaGdF_4$ shell is coated onto the Yb:$NaYF_4$ core to improve the quantum efficiency[151]. A radiation balanced microsphere laser has been proposed based on coating the surface of the microspheres using upconverting nanoparticles and laser refrigeration nanoparticles with such core-shell structure. In this design, surface whispering gallery modes will enable lasing and cooling via the nanoparticles on the surface. In contrast with the first design, the second design is based on incorporating laser refrigeration nanoparticles throughout the entire volume of the microsphere, rather than just the surface. In this design, cooling will be pursued throughout the entire volume of the composite microsphere in off-resonant conditions. Recently, lasing of microspheres coated with Tm-doped $NaYF_4$ nanoparticles and cooling of microspheres coated with Yb-doped $NaYF_4$ nanoparticles have been achieved separately in the Pauzauskie lab. To realize radiation-balanced lasing, the two types of nanoparticles can be coated to the same microsphere and pumped with different wavelengths. A more sophisticated model is required with lanthanides energy levels engineered to

achieve lasing and cooling simultaneously. Recently, optical cooling has been proposed in CdS/CdSe core-shell quantum dots with phonon-assisted upconversion[152]. Synthesis of high EQE CdS/CdSe QDs is one of the ongoing projects in the Pauzauskie lab.

The radiation balanced fiber laser design has been discussed a lot in Chapter 6. A cooling grade silica glass preform is available in the Pauzauskie lab (borrowed from Mafi's group at the University of New Mexico). However, the temperature change is limited to 0.1K/W. Sub 100mK resolution is required. Optically detected magnetic resonance is such method that can measure temperatures reliably. Nanodiamonds with NV^- centers can be coated to the surface of the fiber preform. The emission spectrum from the center ranges from the ZPL at 638 nm, out to 800 nm through phonon broadened transitions between the ground state ($^3A_2$) and excited state (^3E) triplets. Readout of the spin state within the ground state triplet can be performed optically using the spin-selective inter-system crossing between the NV^- excited state triplet and a pair of singlet states ($^1A_1$ and ^1E). Decay through the inter-system crossing is nonradiative and preferentially repopulates the $m_s = 0$ ground state spin sublevel. Since the non-radiative decay is stronger from $m_s = \pm 1$ than $m_s = 0$, a reduction in the emitted PL results if the NV^- spin has been prepared in $m_s = \pm 1$ using MW radiation prior to excitation above the ZPL.

BIBLIOGRAPHY

[1] M Sheik-Bahae and R Epstein. *Optical Refrigeration: Science and Applications of Laser Cooling of Solids*. Wiley-VCH, Weinheim, Germany, 2009.

[2] Peter Pringsheim. Two observations about the difference between luminescence and thermal radiation. *Z. Phys*, 57:739–746, 1929.

[3] Richard I. Epstein, Melvin I. Buchwald, Bradley C. Edwards, Timothy R. Gosnell, and Carl E. Mungan. Observation of laser-induced fluorescent cooling of a solid. *Nature*, 377(6549):500–503, 1995.

[4] J Fernandez, A Mendioroz, AJ Garcia, R Balda, and JL Adam. Anti-stokes laser-induced internal cooling of yb 3+-doped glasses. *Phys. Rev. B*, 62(5):3213, 2000.

[5] J. Thiede, J. Distel, S. R. Greenfield, and R. I. Epstein. Cooling to 208K by optical refrigeration. *Appl. Phys. Lett.*, 86(15):154107, 2005.

[6] Seth D. Melgaard, Alexander R. Albrecht, Markus P. Hehlen, and Mansoor Sheik-Bahae. Solid-state optical refrigeration to sub-100 Kelvin regime. *Scientific Reports*, 6(1):20380, apr 2016.

[7] R. I. Epstein, J. J. Brown, B. C. Edwards, and A. Gibbs. Measurements of optical refrigeration in ytterbium-doped crystals. *J. Appl. Phys.*, 90(9):4815–4819, 2001.

[8] A. Mendioroz, J. Fernández, M. Voda, M. Al-Saleh, R. Balda, and A. J. García-Adeva. Anti-Stokes laser cooling in Yb^3+-doped KPb_2Cl_5 crystal. *Opt. Lett.*, 27(17):1525, 2002.

[9] Stefano Bigotta, Daniela Parisi, Lucia Bonelli, Alessandra Toncelli, Mauro Tonelli, and Alberto Di Lieto. Spectroscopic and laser cooling results on Yb3+-doped BaY2F8 single crystal. *J. Appl. Phys.*, 100(1):013109, 2006.

[10] Biao Zhong, Jigang Yin, Youhua Jia, Lin Chen, Yin Hang, and Jianping Yin. Laser cooling of Ybˆ3+-doped LuLiF_4 crystal. *Opt. Lett.*, 39(9):2747, 2014.

[11] A. Volpi, G. Cittadino, A. Di Lieto, and M. Tonelli. AntiStokes cooling of Yb-doped KYF4 single crystals. *Journal of Luminescence*, 203:670–675, 2018.

[12] Paden B Roder, Bennett E Smith, Xuezhe Zhou, Matthew J Crane, and Peter J Pauzauskie. Laser refrigeration of hydrothermal nanocrystals in physiological media. *Proc. Natl. Acad. Sci.*, 112(49):15024–15029, 2015.

[13] A. Einstein. Über die von der molekularkinetischen theorie der wärme geforderte bewegung von in ruhenden flüssigkeiten suspendierten teilchen. *Ann. Physk*, 322(8):549–560, 1905.

[14] Markus P. Hehlen, Junwei Meng, Alexander R. Albrecht, Eric R. Lee, Aram Gragossian, Steven P. Love, Christopher E. Hamilton, Richard I. Epstein, and Mansoor Sheik-Bahae. First demonstration of an all-solid-state optical cryocooler. *Light: Sci. Appl.*, 7(1):15, 2018.

[15] Steven R Bowman and Carl E Mungan. Selecting Materials for Radiation Balanced Lasers. Technical report.

[16] Thomas Kessler, Christian Hagemann, C Grebing, T Legero, Uwe Sterr, Fritz Riehle, MJ Martin, L Chen, and J Ye. A sub-40-mhz-linewidth laser based on a silicon single-crystal optical cavity. *Nature Photonics*, 6(10):687, 2012.

[17] Xuezhe Zhou, Bennett E. Smith, Paden B. Roder, and Peter J. Pauzauskie. Laser Refrigeration of Ytterbium-Doped Sodium-Yttrium-Fluoride Nanowires. *Adv. Mater.*, 28(39):8658–8662, 2016.

[18] Galina Nemova and Raman Kashyap. Laser cooling of solids: latest achievements and prospects. In *Optical and Electronic Cooling of Solids III*, volume 10550, page 1055005. International Society for Optics and Photonics, 2018.

[19] L Landau. On the thermodynamics of photoluminescence. *J. Phys.(Moscow)*, 10(503), 1946.

[20] M. Sheik-Bahae and R.I. Epstein. Laser cooling of solids. *Laser Photonics Rev.*, 3(1-2):67–84, 2009.

[21] Denis V Seletskiy, Richard Epstein, and Mansoor Sheik-Bahae. Laser cooling in solids: advances and prospects. *Rep. Prog. Phys.*, 79(9):096401, 2016.

[22] Mansoor Sheik-Bahae and Richard I. Epstein. Optical refrigeration. *Nat. Photonics*, 1(12):693–699, 2007.

[23] Denis V. Seletskiy, Seth D. Melgaard, Richard I. Epstein, Alberto Di Lieto, Mauro Tonelli, and Mansoor Sheik-Bahae. Local laser cooling of Yb:YLF to 110 K. *Optics Express*, 19(19):18229–18236, 2011.

[24] Aram Gragossian, Azzurra Volpi, Junwei Meng, Alexander R Albrecht, Saeid Rostami, Markus P Hehlen, and Mansoor Sheik-Bahae. Investigation of temperature dependence of quantum efficiency and parasitic absorption in rare-earth doped crystals (conference presentation). In *Optical and Electronic Cooling of Solids III*, volume 10550, page 1055006. International Society for Optics and Photonics, 2018.

[25] Azzurra Volpi, Junwei Meng, Aram Gragossian, Alexander R Albrecht, Saeid Rostami, Alberto Di Lieto, Richard I Epstein, Mauro Tonelli, Markus P Hehlen, and Mansoor Sheik-Bahae. Optical refrigeration: the role of parasitic absorption at cryogenic temperatures. *Opt. Express*, 27(21):29710–29718, 2019.

[26] Jacob B Khurgin. Role of bandtail states in laser cooling of semiconductors.

[27] Alfred Kastler. Quelques suggestions concernant la production optique et la détection optique d'une inégalité de population des niveaux de quantifigation spatiale des atomes. Application à l'expérience de Stern et Gerlach et à la résonance magnétique. *J. Phys. Radium*, 11(6):255–265, 1950.

[28] Joaquin Fernandez, Angel J Garcia-Adeva, and Rolindes Balda. Anti-stokes laser cooling in bulk erbium-doped materials. *Phys. Rev. Lett.*, 97(3):033001, 2006.

[29] L. A. Riseberg and H. W. Moos. Multiphonon orbit-lattice relaxation of excited states of rare-earth ions in crystals. *Phys. Rev.*, 174(2):429–438, 1968.

[30] S.R. Bowman, S. O'Connor, and S. Biswal. Radiation balanced lasers. In *Proceedings of IEEE Conference on Lasers and Electro-Optics Europe, 2005.*, pages 35–35. IEEE.

[31] Zhou Yang, Junwei Meng, Alexander R. Albrecht, and Mansoor Sheik-Bahae. Radiation-balanced Yb:YAG disk laser. *Optics Express*, 27(2):1392, 2019.

[32] S. R. Bowman, S. P. O'Connor, S. Biswal, N. J. Condon, and A. Rosenberg. Minimizing heat generation in solid-state lasers. *IEEE Journal of Quantum Electronics*, 46(7):1076–1085, 2010.

[33] Mostafa Peysokhan, Esmaeil Mobini, Arman Allahverdi, Behnam Abaie, and Arash Mafi. Laser Cooling Characterization of Yb-Doped ZBLAN Fiber as a Platform for Radiation Balanced Lasers. Technical report.

[34] Esmaeil Mobini, Saeid Rostami, Mostafa Peysokhan, Alexander Albrecht, Stefan Kuhn, Sigrun Hein, Christian Hupel, Johannes Nold, Nicoletta Haarlammert, Thomas Schreiber, et al. Laser cooling of silica glass. *arXiv preprint arXiv:1910.10609*, 2019.

[35] Jennifer Knall, Pierre-Baptiste Vigneron, Magnus Engholm, Peter D. Dragic, Nanjie Yu, John Ballato, Martin Bernier, and Michel J. F. Digonnet. Laser cooling in a silica optical fiber at atmospheric pressure. *Optics Letters*, 45(5):1092, 2020.

[36] Jennifer M Knall, Mina Esmaeelpour, and MJF Digonnet. Model of anti-stokes fluorescence cooling in a single-mode optical fiber. *Journal of Lightwave Technology*, 36(20):4752–4760, 2018.

[37] Esmaeil Mobini, Mostafa Peysokhan, Behnam Abaie, and Arash Mafi. Thermal modeling, heat mitigation, and radiative cooling for double-clad fiber amplifiers. *Journal of the Optical Society of America B*, 35(10):2484–2493, 2018.

[38] Seth D Melgaard, Alexander R Albrecht, Markus P Hehlen, and Mansoor Sheik-Bahae. Solid-state optical refrigeration to sub-100 kelvin regime. *Sci. Rep.*, 6:20380, 2016.

[39] ATM Anishur Rahman and PF Barker. Laser refrigeration, alignment and rotation of levitated Yb^{3+}: YLF nanocrystals. *Nat. Photonics*, 11(10):634–638, 2017.

[40] WM Patterson, DV Seletskiy, M Sheik-Bahae, RI Epstein, and MP Hehlen. Measurement of solid-state optical refrigeration by two-band differential luminescence thermometry. *JOSA B*, 27(3):611–618, 2010.

[41] X. Liang, X. Wang, J. Zhuang, Q. Peng, and Y. Li. Synthesis of $NaYF_4$ nanocrystals with predictable phase and shape. *Adv. Funct. Mater.*, 17(15):2757–2765, 2007.

[42] Fiorenzo Vetrone, Rafik Naccache, Angeles Juarranz de la Fuente, Francisco Sanz-Rodriguez, Alfonso Blazquez-Castro, Emma Martin Rodriguez, Daniel Jaque, Jose Garcia Sole, and John A. Capobianco. Intracellular imaging of HeLa cells by non-functionalized $NaYF_4 : Er^{3+}$, Yb^{3+} upconverting nanoparticles. *Nanoscale*, 2(4):495–498, 2010.

[43] Lorenz H. Fischer, Gregory S. Harms, and Otto S. Wolfbeis. Upconverting nanoparticles for nanoscale thermometry. *Angew. Chem.-Int. Edit.*, 50(20):4546–4551, 2011.

[44] Emily J. McLaurin, Liam R. Bradshaw, and Daniel R. Gamelin. Dual-emitting nanoscale temperature sensors. *Chem. Mater.*, 25(8):1283–1292, 2013.

[45] Paden B. Roder, Sandeep Manandhar, Bennett E. Smith, Xuezhe Zhou, Vaithiyalingam S. Shutthanandan, and Peter J. Pauzauskie. Photothermal superheating of water with ion-implanted silicon nanowires. *Adv. Opt. Mater*, 3(10):1362–1367, 2015.

[46] Dejgj Dolmans, D. Fukumura, and R. K. Jain. Photodynamic therapy for cancer. *Nat. Rev. Cancer*, 3(5):380–387, 2003.

[47] Kirstine Berg-Sørensen and Henrik Flyvbjerg. Power spectrum analysis for optical tweezers. *Rev. Sci. Instrum*, 75(3):594–612, 2004.

[48] D. Chakraborty, M. V. Gnann, D. Rings, J. Glaser, F. Otto, F. Cichos, and K. Kroy. Generalised einstein relation for hot brownian motion. *EPL (Europhysics Letters)*, 96(6):60009, 2011.

[49] Daniel Rings, Markus Selmke, Frank Cichos, and Klaus Kroy. Theory of hot brownian motion. *Soft Matter*, 7(7):3441–3452, 2011.

[50] Ruri Hidema, Zenji Yatabe, Hikari Takahashi, Ryusei Higashikawa, and Hiroshi Suzuki. Inverse integral transformation method to derive local viscosity distribution measured by optical tweezers. *Soft Matter*, 16(29):6826–6833, aug 2020.

[51] Bennett E Smith. *Thermochemical dynamics of laser-irradiated semiconductor nanostructures*. PhD thesis, University of Washington Libraries, 2016.

[52] R Sandberg, W Svendsen, Kristian Mølhave, and Anja Boisen. Temperature and pressure dependence of resonance in multi-layer microcantilevers. *J. Micromech. Microeng.*, 15(8):1454–1458, 2005.

[53] Anupum Pant. *Laser Heating, Refrigeration, and Thermometry of Semiconductor Nanomaterials*. University of Washington, 2020.

[54] Carlos D.S. Brites, Sangeetha Balabhadra, and Luís D Carlos. Lanthanide-Based Thermometers: At the Cutting-Edge of Luminescence Thermometry, 2019.

[55] Susil Baral, Samuel C Johnson, Arwa A Alaulamie, and Hugh H Richardson. Nanothermometry using optically trapped erbium oxide nanoparticle. *Applied Physics A*, 122(4):340, 2016.

[56] Emily J McLaurin, Liam R Bradshaw, and Daniel R Gamelin. Dual-emitting nanoscale temperature sensors. *Chemistry of Materials*, 25(8):1283–1292, 2013.

[57] Fiorenzo Vetrone, Rafik Naccache, Alicia Zamarrón, Angeles Juarranz de la Fuente, Francisco Sanz-Rodríguez, Laura Martinez Maestro, Emma Martin Rodriguez, Daniel Jaque, Jose Garcia Sole, and John A Capobianco. Temperature sensing using fluorescent nanothermometers. *ACS Nano*, 4(6):3254–3258, 2010.

[58] SF Collins, GW Baxter, SA Wade, T Sun, KTV Grattan, ZY Zhang, and AW Palmer. Comparison of fluorescence-based temperature sensor schemes: theoretical analysis and experimental validation. *Journal of Applied Physics*, 84(9):4649–4654, 1998.

[59] Jiajia Zhou, Blanca Del Rosal, Daniel Jaque, Seiichi Uchiyama, and Dayong Jin. Advances and challenges for fluorescence nanothermometry. *Nature methods*, pages 1–14, 2020.

[60] Mochen Jia, Guofeng Liu, Zhen Sun, Zuoling Fu, and Weiguo Xu. Investigation on two forms of temperature-sensing parameters for fluorescence intensity ratio thermometry based on thermal coupled theory. *Inorganic Chemistry*, 57(3):1213–1219, 2018.

[61] Scott A Wade, Stephen F Collins, and Gregory W Baxter. Fluorescence intensity ratio technique for optical fiber point temperature sensing. *Journal of Applied Physics*, 94(8):4743–4756, 2003.

[62] AH Khalid and K Kontis. 2d surface thermal imaging using rise-time analysis from laser-induced luminescence phosphor thermometry. *Measurement Science and Technology*, 20(2):025305, 2009.

[63] H Berthou and CK Jörgensen. Optical-fiber temperature sensor based on upconversion-excited fluorescence. *Optics Letters*, 15(19):1100–1102, 1990.

[64] A Siaï, P Haro-González, K Horchani Naifer, and M Férid. Optical temperature sensing of Er^{3+}/Yb^{3+} doped $LaGdO_3$ based on fluorescence intensity ratio and lifetime thermometry. *Optical Materials*, 76:34–41, 2018.

[65] Yan Ma, Guotao Xiang, Jiahua Zhang, Zhen Liu, Pan Zhou, Wen Liu, Xiao Tang, Sha Jiang, Xianju Zhou, Li Li, et al. Upconversion properties and temperature sensing behaviors in visible and near-infrared region based on fluorescence intensity ratio in $LuVO_4$:Yb^{3+}/Er^{3+}. *Journal of Alloys and Compounds*, 769:325–331, 2018.

[66] Marta Quintanilla, Eugenio Cantelar, Fernando Cusso, Marina Villegas, and Amador C Caballero. Temperature sensing with up-converting submicron-sized $LiNbO_3$: Er^{3+}/Yb^{3+} particles. *Applied Physics Express*, 4(2):022601, 2011.

[67] PV Dos Santos, MT De Araujo, AS Gouveia-Neto, JA Medeiros Neto, and ASB Sombra. Optical temperature sensing using upconversion fluorescence emission in Er^{3+}/Yb^{3+}-codoped chalcogenide glass. *Applied Physics Letters*, 73(5):578–580, 1998.

[68] Antonio C Brandão-Silva, Maria A Gomes, Suellen MV Novais, Zélia S Macedo, Jhon FM Avila, JJ Rodrigues Jr, and MARC Alencar. Size influence on temperature sensing of erbium-doped yttrium oxide nanocrystals exploiting thermally coupled and uncoupled levels' pairs. *Journal of Alloys and Compounds*, 731:478–488, 2018.

[69] X Mateos, R Solé, Jna Gavaldà, M Aguiló, F Díaz, and J Massons. Ultraviolet and visible emissions of Er^{3+} in KY $(WO_4)_2$ single crystals co-doped with Yb^{3+} ions. *Journal of Luminescence*, 115(3-4):131–137, 2005.

[70] Shaoshuai Zhou, Kaimo Deng, Xiantao Wei, Guicheng Jiang, Changkui Duan, Yonghu Chen, and Min Yin. Upconversion luminescence of $NaYF_4$:Yb^{3+}, Er^{3+} for temperature sensing. *Optics Communications*, 291:138–142, 2013.

[71] C Renero-Lecuna, R Martín-Rodríguez, R Valiente, J González, F Rodríguez, KW Kramer, and HU Gudel. Origin of the high upconversion green luminescence efficiency in β-$NaYF_4$: 2% Er^{3+}, 20% Yb^{3+}. *Chemistry of Materials*, 23(15):3442–3448, 2011.

[72] Xiaojing Xia, Anupum Pant, Xuezhe Zhou, Elena Dobretsova, Alex Bard, Matthew Lim, Joo Yeon Roh, Daniel R. Gamelin, and Peter Pauzauskie. Hydrothermal Synthesis and Solid-State Laser Refrigeration of Ytterbium-Doped Potassium Lutetium Fluoride (KLF) Microcrystals. *ChemRxiv*, 5 2020.

[73] Ying Cui, Longjiang Zheng, Wei Xu, Hailong Liu, Leipeng Li, and Zhiguo Zhang. Influence of 980 nm pump power on optical thermometry based on $NaYF_4$:Yb^{3+}/Er^{3+} nanoparticles. *Materials Research Express*, 5(6):065018, 2018.

[74] Denis V Seletskiy, Richard Epstein, and Mansoor Sheik-Bahae. Laser cooling in solids: advances and prospects. *Reports on Progress in Physics*, 79(9):096401, 2016.

[75] Xiaojing Xia, Anupum Pant, Abbie S Ganas, Fedor Jelezko, and Peter J Pauzauskie. Quantum point defects for solid-state laser refrigeration. *Advanced Materials*, page 1905406, 2020.

[76] JF Suyver, J Grimm, KW Krämer, and Hans-Ulrich Güdel. Highly efficient near-infrared to visible up-conversion process in $NaYF_4$:Er^{3+}, Yb^{3+}. *Journal of Luminescence*, 114(1):53–59, 2005.

[77] Markus Pollnau, Daniel R Gamelin, SR Lüthi, HU Güdel, and Markus P Hehlen. Power dependence of upconversion luminescence in lanthanide and transition-metal-ion systems. *Physical Review B*, 61(5):3337, 2000.

[78] Mary T Berry and P Stanley May. Disputed mechanism for NIR-to-red upconversion luminescence in $NaYF_4$: Yb^{3+}/Er^{3+}. *The Journal of Physical Chemistry A*, 119(38):9805–9811, 2015.

[79] Vesna M Lojpur, Phillip S Ahrenkiel, and Miroslav D Dramićanin. Color-tunable up-conversion emission in Y_2O_3:Yb^{3+}, Er^{3+} nanoparticles prepared by polymer complex solution method. *Nanoscale Research Letters*, 8(1):131, 2013.

[80] M Yuan, R Wang, C Zhang, Z Yang, W Cui, X Yang, N Xiao, H Wang, and X Xu. Exploiting the silent upconversion emissions from a single β-$NaYF_4$:yb/Er microcrystal via saturated excitation. *Journal of Materials Chemistry C*, 6(38):10226–10232, 2018.

[81] Guokui Liu. Advances in the theoretical understanding of photon upconversion in rare-earth activated nanophosphors. *Chemical Society Reviews*, 44(6):1635–1652, 2015.

[82] Hao Wu, Zhengdong Hao, Liangliang Zhang, Xia Zhang, Yu Xiao, Guo-Hui Pan, Huajun Wu, Yongshi Luo, Haifeng Zhao, and Jiahua Zhang. Phonon energy dependent energy transfer upconversion for the red emission in the Er^{3+}/Yb^{3+} system. *The Journal of Physical Chemistry C*, 122(17):9611–9618, 2018.

[83] Juan Wang, Renren Deng, Mark A MacDonald, Bolei Chen, Jikang Yuan, Feng Wang, Dongzhi Chi, Tzi Sum Andy Hor, Peng Zhang, Guokui Liu, et al. Enhancing multiphoton upconversion through energy clustering at sublattice level. *Nature Materials*, 13(2):157–162, 2014.

[84] GA Bukhalova, EP Bahaeva, and Khliyan TM. No Title. *Zh. Neorg. Khim*, 10:2127—-2131, 1965.

[85] E.M. Levin and H.F. McMurdie. Phase diagrams for ceramists, 1975 supplement, 1975.

[86] Bruce H. T. Chai, J. Lefaucheur, Anh-Tuyet Pham, G. B. Loutts, and John F. Nicholls. Growth of high-quality single crystals of KYF4 by TSSG method</title>. volume 1863, pages 131–135. International Society for Optics and Photonics, 1993.

[87] Azzurra Volpi, Junwei Meng, Alexander R. Albrecht, Mansoor Sheik-Bahae, Daniel Biner, Karl W. Krämer, and Markus P. Hehlen. Bridgman growth of LiYF4 and LiLuF4 crystals for radiation-balanced lasers. (May):24, 2019.

[88] Y.Q. Jia. Crystal radii and effective ionic radii of the rare earth ions. *Journal of Solid State Chemistry*, 95(1):184–187, 1991.

[89] Mingye Ding, Fei Zhu, Danyang Ma, Xiaoyong Huang, Peng Liu, Kaixin Song, Jiasong Zhong, Junhua Xi, Zhenguo Ji, and Daqin Chen. KF-mediated controlled-synthesis of potassium ytterbium fluorides (doped with er $^{3+}$) with phase-dependent upconversion luminescence. *CrystEngComm*, 17(37):7182–7190, 2015.

[90] M. Karbowiak, P. Gnutek, and C. Rudowicz. Energy levels and crystal field parameters for Nd3+ ions in BaY2F8, LiKYF5, and K2YF5 single crystals. *Spectrochimica Acta Part A: Molecular and Biomolecular Spectroscopy*, 87:46–60, 2012.

[91] Brian Henderson and Ralph H. Bartram. *Crystal-Field Engineering of Solid-State Laser Materials*. Cambridge University Press, Cambridge, 2000.

[92] Xuezhe Zhou, Xiaojing Xia, Bennett E. Smith, Matthew B. Lim, Alexander B. Bard, Anupum Pant, and Peter J. Pauzauskie. Interface-Dependent Radiative Lifetimes of Yb ³⁺ , Er ³⁺ Co-doped Single NaYF ₄ Upconversion Nanowires. *ACS Applied Materials & Interfaces*, 11(25):22817–22823, 2019.

[93] M Eichhorn. Fluorescence reabsorption and its effects on the local effective excitation lifetime. *Appl Phys B*, 96:369–377, 2009.

[94] Sujata Saha, Saha Chowdhury, and Amitava Patra. Luminescence of Ce 3+ in Y 2 SiO 5 Nanocrystals: Role of Crystal Structure and Crystal Size. 2005.

[95] Xiaojie Xue, Shinya Uechi, Rajanish N. Tiwari, Zhongchao Duan, Meisong Liao, Masamichi Yoshimura, Takenobu Suzuki, and Yasutake Ohishi. Size-dependent upconversion luminescence and quenching mechanism of LiYF_4: Erˆ3+/Ybˆ3+ nanocrystals with oleate ligand adsorbed. *Optical Materials Express*, 3(7):989, 2013.

[96] D. S. Sumida and T. Y. Fan. Effect of radiation trapping on fluorescence lifetime and emission cross section measurements in solid-state laser media. *Optics Letters*, 19(17):1343, 1994.

[97] Anupum Pant, Bennett E. Smith, Matthew J. Crane, Xuezhe Zhou, Matthew B. Lim, Stuart A. Frazier, E. James Davis, and Peter J. Pauzauskie. Optomechanical Thermometry of Nanoribbon Cantilevers. *The Journal of Physical Chemistry C*, 122(13):7525–7532, 2018.

[98] Paden B Roder, Bennett E Smith, Xuezhe Zhou, Matthew J Crane, and Peter J Pauzauskie. Laser refrigeration of hydrothermal nanocrystals in physiological media. *Proc. Natl. Acad. Sci. U. S. A.*, 112(49):15024–15029, 2015.

[99] Xun Wang and Yadong Li. Synthesis and Characterization of Lanthanide Hydroxide Single-Crystal Nanowires. *Angewandte Chemie International Edition*, 41(24):4790–4793, 2002.

[100] Xing Wang, Hongliang Zhang, Tomonori Baba, Hao Jiang, Cheng Liu, Yingxin Guan, Omar Elleuch, Thomas Kuech, Dane Morgan, Juan-Carlos Idrobo, et al. Radiation-induced segregation in a ceramic. *Nature Materials*, 19(9):992–998, 2020.

[101] Sylvain Girard, Antonino Alessi, Nicolas Richard, Layla Martin-Samos, Vincenzo De Michele, Luigi Giacomazzi, Simonpietro Agnello, Diego Di Francesca, Adriana Morana, Blaž Winkler, et al. Overview of radiation induced point defects in silica-based optical fibers. *Reviews in Physics*, 4:100032, 2019.

[102] Chinthaka M Silva, Thomas M Rosseel, and Marie C Kirkegaard. Radiation-induced changes in quartz, a mineral analog of nuclear power plant concrete aggregates. *Inorganic Chemistry*, 57(6):3329–3338, 2018.

[103] Giuseppe Baldacchini. Colored LiF: an optical material for all seasons. *Journal of Luminescence*, 100:333–343, 2002.

[104] Sławomir M. Kaczmarek, Amina Bensalah, and Georges Boulon. γ-Ray induced color centers in pure and Yb doped $LiYF_4$ and $LiLuF_4$ single crystals. *Optical Materials*, 28(1-2):123–128, jan 2006.

[105] S. P. Deshpande, S. J. Dhoble, W. K. Pokale, B. T. Deshmukh, R. B. Pode, and T. K. Gundurao. Radiation effect on the luminescence of $LiYF_4$: Er^{3+}. *Nuclear Instruments and Methods in Physics Research, Section B: Beam Interactions with Materials and Atoms*, 134(3-4):385–392, mar 1998.

[106] B Schaudel, P Goldner, M Prassas, and F Auzel. Ion irradiation damage in Er-doped silica probed by the Er^{3+} luminescence lifetime at 1.535 ţm. *Nucl. Instr. and Meth. in Phys. Res. B*, 354(3):16–48, 2008.

[107] Vera Pukhkaya, Philippe Goldner, Alban Ferrier, and Nadège Ollier. Impact of rare earth element clusters on the excited state lifetime evolution under irradiation in oxide glasses. *Optics Express*, 23(3):3270–3281, 2015.

[108] Lilia C. Courrol, Izilda M. Ranieri, Sônia L. Baldochi, Ricardo E. Samad, Anderson Z. de Freitas, Laércio Gomes, and Nilson D. Vieira. Study of color centers produced in thulium doped YLF crystals irradiated by electron beam and femtosecond laser pulses. *Optics Communications*, 270(2):340–346, 2007.

[109] Andris Fedotovs. *EPR of radiation defects in fluoride crystals and in oxyfluoride glass ceramics*. PhD thesis, PhD thesis]. Riga: University of Latvia Faculty of Physics And Mathematics, 2008.

[110] S. P. Feofilov, A. B. Kulinkin, V. A. Konyushkin, and A. N. Nakladov. Laser cooling of solids containing local centers with electric dipole allowed transitions: A feasibility study. *Optical Materials*, 48:75–79, 2015.

[111] Hiroki Sato, Amina Bensalah, Hiroshi Machida, Martin Nikl, and Tsuguo Fukuda. Growth and characterization of 3-in size Tm, Ho-codoped LiYF4 and LiLuF4 single crystals by the Czochralski method. *Journal of Crystal Growth*, 253(1-4):221–229, 2003.

[112] Vasilis Pagonis. *Luminescence Dosimetry: Signal Analysis Using Python*. Springer Nature, 2022.

[113] Ngangbam Chandrasekhar and RK Gartia. Gaussian approximation of thermoluminescence (tl) peaks: A common misconception for analysis of tl of persistent luminescent materials. *Journal of Alloys and Compounds*, 745:773–778, 2018.

[114] Anupum Panr, Katharina Senkalla, Xiaojing Xia, Chaman Gupta, Greg Felsted, Scott T. Dunham, Fedor Jelezko, and Peter J. Pauzauskie. Reduced photothermal heating in diamonds enriched with h3 pointd efects. *J. Appl. Phys.*, *in preparation*.

[115] B Tortech, Y Ouerdane, Sébastien Girard, J-P Meunier, A Boukenter, T Robin, B Cadier, and P Crochet. Radiation effects on yb-and er/yb-doped optical fibers: a micro-luminescence study. *Journal of Non-Crystalline Solids*, 355(18-21):1085–1088, 2009.

[116] A. Bensalah, M. Nikl, A. Vedda, K. Shimamura, T. Satonaga, H. Sato, T. Fukuda, and G. Boulon. X-ray induced color centres in pure and doped $LiYF_4$ and $LiLuF_4$ single crystals. *Radiation Effects and Defects in Solids*, 157(6-12):563–567, 2002.

[117] Jigang Yin, Yin Hang, Lianhan Zhang, Chengchun Zhao, Jing Xiong, and Pengchao Hu. Origin of the 330 nm absorption band and effect of doping Yb in $LiYF_4$ crystals. *Journal of Luminescence*, 130(8):1338–1342, 2010.

[118] Alexander S Ditter, Evan P Jahrman, Liam R Bradshaw, Xiaojing Xia, Peter J Pauzauskie, and Gerald T Seidler. A mail-in and user facility for x-ray absorption near-edge structure: The cei-xanes laboratory x-ray spectrometer at the university of washington. *Journal of Synchrotron Radiation*, 26(6):2086–2093, 2019.

[119] D. J. Richardson, J. Nilsson, and W. A. Clarkson. High power fiber lasers: current status and future perspectives [Invited]. *Journal of the Optical Society of America B*, 27(11):B63–B92, 2010.

[120] Xiangru Wang, Ying Chen, William Hageman, Gyu Ug Kim, Martin Richardson, Caidong Xiong, John Ballato, and Michael Bass. Transverse mode competition in gain-guided index antiguided fiber lasers. *J. Opt. Soc. Am. B*, 29(2):191–196, 2012.

[121] Shijie Fu, Wei Shi, Yan Feng, Lei Zhang, Zhongmin Yang, Shanhui Xu, Xiushan Zhu, R. A. Norwood, and N. Peyghambarian. Review of recent progress on single-frequency fiber lasers (invited). *J. Opt. Soc. Am. B*, 34(3):A49–A62, 2017.

[122] John H. Martin, Brennan D. Yahata, Jacob M. Hundley, Justin A. Mayer, Tobias A. Schaedler, and Tresa M. Pollock. 3D printing of high-strength aluminium alloys. *Nature*, 549(7672):365–369, SEP 21 2017.

[123] René Heller, Michael Hippke, and Pierre Kervella. Optimized trajectories to the nearest stars using lightweight high-velocity photon sails. *The Astronomical Journal*, 154(3):115–126, 2017.

[124] James D Kafka. Laser diode pumped fiber lasers with pump cavity, May 9 1989. US Patent 4,829,529.

[125] T.Y. Fan. Laser beam combining for high-power, high-radiance sources. *IEEE Journal of Selected Topics in Quantum Electronics*, 11(3):567–577, 2005.

[126] Kristian Rymann Hansen, Thomas Tanggaard Alkeskjold, Jes Broeng, and Jesper Lægsgaard. Thermo-optical effects in high-power Ytterbium-doped fiber amplifiers. *Optics Express*, 19(24):23965–23980, 2011.

[127] M. S. Kuznetsov, O. L. Antipov, A. A. Fotiadi, and P. Mégret. Electronic and thermal refractive index changes in ytterbium-doped fiber amplifiers. *Optics Express*, 21(19):22374–22388, 2013.

[128] Wei-Wei Ke, Xiao-Jun Wang, Xian-Feng Bao, and Xiao-Jian Shu. Thermally induced mode distortion and its limit to power scaling of fiber lasers. *Optics Express*, 21(12):14272–14281, 2013.

[129] Christophe A Codemard, Jayanta K Sahu, and Johan Nilsson. Tandem cladding-pumping for control of excess gain in ytterbium-doped fiber amplifiers. *IEEE Journal of Quantum Electronics*, 46(12):1860–1869, 2010.

[130] Pu Zhou, Hu Xiao, Jinyong Leng, Jiangmin Xu, Zilun Chen, Hanwei Zhang, and Zejin Liu. High-power fiber lasers based on tandem pumping. *J. Opt. Soc. Am. B*, 34(3):A29–A36, 2017.

[131] Xiushan Zhu and N. Peyghambarian. High-power ZBLAN glass fiber lasers: Review and prospect. *Advances in Optoelectronics*, 2010:1–23, 2010.

[132] Akira Sugiyama, Masamichi Katsurayama, Yutaka Anzai, and Taiju Tsuboi. Spectroscopic properties of yb doped ylf grown by a vertical bridgman method. *Journal of alloys and compounds*, 408:780–783, 2006.

[133] Venkataramanan Mahalingam, Fiorenzo Vetrone, Rafik Naccache, Adolfo Speghini, and John A. Capobianco. Structural and optical investigation of colloidal Ln^{3+}/Yb^3 co-doped KY_3F_{10} nanocrystals. *Journal of Materials Chemistry*, 19(20):3149, 2009.

[134] Angela Pirri, Daniele Alderighi, Guido Toci, Matteo Vannini, Martin Nikl, and Hiroki Sato. Direct comparison of Yb^{3+}:CaF_2 and heavily doped Yb^{3+}:YLF as laser media at room temperature. *Optics Express*, 17(20):18312, 2009.

[135] Guanying Chen, Tymish Y. Ohulchanskyy, Sha Liu, Wing-Cheung Law, Fang Wu, Mark T. Swihart, Hans Ågren, and Paras N. Prasad. Core/shell $NaGdF_4$:Nd^{3+}/$NaGdF_4$ nanocrystals with efficient near-infrared to near-infrared downconversion photoluminescence for bioimaging applications. *ACS Nano*, 6(4):2969–2977, 2012.

[136] XL Ruan and M Kaviany. Enhanced laser cooling of rare-earth-ion-doped nanocrystalline powders. *Phys. Rev. B*, 73(15):155422, 2006.

[137] Ziad Mohammed, Hossein Saghafifar, and Mahmood Soltanolkotabi. An approximate analytical model for temperature and power distribution in high-power Yb-doped double-clad fiber lasers. *Laser Physics*, 24(11):115107, 2014.

[138] D.C. Brown and H.J. Hoffman. Thermal, stress, and thermo-optic effects in high average power double-clad silica fiber lasers. *IEEE Journal of Quantum Electronics*, 37(2):207–217, 2001.

[139] Dong Xue. Three-dimensional simulation of the temperature field in high-power double-clad fiber laser. *Optik*, 122(10):932–935, 2011.

[140] E Snitzer, H Po, F Hakimi, R Tumminelli, and BC McCollum. Double-clad, offset core nd fiber laser. In *Optical fiber sensors*, page 5. Optical Society of America, 1988.

[141] Allan W Snyder and John Love. *Optical Waveguide Theory*. Springer Science & Business Media, 2012.

[142] Paden B Roder, Peter J Pauzauskie, and E James Davis. Nanowire heating by optical electromagnetic irradiation. *Langmuir*, 28(46):16177–16185, 2012.

[143] Hitoki Yoneda, Kazuhiko Yamaguchi, and Ken-ichi Ueda. Dispersion of optical refractive index of Yb^{3+}-doped laser glass and their fitting to Lorentzian model. *Jpn. J. Appl. Phys.*, 38(6A):L639–L641, 1999.

[144] Mikhail N. Polyanskiy. Refractive index database. `https://refractiveindex.info`. Accessed on 2019-05-02.

[145] M. C. Gupta and J. Ballato. *The Handbook of Photonics: Second Edition*. CRC Press, 2007.

[146] Theresa M Allen, Mark F Buehler, and E.James Davis. Radiometric effects on absorbing microspheres. *Journal of Colloid and Interface Science*, 142(2):343–356, 1991.

[147] Denis V. Seletskiy, Seth D. Melgaard, Stefano Bigotta, Alberto Di Lieto, Mauro Tonelli, and Mansoor Sheik-Bahae. Laser cooling of solids to cryogenic temperatures. *Nature Photonics*, 4(3):161–164, 2010.

[148] Anna Garahan, Laurent Pilon, Juan Yin, and Indu Saxena. Effective optical properties of absorbing nanoporous and nanocomposite thin films. *J. Appl. Phys.*, 101(1):014320, 2007.

[149] Johan Nilsson and David N Payne. High-Power Fiber Lasers. *Science*, 332(6032):921 LP – 922, may 2011.

[150] Richard I Epstein and Mansoor Sheik-Bahae. *Optical refrigeration science and applications of laser cooling of solids*. Wiley-VCH, 2009.

[151] Angel Fernandez-Bravo, Kaiyuan Yao, Edward S. Barnard, Nicholas J. Borys, Elizabeth S. Levy, Bining Tian, Cheryl A. Tajon, Luca Moretti, M. Virginia Altoe, Shaul Aloni, Kenes Beketayev, Francesco Scotognella, Bruce E. Cohen, Emory M. Chan, and P. James Schuck. Continuous-wave upconverting nanoparticle microlasers. *Nature Nanotechnology*, 13(7):572–577, 2018.

[152] Zikang Ye, Xing Lin, Na Wang, Jianhai Zhou, Meiyi Zhu, Haiyan Qin, and Xiaogang Peng. Phonon-assisted up-conversion photoluminescence of quantum dots. *Nature Communications 2021 12:1*, 12(1):1–9, jul 2021.

Appendix A

PUBLICATIONS

Journal Publications

1. **X. Xia**, X. Zhou, B. E. Smith, M. B. Lim, A. B. Bard, A. Pant, P. J. Pauzauskie, Interface-Dependent Radiative Lifetimes of Yb3+ , Er3+ Co-doped Single NaYF4 Upconversion Nanowires. *ACS Appl. Mater. Interfaces* **11(25)**, 2281722823 (2019).

2. **X. Xia**, A. Pant, E. J. Davis, P. J. Pauzauskie, Design of a radiation-balanced fiber laser via optically active composite cladding materials. *J. Opt. Soc. Am. B* **36(12)**, 3307 (2019).

3. **X. Xia**, A. Pant, A. S. Ganas, F. Jelezko, P. J. Pauzauskie, Quantum point defects for solid-state laser refrigeration. *Adv. Mat.* **33 (23)**, 1905406 (2021).

4. **X. Xia**, A. Pant, X. Zhou, E. A. Dobretsova, A. B. Bard, M. B. Lim, J-Y D. Roh, D. R. Gamelin, P. J. Pauzauskie, Hydrothermal synthesis and solid-state laser refrigeration of potassium lutetium fluoride microcrystals. *Chem. Mat.* **33 (12)**, 4417-4424 (2021).

5. **X. Xia**, A. Volpi, J-Y D. Roh, C. Michael, D. R. Gamelin, M. P. Hehlen, p. J. Pauzauskie, The impact of $^2H_{9/2} \longrightarrow {}^4I_{13/2}$ emission from Er^{3+} ions on ratiometric optical temperature sensing with Yb^{3+}/Er^{3+} co-doped upconversion materials. *J. Lumin.* **236**, 118006 (2021).

6. A. S. Ditter, E. P. Jahrman, L. R. Bradshaw, **X. Xia**, P. J. Pauzauskie, G. T. Seidler, A mail-in and user facility for X-ray absorption near-edge structure: the CEI-XANES laboratory X-ray spectrometer at the University of Washington. *J.*

Synchrotron Radiat. **26(6)**, 20862093 (2019).

7. A. Pant, **X. Xia**, E. J. Davis, P. J. Pauzauskie, Solid-state laser refrigeration of a composite semiconductor Yb: YLiF 4 optomechanical resonator. *Nat. Comm.* **11 (1)**, 1-7 (2020).

8. A. B. Bard, X. Zhou, **X. Xia**, *et al.*, A Mechanistic Understanding of Non-Classical Crystal Growth in Hydrothermal Sodium Yttrium Fluoride. *Chem. Mat.* **32 (7)**, 2753-2763 (2020).

9. E. A. Dobretsova, **X. Xia**, *et al.*, Solid-State Laser Refrigeration of Silicon-Nitride TEM Windows with Hydrothermally Synthesized Yb3+ :LuLiF 4. *Laser Photonics Rev.* 2100019 (2021).

10. A. S. Ganas, E. A. Dobretsova, B. Journaux, A. Pant, **X. Xia**, *et al.*, Solid-state laser refrigeration at GPa pressures. *Phys. Rev. Lett.* (in revision)

11. R. G. Felsted, A. Pant, A. B. Bard, **X. Xia**, *et al.*, Chemically tunable aspect ratio control and laser refrigeration of hexagonal sodium yttrium fluoride upconverting materials. *Chem. Mat*(submitted)

12. A. Pant, K. Senkalla, **X. Xia**, *et al.* Reduced photothermal heating in diamonds enriched with H3 point defects. *J. Appl. Phys* (submitted)

Conference Publications

1. 2017 MRS Fall Meeting-ORAL Presentation 2800963, Photoluminescence Lifetime of Single Upconversion Nanowire near an Interface.

2. 2019 SPIE Photonics West-ORAL Presentation 10936-17, Laser refrigeration of optical fibers via optically-active composite cladding materials.

3. 2020 SPIE Photonics West-ORAL Presentation 11298-13, Solid-state laser refrigeration of hydrothermal potassium lutetium fluoride microcrystals.

4. 2021 SPIE Photonics West-ORAL Presentation 11298-13, Computational design of a double-clad radiation balanced fiber laser.

Patents Radiation-balanced fiber laser, P. J. Pauzauskie, A. Pant, X. Xia, E. Dobretsova, E. J. Davis, A. B. Bard, ... US Patent App. 17/160,073

Solid-state laser refrigeration of composite optomechanical resonators Pauzauskie, A. Pant, X. Xia, E. Dobretsova, E. J. Davis, A. B. Bard, ... US Patent App. 17/152,572